

I hereby assign my copyright of this thesis to the Charles Stark Draper  
Laboratory, Inc., Cambridge Massachusetts.



Logan Milliken

Permission is hereby granted by the Charles Stark Draper Laboratory,  
Inc. to the Massachusetts Institute of Technology and to the U.S.  
Government and its agencies to reproduce and to distribute copies of  
this thesis document in whole or in part.

Accession For	
NTIS GRA&I	<input checked="" type="checkbox"/>
DTIC TAB	<input type="checkbox"/>
Unannounced	<input type="checkbox"/>
Justification <i>from 50 per</i>	
By _____	
Distribution/ _____	
Availability Codes	
Dist	Avail and/or
	Special
A-1	



MULTIVARIABLE CONTROL OF AN UNDERWATER VEHICLE

by

Logan George Milliken

Submitted to the Departments of Ocean Engineering and Mechanical Engineering in Partial Fulfillment of the Requirements for the Degrees of Ocean Engineer and Master of Science in Mechanical Engineering

ABSTRACT

Mathematical modeling of a submerged vehicle is accomplished using the Naval Ship Research and Development Center 2510 Report equations of motion with crossflow and vortex shedding terms added. A multivariable depth and heading controller is designed using the Linear Quadratic Gaussian/Loop Transfer Recovery design procedure wherein stability and robustness specifications are met in the frequency domain for a MIMO system. The resulting combination of the model-based compensator and plant is tested using a nonlinear simulation. With gain scheduling, multivariable control is extended over the vehicle's entire speed range.

Thesis Supervisor: Dr. Lena Valavani, Research Scientist  
Laboratory for Information and Decision Systems

#### ACKNOWLEDGEMENTS

I would like to thank, in particular, my thesis adviser, Lena Valavani, for her support in shaping the ideas of this thesis and her patience in seeing it through. Also, I sincerely thank William Bonnice of Draper Laboratory for his endless hours of assistance and advice on many of the practical aspects of this thesis. Finally, I wish to express my gratitude to my thesis supervisors, Professors D. Cummings and D. Yoerger, for their assistance and time.

The Charles Stark Draper Laboratory, Inc., has provided the facilities and financial resources required to complete this thesis. Publication of this thesis, however, does not constitute approval by the Charles Stark Draper Laboratory, Inc., of the findings or conclusions contained herein. It is published solely for the stimulation and exchange of ideas.

TABLE OF CONTENTS

<u>Chapter</u>	<u>Page</u>
ABSTRACT.....	3
ACKNOWLEDGEMENTS.....	4
LIST OF FIGURES.....	8
LIST OF TABLES.....	10
1. INTRODUCTION AND SUMMARY.....	11
1.1 Background.....	11
1.2 Contributions of the Thesis.....	12
1.3 Outline of the Thesis.....	13
2. SYSTEM DESCRIPTION, MODELING AND ANALYSIS.....	14
2.1 Introduction.....	14
2.2 System Description.....	14
2.3 Vehicle Modeling.....	16
2.3.1 Nonlinear Equations of Motion.....	16
2.3.2 Linear Time Invariant State Space Model.....	19
2.3.3 State Variables.....	20
2.3.4 Outputs and Control Inputs.....	20
2.3.5 Twenty Knot Linear Model.....	21
2.3.6 Model Verification.....	23
2.4 Model Dynamics.....	30
2.4.1 Analysis of the Twenty Knot Linear Model.....	30
2.4.2 Pole Structure.....	30
2.4.3 Modal Analysis.....	33
2.4.4 Multivariable Zeros.....	33
2.4.5 Controllability and Observability.....	33
2.4.6 Plant Open-Loop Singular Values.....	35
2.5 Chapter Summary.....	36
3. CONTROLLER SPECIFICATIONS AND ROBUSTNESS.....	38
3.1 Introduction.....	38
3.2 General Specifications.....	38
3.3 Specification Development.....	39
3.4 Robustness.....	43
3.5 Chapter Summary.....	48

Table of Contents (cont'd)

<u>Chapter</u>	<u>Page</u>
4. MODEL-BASED COMPENSATOR AND CONTROLLER DESIGN.....	49
4.1 Introduction.....	49
4.2 Model-Based Compensator Structure.....	49
4.3 Calculation of Gain Matrices.....	53
4.4 Control Surface Dynamics and Augmentation.....	54
4.4.1 Actuator Dynamics and Augmentation.....	54
4.4.2 Overall System Model.....	57
4.4.3 Augmented Plant Dynamics.....	61
4.5 Compensator Design Methodology.....	61
4.6 Compensator Design Example.....	66
4.7 Compensated System Response.....	75
4.7.1 Simulation.....	75
4.7.2 Initial Conditions and Reference Inputs.....	75
4.7.3 Error Limits.....	76
4.7.4 Compensated Linear and Nonlinear Responses to Step Inputs.....	76
4.7.5 Compensated Linear and Nonlinear Ramp Responses...	80
4.8 Chapter Summary.....	82
5. GAIN SCHEDULING.....	84
5.1 Introduction.....	84
5.2 Twenty Knot Controller.....	84
5.2.1 Range of the Twenty Knot Controller.....	84
5.2.2 Vehicle Response at Fifteen Knots with Twenty Knot Gains.....	84
5.2.3 Vehicle Response at Thirty Knots with Twenty Knot Gains.....	89
5.3 Ten Knot Linear Model.....	93
5.4 Five Knot Linear Model.....	96
5.5 Gain Scheduling Algorithm.....	100
5.5.1 Selected Gain Scheduling Results.....	101
5.6 Chapter Summary.....	110

<u>Table of Contents (cont'd)</u>	<u>Page</u>
6. SUMMARY, CONCLUSIONS AND RECOMMENDATIONS.....	111
6.1 Summary.....	111
6.2 Conclusions.....	112
6.3 Recommendations for Further Study.....	112
APPENDIX A: Nonlinear Equations of Motions and Kinematic Relations.....	114
APPENDIX B: Linearized Equations of Motion.....	121
APPENDIX C: Summary of SUBMODEL Program.....	136
TABLE C.1: Twenty Knot Accelerations and Equilibrium States.....	140
TABLE C.2: Twenty Knot Linear System: <u>A</u> , <u>B</u> and <u>C</u> Matrices.....	141
TABLE C.3: Twenty Knot Augmented Linear System: <u>A</u> , <u>B</u> and <u>C</u> Matrices.....	142
TABLE C.4: Twenty Knot Compensator Gains: <u>G</u> and <u>H</u> Matrices Matrices.....	143
APPENDIX D: Ten Knot Model.....	144
TABLE D.1: Ten Knot Augmented Linear System: <u>A</u> , <u>B</u> and <u>C</u> Matrices.....	144
TABLE D.2: Ten Knot System Eigenvalues and Transmission Zeros .....	145
TABLE D.3: Ten Knot Compensator Gains: <u>G</u> and <u>H</u> Matrices.....	146
APPENDIX E: Five Knot Model.....	147
TABLE E.1: Five Knot Augmented Linear System: <u>A</u> , <u>B</u> and <u>C</u> Matrices.....	147
TABLE E.2: Five Knot System Eigenvalues and Transmission Zeros.....	148
TABLE E.3: Five Knot Compensator Gains: <u>G</u> and <u>H</u> Matrices Matrices.....	149
REFERENCES.....	150

## LIST OF FIGURES

### CHAPTER 2

<b>FIGURE 2.1</b>	Submerged Vehicle Showing Axes, Forces and Moments Moments.....	15
2.2	Linear and Nonlinear Responses at Twenty Knots, $q=r=.01$ .....	24
2.3	Linear and Nonlinear Responses at Twenty Knots with a Sternplane Deflection of 2 Degrees.....	28
2.4	Linear and Nonlinear Responses at Twenty Knots with a Rudder Deflection of 2 degrees.....	29
2.5	Modal Analysis of Twenty Knot Linear Model.....	34
2.6	Singular Values of the Twenty Knot Open-Loop Plant.....	37

### CHAPTER 3

<b>FIGURE 3.1</b>	Plot of Singular Values Versus Frequency.....	40
3.2	General Feedback System.....	44
3.3	Robustness in Terms of Multiplicative Error.....	44

### CHAPTER 4

<b>FIGURE 4.1</b>	MIMO Feedback System.....	51
4.2	State Space Description of the MBC.....	51
4.3	First Order Lag Compensation Block Diagram.....	56
4.4	State Space Representation of the Augmented Dynamics.....	56
4.5	Overall Compensated System.....	59
4.6	Nominal Plant with Augmentation.....	59
4.7	Singular Values of Twenty Knot Augmented Plant.....	62
4.8	Singular Values of $\underline{G}_{FOL}(s)$ .....	68
4.9	Singular Values of $\underline{G}_{KF}(s)$ .....	70
4.10	Singular Values of the Compensated Open-Loop System.....	71
4.11	Singular Values of $[\underline{I} + \underline{T}(jw)]$ .....	73
4.12	Singular Values of $[\underline{I} + \underline{T}^{-1}(jw)]$ .....	74
4.13	Step Response of the Twenty Knot Compensated Nonlinear Model.....	77

	<u>List of Figures (cont'd)</u>	<u>Page</u>
4.14	Thirty Degree Ramp Response of the Compensated Nonlinear Model.....	81
4.15	Fifty Foot Ramp Response of the Compensated Nonlinear Model.....	83
 <b>CHAPTER 5</b>		
<b>FIGURE 5.1</b>	Compensated Nonlinear Step Response at 15 Knots with 20 Knot Gains.....	85
5.2	Compensated Nonlinear Response to a 30 Degree Ramp at 15 Knots with 20 Knot Gains.....	87
5.3	Compensated Nonlinear Response to a 50 Foot Ramp at 15 Knots with 20 Knot Gains.....	88
5.4	Compensated Nonlinear Step Response at 30 Knots with 20 Knot Gains.....	90
5.5	Compensated Nonlinear Response to a 30 Degree Ramp at 30 Knots with 20 Knot Gains.....	91
5.6	Compensated Nonlinear Response to a 50 Foot Ramp at 30 Knots with 20 Knot Gains.....	92
5.7	Singular Values of the Ten Knot Open-Loop Plant.....	94
5.8	Singular Values of the Compensated Ten Knot System.....	95
5.9	Singular Values of the Five Knot Open-Loop Plant.....	97
5.10	Singular Values of the Compensated Five Knot System.....	99
5.11	Scheduled Nonlinear Step Response at Seven Knots.....	102
5.12	Scheduled Nonlinear 30 Degree Ramp Response at Seven Knots.....	103
5.13	Scheduled Nonlinear 50 Foot Ramp Response at Seven Knots.....	105
5.14	Scheduled Nonlinear Step Response at Fifteen Knots.....	106
5.15	Scheduled Nonlinear 30 Degree Ramp Response at Fifteen Knots.....	108
5.16	Scheduled Nonlinear 50 Foot Ramp Response at Fifteen Knots.....	109

## LIST OF TABLES

### CHAPTER 2

### Page

TABLE 2.1	Model Inputs, States and Outputs.....	22
2.2	Eigenvalues of the Twenty Knot System.....	32
2.3	Transmission Zeros of the Twenty Knot System.....	32

### CHAPTER 3

TABLE 3.1	Encounter Frequencies.....	41
3.2	Settling Times and Crossover Frequencies.....	42
3.3	Depth Excursion Limits.....	42

### CHAPTER 4:

TABLE 4.1	Second Order Actuator Dynamics.....	55
-----------	-------------------------------------	----

## 1.0 INTRODUCTION AND SUMMARY

### 1.1 Background

The purpose of this thesis is to investigate the applicability of designing a multivariable controller for a deeply submerged underwater vehicle using the Linear Quadratic Gaussian (LQG) with Loop Transfer Recovery (LTR) methodology. At the present time, there are few examples of multi-input, multi-output (MIMO) design of complex systems using the LQG procedure and still fewer examples which actually test the control system on a nonlinear simulation as will be accomplished in this thesis.

While it is possible that full state feedback could be achieved in the present system, this is not always practical or feasible in general for systems with inaccessible state variables. Moreover, being able to accomplish control with only a selected set of the available state variables provides additional flexibility and efficiency in designing a fault-tolerant system.

As one of the primary concerns of submerged vehicle operations is course and depth keeping, it is natural to desire to control the heading angle ( $\psi$ ,  $\psi$ ) and depth ( $z$ ) of the vehicle. Thus, for this design it is intended to feedback only two states ( $\psi$  and  $z$ ) and obtain reconstruction of the remainder as a by-product of a Kalman filter-based estimator within the compensator structure.

There are several reasons for designing a depth and heading controller. An automatic control system can be expected to reduce the operational workload and thus the required manning. With manual control, the response to course and depth changes tends to be oscillatory, especially at higher speeds. Automatic control should provide control surface movement which is more precise, requiring less overall motion and energy. The reduction in lifting surface motion will also lower vehicle resistance and reduce fuel costs.

It is emphasized that the type of controller design proposed here would be utilized under normal operating conditions such as transits from one location to another or in patrolling a given area of the ocean. It is not intended that the control system be used for rapid maneuvers such as collision avoidance or navigation in restricted waters.

### 1.2 Contributions of the Thesis

The primary contribution of this thesis is the design of a truly multivariable control system for a submerged, underwater vehicle. Typically, such vehicles have been controlled by separating plans of motion and coordinating the decoupled control actions. However, when cross-coupling is considerable, the control system thus designed may actually become unstable.

Design of a truly multivariable controller overcomes the shortcomings of some of the "classical" designs. The coupling between planes of motion, as discussed in Chapter 2, is particularly severe for the system under consideration. With multivariable control, these coupling effects are incorporated in the design and thus, one may expect to develop good controllers in a more systematic fashion.

An additional contribution of this thesis is that it represents the first attempt to apply the LQG/LTR control methodology to design an autopilot for a submersible. This methodology, which largely follows the work of Doyle and Stein [5], has several excellent characteristics. First, it is a systematic procedure which, through the use of singular values, allows one to "design to" a set of frequency-domain specifications. With appropriately chosen design specifications, the compensated system will exhibit desirable command following and disturbance rejection properties as well as insensitivity to modeling errors and sensor noise. Further, the design methodology allows one to ascertain the multivariable robustness properties (stability margins), ensuring closed-loop stability in the presence of modeling errors.

Finally, the control design is tested on a nonlinear simulation. Due to the inherent robustness properties of the LQG method, we may expect the controller to operate satisfactorily at other than its nominal speed and position in state space. This will ease the gain scheduling task.

### 1.3 Outline of the Thesis

Chapter 2 contains a physical description of the submarine with its nonlinear and linearized equations of motion. The second part of the chapter investigates the dynamics of the linear model obtained at twenty knots. This includes a modal analysis and the open loop singular values of the plane.

Chapter 3 discusses the desirable characteristics of the controller and sets some specifications to be met in the frequency and time domains. Multivariable robustness considerations are also discussed.

Chapter 4 presents the model-based compensator structure along with a discussion of the augmented dynamics incorporated in this design. The LQG/LTR controller design methodology is shown and a control design based on the twenty knot linear model is developed. Finally, the compensator is tested on the linear and nonlinear simulations.

Chapter 5 investigates the speed range over which the compensator, designed using the twenty knot linear model, meets the specifications and presents the other models (linearized for different speeds) necessary to accomplish automatic control over the speed range of the submarine.

Finally, Chapter 6 contains the conclusions and recommendations for future study.

## 2.0 SYSTEM DESCRIPTION, MODELING AND ANALYSIS

### 2.1 Introduction

In this chapter we shall first discuss the submarine in physical terms, describing its salient features and dynamic characteristics. Some background will be given in the sequel describing the nonlinear equations of motion after which a short derivation of the linearized dynamics is presented along with the state variables and system inputs and outputs. The twenty-knot linear model is then presented and verified by comparing the linear and nonlinear dynamic responses. Finally, an analysis of the dynamics of the linear model is undertaken including the pole/zero structure and a modal analysis.

### 2.2 System Description

The system to be controlled is a manned, underwater vehicle with port/starboard (left/right) symmetry as shown in Figure 2.1. For the purpose of this control design the vehicle is assumed to be well below the surface of the ocean and its mass constant. Neutral buoyancy is assumed as the ballast system is not modeled. The control surface configuration consists of a cruciform stern with separate sternplanes and rudder located aft and fairwater planes located on the sail. There is no differential control; that is, both the upper and lower or port and starboard control surfaces must rotate together.

Positive rudder deflections primarily cause the vehicle to turn left; however, due to vehicle banking (which causes the rudder to act to some degree as a sternplane) as well as crossflow drag effects and lifting surface memory effects the vehicle exhibits a tendency to dive in a turn. Further, the stern and fairwater plans will tend to be "seen", to a certain extent, as rudders. These effects are quite pronounced at higher speeds. Thus, there is considerable cross-coupling between planes of motion.

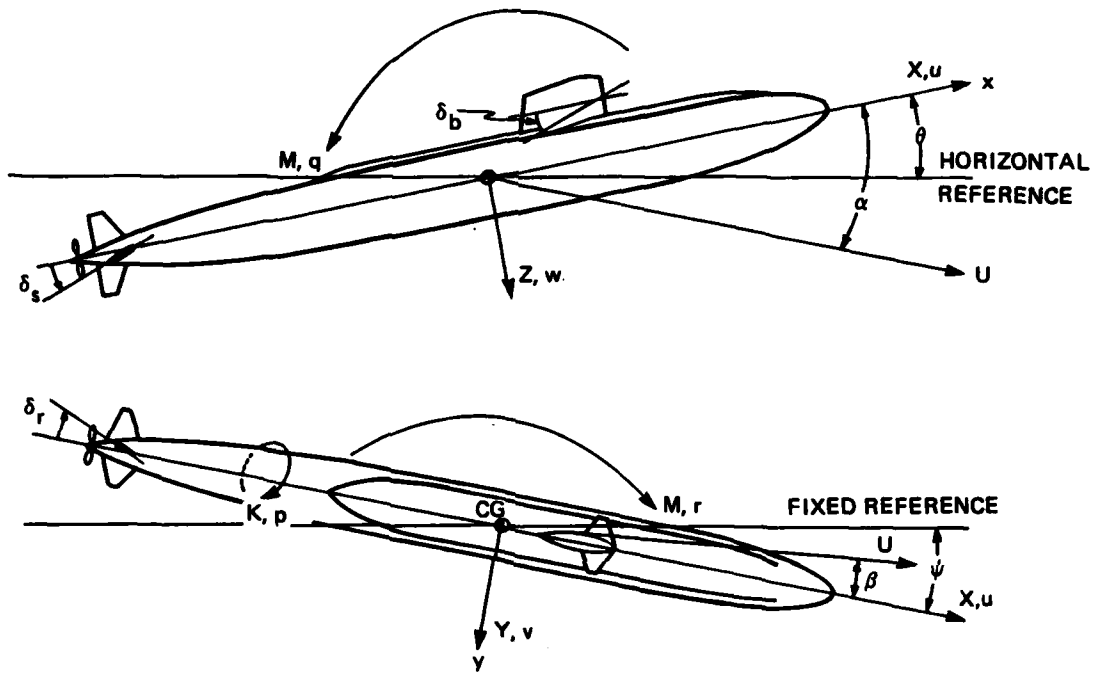


Figure 2.1. Sketch showing positive directions of axes, angles, velocities, forces, and moments.

While the generic model of the underwater vehicle is based on the original Naval Ship Research and Development Center (NSRDC) 2510 Report [8], various supplemental models have subsequently evolved. These modifications enable the model to predict well at least one particular aspect of vehicle motion. The most notable additions attempt to model the memory effects of velocities induced on the afterbody and control surfaces by trailing vortices from the fairwater planes and sail. Thus, the effects of crossflow drag and vortex shedding have been included in the math model; however, neither surface or bottom effects are included.

Finally, the subject vehicle is capable of speeds in excess of thirty knots with a minimum speed of about five knots. The sternplanes and rudder are limited to a maximum of plus or minus forty degrees of rotation with the fairwater planes' maximum excursion limited to twenty degrees.

### **2.3 Vehicle Modeling**

#### **2.3.1 Nonlinear Equations of Motion**

The system dynamics, including control forces and moments exerted by the rudder and planes, are typically described by a set of six degree of freedom nonlinear differential equations based on the NSRDC 2510 report [8]. The equations are general enough to simulate the rigid body trajectories and responses of a submarine in normal maneuvers as well as in extreme maneuvers such as those associated with emergency recoveries from a sternplane jam and flooding casualties. Over the years correlation to full scale trial measurements with the following equations has shown them to yield accurate predictions of submarine motions and trajectories. The advantage of using this formulation is that it is experimentally based and takes advantage of commonly used experimental techniques in generating many of the hydrodynamic coefficients.

The hydrodynamic coefficients constitute the heart of the mathematical model used to simulate the rigid-body motions of the vehicle. The hydrodynamic coefficients used for this study are for a deeply submerged vehicle, free of free-surface, bottom, and wall effects. The hydrodynamic forces and moments which enter into the equations as coefficients are usually classified into three categories: static, rotational, and acceleration. The static coefficients are from the linear velocity components of the vehicle relative to the fluid, the rotary coefficients are due to angular velocity components and the acceleration coefficients are due to either linear or angular accelerations. Within limited ranges, the coefficients are linear with respect to the appropriate variables, and thus yield good results in the linearized equations of motion [8].

The major modeling problem therefore reduces to finding the numerical values of the individual coefficients with sufficient accuracy to support the objective of the simulation study, in this case an automatic heading and depth controller to be used during normal underway operations. Ideally, one would acquire the values for a given vehicle configuration using hydrodynamic theory. Unfortunately, those coefficients which are due primarily to viscous flow considerations, such as the static and rotary coefficients, cannot be obtained reliably using existing theory alone. Theory has been used with good results in computing the acceleration coefficients for simple shapes without appendages, using potential flow theory. For an actual underwater vehicle which includes appendages such as control surfaces, propellers and bridge fairwaters, the use of theory does not, in most cases, yield results which accurately describe the physical system. Accordingly, the present state of the art is either to rely on experimental means or semi-empirical computer-based methods to determine the hydrodynamic coefficients for a specific design.

The primary experimental method used to obtain the coefficients is the planar-motions-mechanisms-system in conjunction with a physical model of the vehicle. The physical models used for testing are large as

towing tank. This permits determination of the hydrodynamic coefficients which are comparatively free of scale effects and other experimental problems. Using a large model allows one to obtain, more easily, the high Reynolds number necessary to avoid the effects of transitional flow over the hull and appendages of the model. The planar-motions-mechanism is used to find all the values of hydrodynamic coefficients except certain coupling terms and those nonlinearities associated with high values of angular velocity, found while conducting tight turns or dives [1,8]. If such values are required, the planar-motions-mechanism tests are supplemented by the rotating-arm test. The hydrodynamic coefficients used in this study were provided by NSRDC for a generic underwater vehicle.

The equations of motion are written in a right-hand orthogonal system of moving axes, fixed in the body, with its origin located at the center of gravity of the vehicle. The axes are body fixed as the hydrodynamic forces and inertia are most readily computed in the vehicle's frame. As shown in Figure 2.1, the xy plane is the principal plane of symmetry, with the x-axis parallel to the baseline of the body. The positive direction of the axes are as follows: x-forward, y-starboard, and z-downward. The remaining sign conventions follow from the right-hand rule. The positive directions of the axes, angles, linear and angular velocity components, forces and moments are also shown in Figure 2.1. For the purposes of control, it is sufficient to include the effect of relative motion between the body frame and flat non-rotating earth frame with the latter used as the inertial frame. Thus the effects of the earth's rotation and its spherical shape have been neglected as they are relatively small. The nonlinear equations, and kinematic relations, are given in Appendix A, and include the crossflow drag and lifting surface memory effects. The definitions of the hydrodynamic coefficients are contained in reference [8].

### 2.3.2 Linear Time Invariant State Space Model

For the purposes of controller design the nonlinear equations of motion are linearized about an operating or nominal point. Further, it is sought to place the linearized equations in a state space form as shown below:

$$\underline{M}\dot{\underline{x}} = \underline{A}\underline{x} + \underline{B}\underline{u} \quad (2.1)$$

where  $\underline{x}$  is the state variable vector and  $\underline{u}$  is the control vector.

The equations are therefore expanded in a Taylor Series about the steady-state operating point with only the first order terms of the expansion being retained. Thus, given the nonlinear state model of the form:

$$\underline{M}\dot{\underline{x}} = \underline{f}(\underline{x}, \underline{u}) \quad (2.2)$$

we linearize about the nominal point  $\underline{x}_0, \underline{u}_0$ . Neglecting higher order terms we find the linearized dynamics to be described by the following equations

$$\underline{M}\dot{\underline{x}}_0 + \underline{M}\Delta\dot{\underline{x}} = \underline{f}(\underline{x}_0, \underline{u}_0) + \frac{\delta f(\underline{x}_0, \underline{u}_0)}{\delta \underline{x}}(\underline{x}-\underline{x}_0) + \frac{\delta f(\underline{x}_0, \underline{u}_0)}{\delta \underline{u}}(\underline{u}-\underline{u}_0). \quad (2.3)$$

The nominal input  $\underline{u}_0$  and the resulting nominal state  $\underline{x}_0$  satisfy the original equations of motion at the nominal point,  $\underline{M}\dot{\underline{x}}=\underline{f}(\underline{x}_0, \underline{u}_0)$ . Defining  $\Delta\underline{x} = (\underline{x} - \underline{x}_0)$  and  $\Delta\underline{u} = (\underline{u} - \underline{u}_0)$ , one has

$$\underline{M}\Delta\dot{\underline{x}} = \frac{\delta f(\underline{x}_0, \underline{u}_0)}{\delta \underline{x}} \Delta\underline{x} + \frac{\delta f(\underline{x}_0, \underline{u}_0)}{\delta \underline{u}} \Delta\underline{u} \quad (2.4)$$

which is of the desired form, where  $\underline{A} = \frac{\delta f(\underline{x}_0, \underline{u}_0)}{\delta \underline{x}}$  and  $\underline{B} = \frac{\delta f(\underline{x}_0, \underline{u}_0)}{\delta \underline{u}}$ .

The linearized equations of motion can be found in Appendix B.

### 2.3.3 State Variables

The six equations for surge, sway, heave, roll, pitch and yaw contain eight variables in addition to the hydrodynamic coefficients. These are  $u$  (forward speed),  $v$ ,  $w$ ,  $p$ ,  $q$ ,  $r$ ,  $\phi$  and  $\theta$ . To the previous six equations we add the four kinematic relations - depth rate ( $\dot{z}$ ), roll rate ( $\dot{\phi}$ ), pitch rate ( $\dot{\theta}$ ), and yaw rate ( $\dot{\psi}$ ). As it is intended to control the yaw/heading angle and depth these variables will be considered as the feedback state variables for this design. It is interesting to note that none of the ten state equations used to model the system is a function of the heading angle or depth. Thus, the system as presently modeled has two integrators associated with the variables  $\psi$  and  $z$ . Within linear system theory, this integrator action shall ensure no steady state error for step disturbances in the closed-loop compensated system.

### 2.3.4 Outputs and Control Inputs

The intent of this thesis is to use and evaluate the loop transfer recovery technique (discussed in Chapter 4) to design the compensator. This methodology requires a square system with an equal number of control inputs,  $u$ , and observed outputs,  $y$ . As the compensator to be designed is to control the heading angle and depth; and, since these variables are readily available for measurement, they are selected as the system outputs. Thus, the output vector is:

$$\underline{y} = \begin{bmatrix} \psi \\ z \end{bmatrix} \quad (2.5)$$

The choice of two control inputs is only slightly more difficult. The vehicle has available, as inputs, its three control surfaces - the rudder, stern and fairwater planes. As the fairwater and sternplanes

are redundant (either can separately control depth, depth rate or pitch) and present operating procedure is to fix the fairwater planes while utilizing the sternplanes; the system inputs selected were the rudder and sternplane deflection ( $\delta_r$ ,  $\delta_s$ ). The input vector is then:

$$\underline{u} = \begin{bmatrix} \delta_r \\ \delta_s \end{bmatrix}. \quad (2.6)$$

Note that by not utilizing the fairwater planes under normal conditions, a separate set of gains can, in the future, be generated as a means of back-up depth control. Table 2.1 lists the inputs, states and outputs of the submarine used in this control design along with their respective units.

### 2.3.5 Twenty Knot Linear Model

The function of the multivariable controller to be designed is to maintain an ordered course and depth as well as to be capable of altering vehicle heading and depth. As the submarine will spend the great majority of time maintaining a given course and depth, it was decided to linearize about straight ahead motion at constant speed. The SUBMODEL program, developed at Draper Laboratory is briefly discussed in Appendix C and, more completely, in reference [18]. It was used to find the local equilibrium point.

The local equilibrium point was found by perturbing  $u$ ,  $v$ ,  $w$ ,  $p$ ,  $q$ ,  $r$ ,  $\phi$ , and  $\theta$  until the accelerations (derivations of the states) were, practically speaking, zero. The accelerations and equilibrium values of the states at twenty knots are listed in Table C.1 of Appendix C.

At this point, the linear dynamics are calculated and the ten by ten  $M^{-1}A$  ( $A_p$ ) and the ten by three  $M^{-1}B$  ( $B_p$ ) matrices generated. The  $A_p$ ,  $B_p$ , and  $C_p$  matrices are shown in Table C.3 of Appendix C and represent the unaugmented submarine model at twenty knots. The  $B_p$  matrix still shows three controls as the fairwater planes have not yet been "locked". Subsequently, in the control design, the second column of  $B_p$  (corresponding to the fairwater planes), is deleted.

TABLE 2.1

Vehicle Control Inputs

$u_1$  = sternplane deflection - degrees  
 $u_2$  = rudder deflection - degrees

States

$x_1$  =  $u$ , forward speed - ft/sec  
 $x_2$  =  $v$ , lateral speed - ft/sec  
 $x_3$  =  $w$ , vertical speed - ft/sec  
 $x_4$  =  $p$ , roll rate - radians/sec  
 $x_5$  =  $q$ , pitch rate - radians/sec  
 $x_6$  =  $r$ , yaw rate - radians/sec  
 $x_7$  =  $\phi$ , roll angle - degrees  
 $x_8$  =  $\theta$ , pitch angle - degrees  
 $x_9$  =  $\psi$ , yaw/heading angle - degrees  
 $x_{10}$  =  $z$ , depth - feet

System Outputs

$y_1$  =  $\psi$ , yaw angle - degrees  
 $y_2$  =  $z$ , depth - feet

### 2.3.6 Model Verification

To ascertain the validity of the linear model about a particular nominal point, one only has to equally perturb the linear and nonlinear models (using the SUBMODEL program), then observe and compare their responses. If the linear model dynamics are sufficiently close to the nonlinear response, one may have confidence in the linear model. Additionally, one can gain a feeling for the region of state space in which the linear model is valid by comparing the linear and nonlinear responses for various perturbations from the nominal point.

As an example, the linear and nonlinear responses with no control surface deflection and initial perturbations in  $q$  and  $r$  of 0.01 radians/second are shown in the plots in Figure 2.2. Note with the exception of the forward speed,  $u$ , the close agreement of responses. The difference in forward speed can be attributed to the fact that we linearized about straight ahead motion at constant speed [1]. Other tests with different states perturbed were made with the comparisons between linear and nonlinear responses being, in general, excellent. Since the controller is to be capable of turning and diving, non-zero settings of the rudder and sternplanes were also compared.

Comparing the linear and nonlinear responses with the sternplanes set at two degrees, there is generally good agreement, especially if one compares not only the shapes but the absolute values. Of particular interest are the  $\psi$  and depth responses shown in Figure 2.3. The nonlinear and linear values at 100 seconds for  $\psi$  although opposite in direction are both essentially zero (.0045 versus -.0013 degrees). The depth response for the linear model follows very closely for the first thirty seconds (within one foot). The depth at 100 seconds being 633 feet for the linear model and 574 feet in the nonlinear case. The variations between the responses is certainly acceptable.

When one compares the linear and nonlinear heading and depth responses with a two-degree rudder deflection (Figure 2.4) the major weakness of linearizing about straight ahead motion becomes apparent. The linear model shows nearly no deviation in depth during a turn (-.16

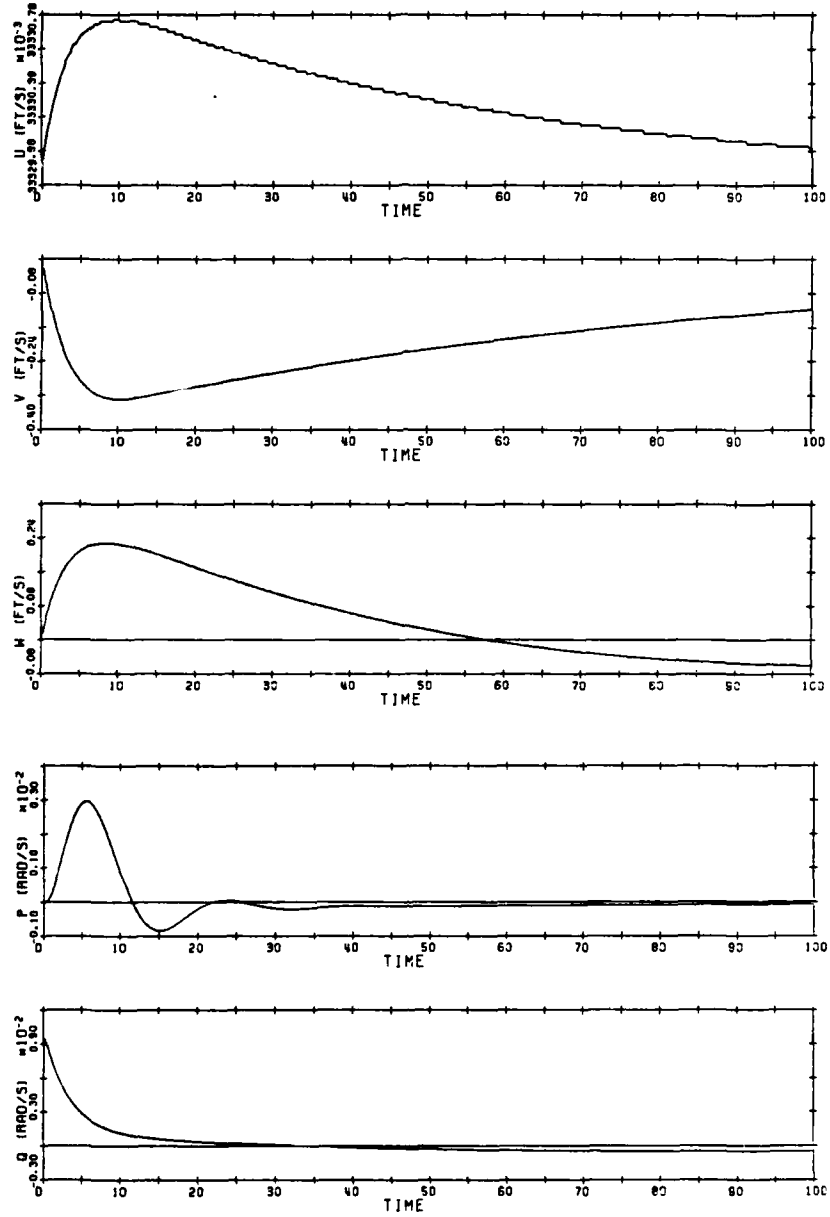


**Figure 2.2: Linear Model Response at Twenty Knots,  $q=r=.01$  radians per second**

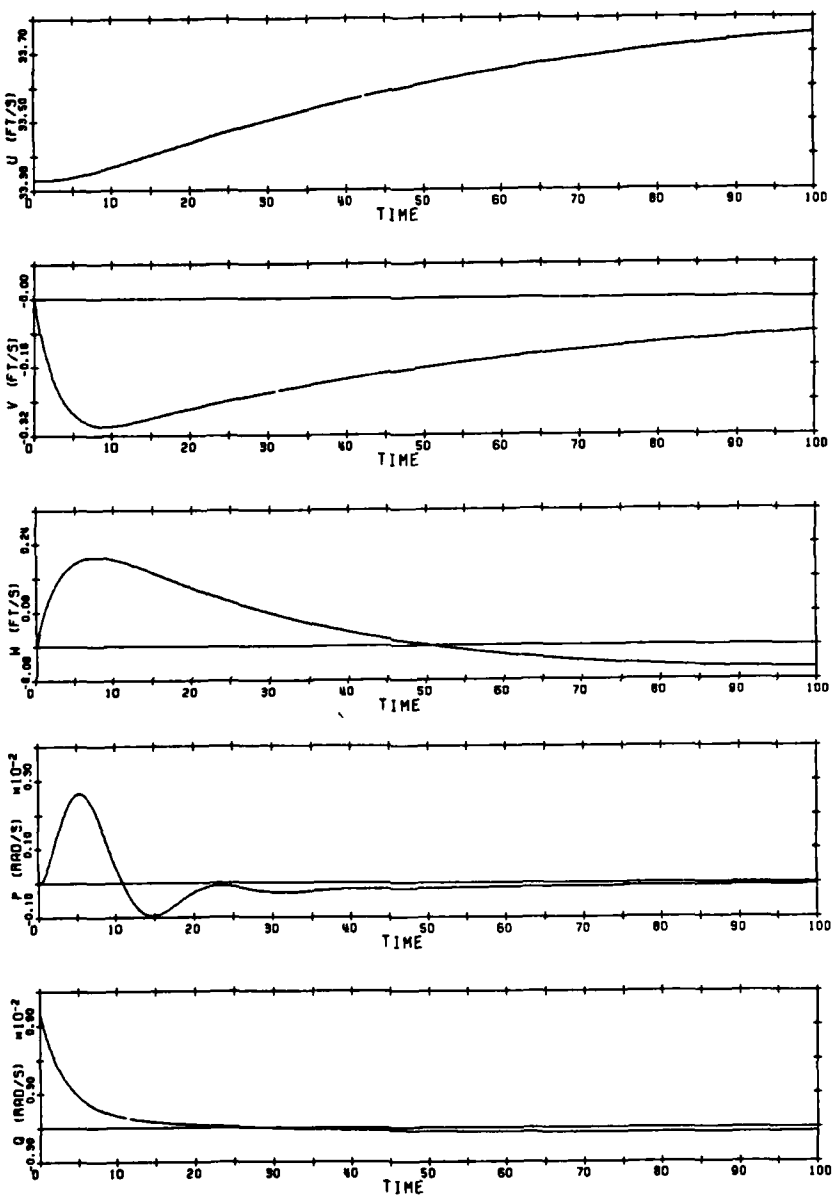


**Figure 2.2: Nonlinear Model Response at Twenty Knots,  $q=r=.01$  radians per second**

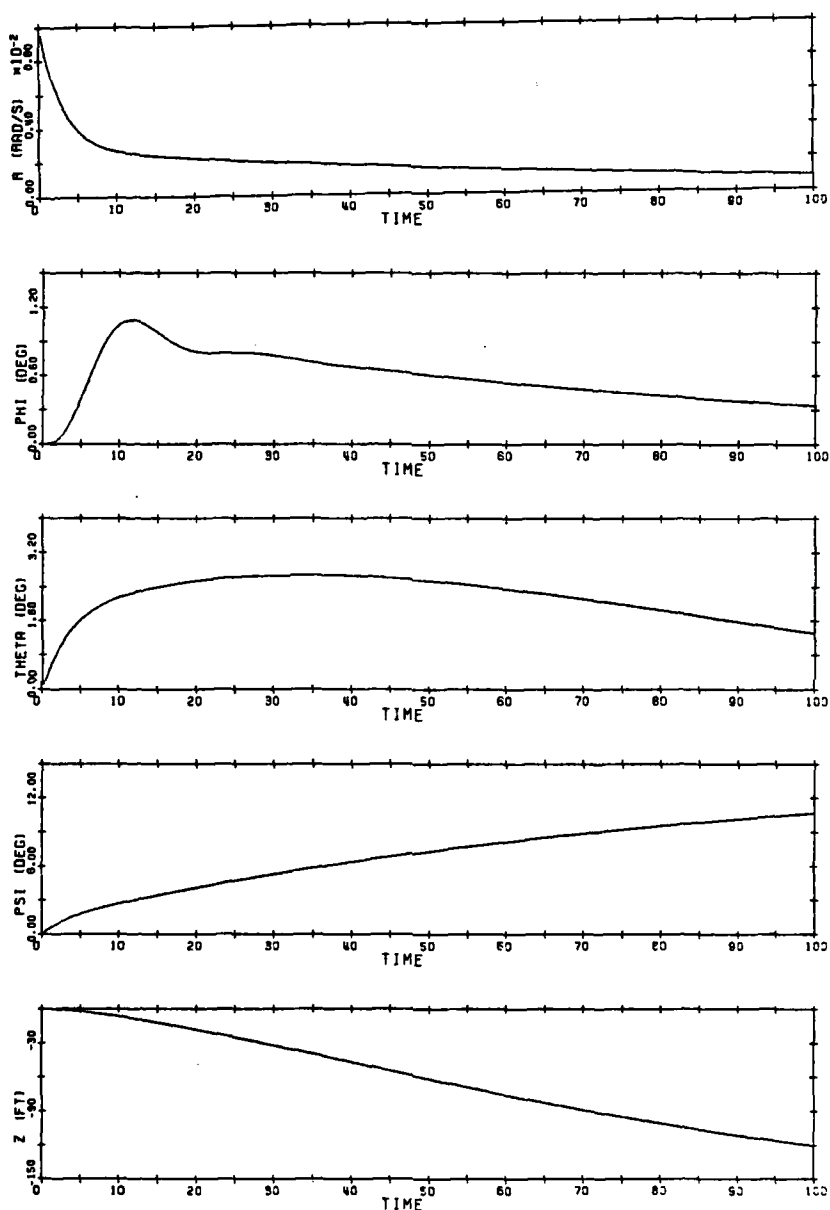


**Figure 2.2:** Linear Model Response at Twenty Knots,  $q=r=.01$  radians per second

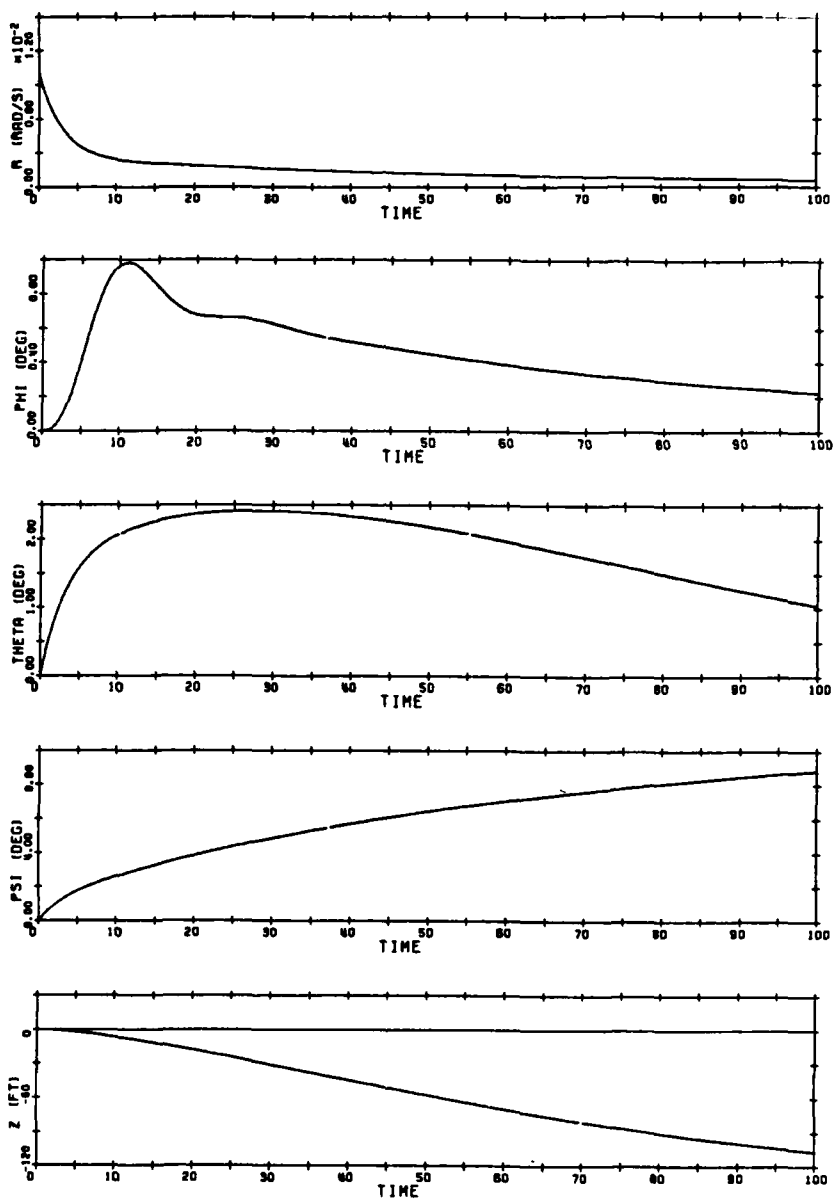
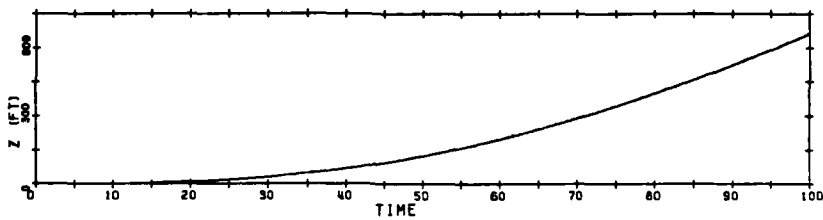
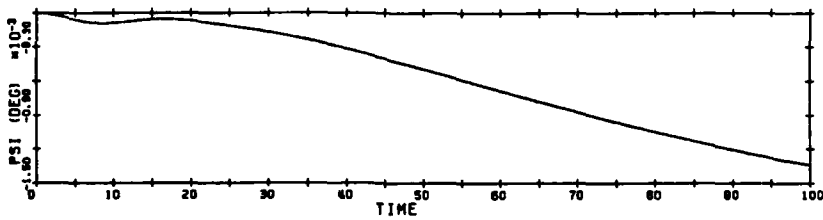
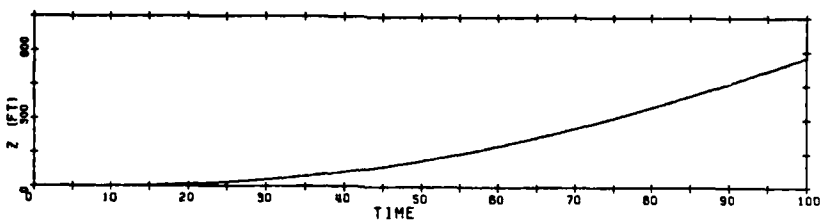
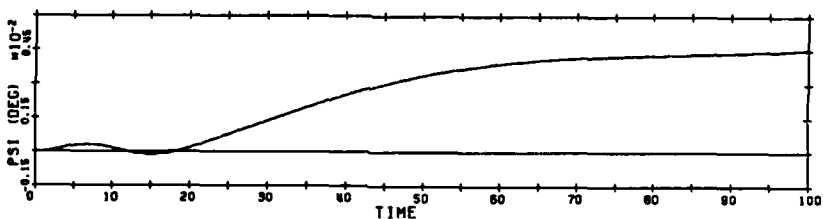


**Figure 2.2:** Nonlinear Model Response at Twenty Knots,  $q=r=.01$  radians per second

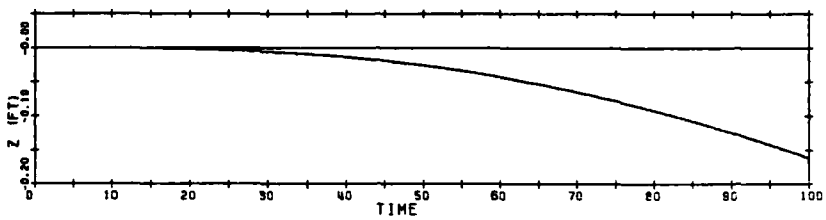
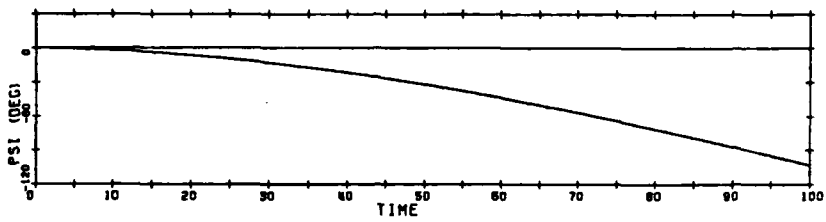


LINEAR

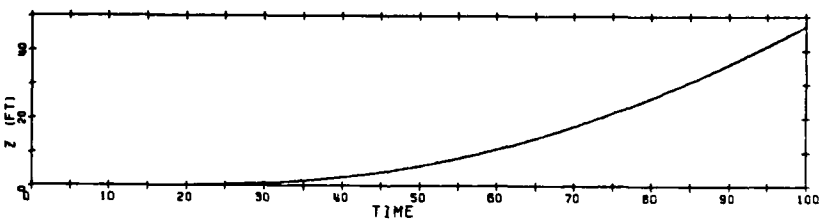
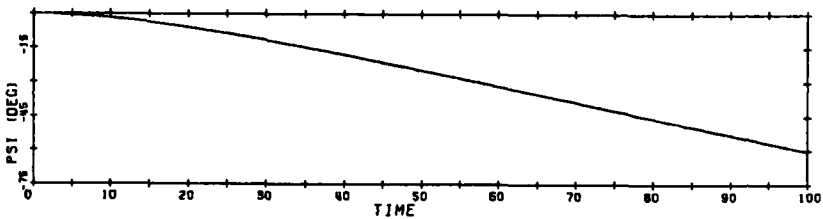


NONLINEAR

**Figure 2.3: Linear and Nonlinear Responses at Twenty Knots with a Sternplane Deflection of 2 Degrees**



LINEAR



NONLINEAR

Figure 2.4: Linear and Nonlinear Responses at Twenty Knots with a Rudder Deflection of 2 Degrees

feet) while the nonlinear model (due to the cross-coupling effects) shows a depth excursion of 47 feet at 100 seconds. However, it should be noted that the difference between the two models is less than a foot at times less than 30 seconds.

The psi responses compare well, with the difference between the linear and nonlinear heading being less than 1.5 degrees at 30 seconds. At 100 seconds, the nonlinear model has shown a heading change of -60 degrees while the linear model is at -103 degrees.

Other comparisons with different control surface deflections and vehicle speeds show the same general results. As expected, the linear and nonlinear model responses increasingly deviate as the deflections and speeds increased, however there was good agreement in the first 20 to 30 seconds. These analyses suggest that, if the control design which is based on the linear model of the submarine, requires large, prolonged control surface deflections, the compensator may not provide adequate response to perturbations. This is so because the controller will have based its actions on the expected linear response while the actual vehicle more closely follows the nonlinear model.

## 2.4 Model Dynamics

### 2.4.1 Analysis of the Twenty Knot Linear Model

In this section, the submarine dynamics shall be investigated. The multivariable poles and zeros are presented and their implications discussed. A modal analysis is conducted to further validate the linear model and lead to a more complete understanding of the vehicle dynamics. Controllability and observability studies are undertaken and the plant open-loop singular values are calculated and their implications in future controller design discussed.

### 2.4.2 Pole Structure

The stability of the system depends solely on its poles (the eigenvalues of  $A_p$ ). For stability all eigenvalues must have negative real parts. Stability implies that, if the vehicle is perturbed from

its equilibrium point in state space, it will naturally tend to return to its nominal state. The poles of the system are shown in Table 2.2.

Note the two poles at zero due to the independence of all the equations to the state variables  $\psi$  and  $z$ . These poles at the origin show that there is no tendency for the vehicle to return to a given heading or depth (assuming that weight equals buoyancy) when perturbed. Further note that the fastest system pole is -0.33 radians per second. This emphasizes the fact that the submarine is a very slow system. Also, the two sets of complex conjugate pairs correspond to the oscillatory roll and pitch modes. It is desirable to further associate the poles with the states and modes in order that one may gain insight into the physical system and also further verify the linear model. To accomplish this, a modal analysis of the linear system was performed.

#### 2.4.3 Modal Analysis

As the heading angle and depth of the vehicle have no effect on the six modes (surge, sway, heave, roll, pitch and yaw) a reduced  $\underline{A}$  matrix with the  $\psi$  and  $z$  states and equations deleted was used in computing the eigenvalues. This leaves the remaining eight eigenvectors (two of which form conjugate pairs) to describe the six degrees of submarine motion.

The normalization of the eigenvectors highlights the issues of appropriate dimensions. The state variables  $u$ ,  $v$ , and  $w$  are in units of feet per second,  $p$ ,  $q$ , and  $r$  in radians per second and  $\phi$  and  $\theta$  in radians. There is no consistent set of factors by which to non-dimensionalize the  $\underline{A}_p$  matrix (and hence the eigenvectors). Ideally, each column of  $\underline{A}_p$  could be normalized by its respective state equilibrium value; however, in this instance, most of the equilibrium states are essentially zero (see Table C.1).

In order to more appropriately view the eigenvectors, the three linear velocities of each eigenvector were normalized by the largest among  $u$ ,  $v$  and  $w$ . The three angular velocities and two angles ( $\phi$  and  $\theta$ )

TABLE 2.2  
Twenty Knot Linear System Eigenvalues

0.000000  
0.000000  
-.011766  
-.014427 ± 0.016029  
-.025288  
-.141521 ± 0.365928  
-.296676  
-.329816

TABLE 2.3  
Twenty Knot System Transmission Zeros

-.025288  
-.13902 ± 0.36063  
-.16079  
-.17617  
+.48846

were likewise normalized among themselves. Thus, while we are not able to compare the contribution to each mode from each state on a uniform basis, we may still gain an adequate feel for the individual state contribution to each mode by the previously described normalization method.

Figure 2.5 plots for each eigenvalue, the dominant components of its normalized eigenvector. The plots give an indication of the directions (in state space) in which each eigenvalue is important. Also, by analyzing which states are dominant in a particular mode (eigenvector), one can associate with each mode a particular state. This information is also indicated on the plots of Figure 2.5.

#### 2.4.4 Multivariable Zeros

Table 2.3 lists the transmission zeros of the system. There is a non-minimum phase (NMP) zero at +0.488. At present it is not clear precisely how NMP zeros can be handled so that they do not adversely affect control system performance. It is known that, if a right-half plane zero is within the bandwidth of the system, it will impose severe limitations on system performance [5,15]. However, if the NMP zero is above crossover (outside the bandwidth) it is expected that its adverse effect will be greatly attenuated.

#### 2.4.5 Controllability and Observability

It is instructive to ascertain whether or not the linear model is controllable and observable. This is due to the fact that, if  $[A_p, B_p]$  is a controllable pair (hence, stabilizable) and  $[A_p, C_p]$  is an observable pair (implying detectable), then one is guaranteed that at least one set of control and filter gain matrices exist such that the closed-loop compensated system is stable.

A system is controllable, if the input  $\underline{u}$  can control the complete state  $\underline{x}$  of the system. This implies every mode is affected by at least one input. As the system, described by the linear time invariant matrices  $A_p$ ,  $B_p$  and  $C_p$  has repeated eigenvectors and  $A_p$  is

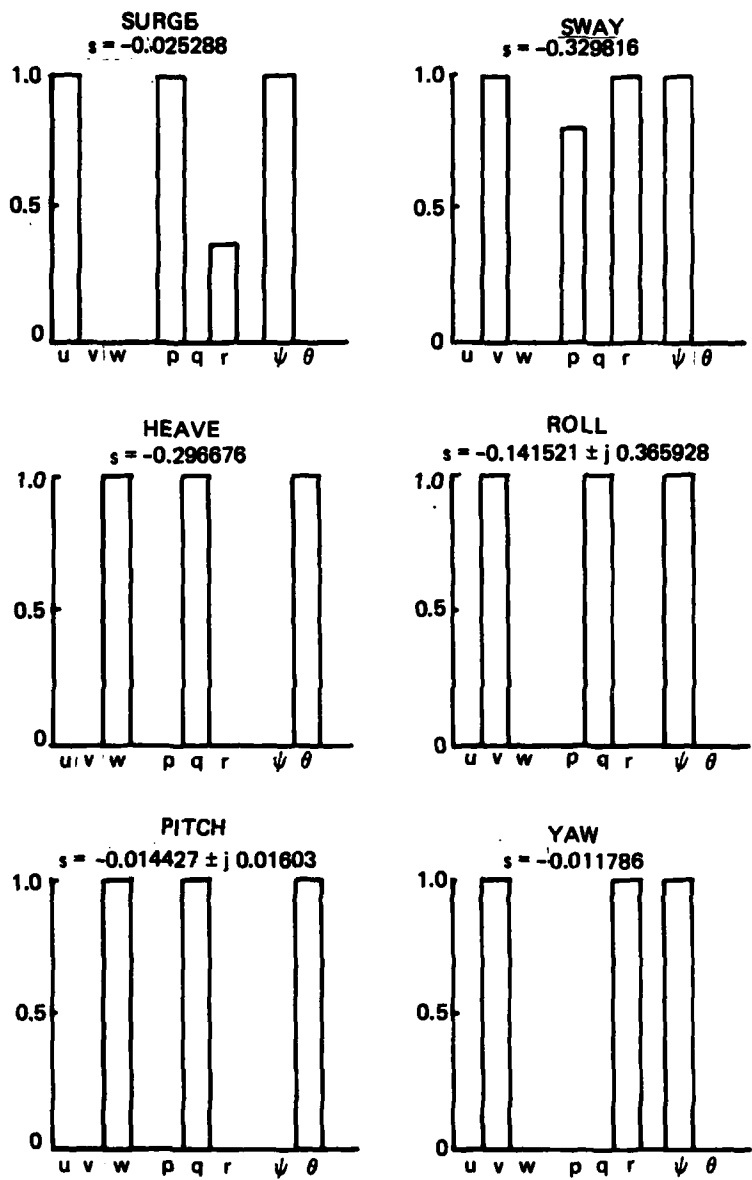


Figure 2.5. Modal analysis of the twenty knot linear model.

singular, the method used to ascertain system controllability is

$$\text{Rank}[\underline{B_p}, \underline{A_p}, \underline{B_p}, \dots, \underline{A_p^{n-1}} \underline{B_p}] = p. \quad (2.7)$$

If the rank  $p$ , is equal to the order of the system,  $n$  (ten in this case), the system is controllable.

A system is observable, if the complete state of the system can be ascertained from observing the output  $\underline{y}$ . This implies every mode is connected to at least one output. The test for observability used here was

$$\text{Rank}[\underline{C_p}, \underline{A_p} \underline{C_p}, \dots, (\underline{A_p})^{-1} \underline{C_p}] = q. \quad (2.8)$$

If the rank of the above matrix is equal to the system order,  $n$ , the system is observable. By forming the above matrixies and determining their ranks, the system was found to be both observable and controllable.

#### 2.4.6 Open Loop-Plant Singular Values

In the multivariable case, the best extension of the Bode plot concept of single input, single output (SISO) systems is a plot of the transfer matrix singular values. Briefly, singular values of a matrix  $\underline{M}$ ,  $\sigma(\underline{M})$ , are a function of frequency and are defined as:

$$\sigma_i(\underline{M}) = \sqrt{\sigma_i(\underline{M^*M})} \quad (2.9)$$

where:  $\sigma_i$  =  $i$ th singular value

$\lambda_i$  =  $i$ th eigenvalue of  $\underline{M}$

$\underline{M^*}$  = the complex conjugate transpose of  $\underline{M}$

For our purpose, we substitute the plant transfer function matrix,  $\underline{G}(s)$  for  $\underline{M}$  [3], where

$$\underline{G}(s) = \underline{C_p}(\underline{sI} - \underline{A_p})^{-1} \underline{B_p} \quad (2.10)$$

and, using a computer routine, the singular values of  $\underline{G}(s)$  as a function of frequency are calculated and plotted. Figure 2.6 is the plot of singular values of the open-loop transfer function  $\underline{G}(s)$  for the twenty knot linear model.

The maximum singular value is dominated by the depth, the minimum by the heading angle. Notice that the crossover frequency of the maximum singular value is approximately 1.0 radian per second while the minimum singular value crossover occurs at about 0.13 radians per second. This implies that the submarine naturally responds more quickly in depth; and also, that designing a controller which is too fast (crossover greater than 0.13 in the psi channel) will attempt to drive the vehicle faster than it could naturally respond. Finally, it is noted that the maximum singular value corresponding to depth crosses over beyond the NMP zero. In designing the controller it will be advantageous for the singular values to cross over at a lower frequency, first, because the crossover frequency should be well below unmodeled and other undesirable dynamics so as to attenuate their effects and, second, so that the NMP zero will be outside the closed-loop system's bandwidth.

## 2.5 Chapter Summary

The physical system to be controlled along with some of its particular dynamic characteristics were discussed. The nonlinear equations of motion, based on the NSRDC 2510 report and their linearized counterparts for straight ahead motion at twenty knots, were presented.

The linear model at twenty knots was successfully verified by comparing the linear and nonlinear model responses to similar perturbations. It was found that for periods of less than thirty seconds, the responses were nearly identical. Finally, the dynamics of the twenty knot linear model were investigated. In the next chapter, time and frequency domain specifications will be developed.

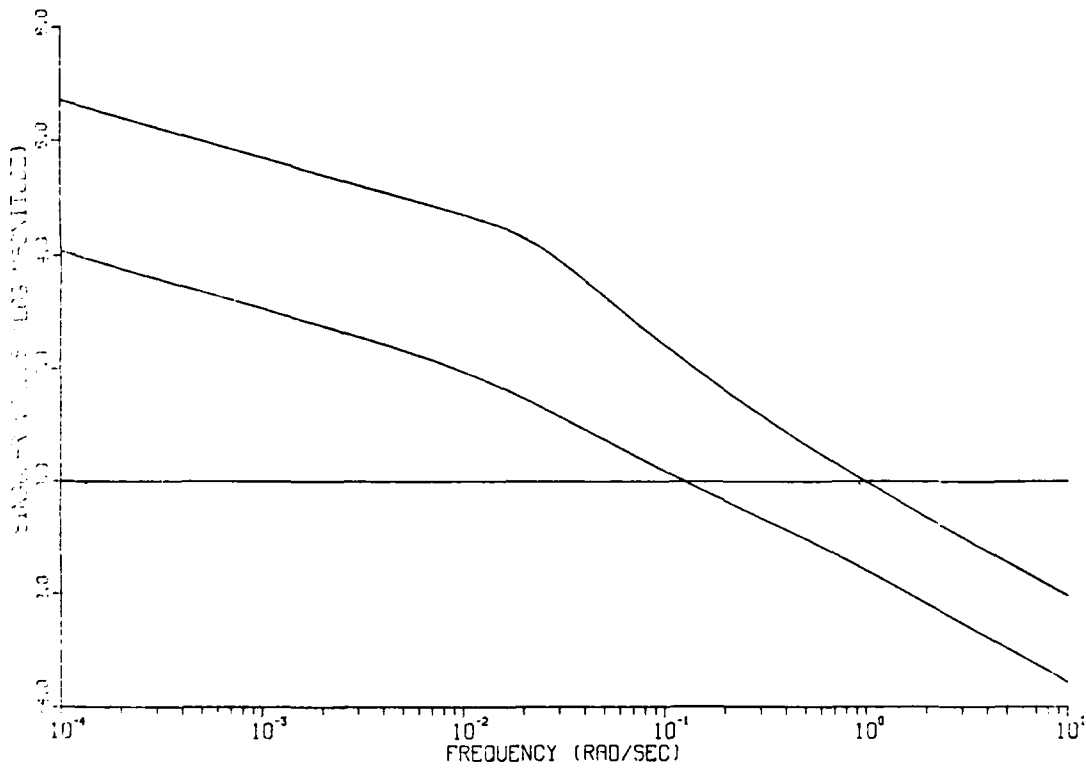


**Figure 2.6: Singular Values of the Twenty Knot Open-Loop Plant**

### 3. CONTROLLER SPECIFICATIONS AND ROBUSTNESS

#### 3.1 Introduction

In this chapter some desirable attributes of an automatic heading and depth controller will first be qualitatively discussed. Next, a set of frequency domain specifications will be derived which will serve as a basis for the compensator design of Chapter 4. Time domain specifications will also be presented against which the resultant compensator shall be tested. Finally, the concept of robust multivariable control is discussed and the definition of multivariable phase and gain margins given.

#### 3.2 General Specifications

There are no clearly stated design specifications which this particular compensator is required to meet. The time domain figures used herein are the designers goals based on several discussions with operational personnel. In general terms, it is desired that a multivariable controller be designed for use as an "autopilot" to maintain course and depth in the presence of disturbances such as shifting currents. It is envisioned that the compensator be activated when the submarine is near its ordered course and depth. This implies that the compensator be able to response favorably to step inputs (in psi and z) as it is unlikely that the submarine will be precisely at the ordered heading or depth when the automatic control system is activated. Further it is required that the controller be able to alter the course and depth of the submarine in response to either step or ramp inputs in heading and depth with small steady state errors. Another requirement is that the control system allow the vehicle to accomplish a level turn, that is, undergoing very little depth excursion while making a turn. Finally, as the multivariable controller is not to be designed for rapid/critical maneuvers, the speed of response is not of primary importance.

The MIMO extension of a bode plot is a plot of the singular values of the transfer matrix. Referring to Figure 3.1, in the frequency domain, it is required that the stable, closed-loop compensator have good command following, input and output disturbance rejection, and low sensitivity to modeling errors and sensor noise. Thus, one desires the minimum singular value to have high DC and low frequency gains for good command following and disturbance rejection while at higher frequencies, where unmodeled dynamics and sensor noise typically have their energy, the maximum singular value should be small and roll off rapidly.

In the time domain, the control design should minimize any oscillatory response or overshoot. This takes priority over the speed of response for the present design objectives. Generally, an overdamped response is considered desirable. Small steady state errors are required.

### 3.3 Specification Development

First we shall set some guidelines in the frequency domain. Having no other criteria, the surface wave frequency spectrum was used to deduce some maximum crossover frequency limits. As discussed in reference [17], the surface wave spectrum has a frequency range typically between 0.2 and 2 radians per second. The frequency of encounter,  $\omega_e$ , between the sea spectrum and a moving vehicle is a function of the sea spectrum frequency, the angle between the vehicle and direction of propagation of the dominant wave front and vehicle speed. Specifically, from reference [13], within linear theory:

$$\omega_e = \omega^2 - \frac{\omega^2 u}{g} \cos\psi \quad (3.1)$$

where:  $u$  = ship speed in ft/sec

$g$  = gravity

$\omega$  = wave spectrum frequency

$\psi$  = direction of the vehicle relative to the direction  
of wave propagation (180 for head seas)

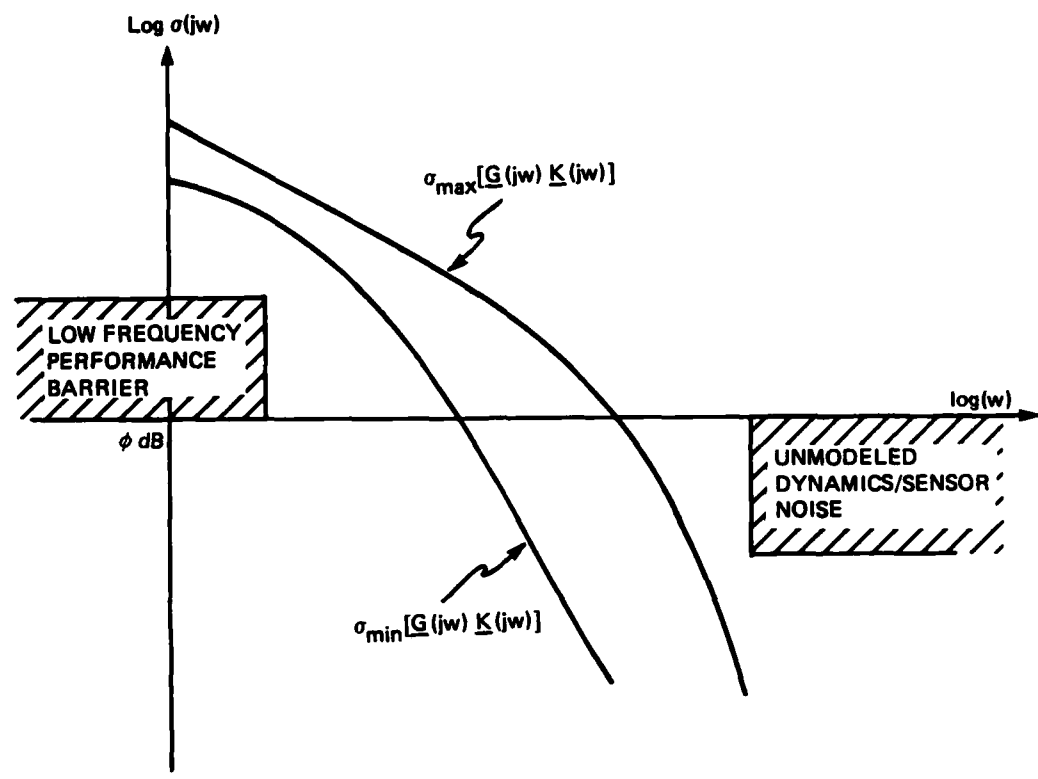


Figure 3.1. Plot of singular values versus frequency.

The worst case (lowest crossover) is for following seas ( $\psi=0$ ) in the presence of low frequency waves ( $\omega = 0.2$ ). Thus, for various speeds, the encounter frequencies presented in Table 3.1 gives some indication of frequencies above which the controller should attenuate energy.

TABLE 3.1: Encounter Frequencies

Speed (Knots)	Encounter Frequency
30	.137
20	.158
10	.179
5	.189

Sensor noise is well above this range; and, therefore, it will be readily attenuated by a compensator designed according to the above considerations for crossover. Note also that the NMP zero at +.488 is well above the indicated crossover frequency.

In setting a lower frequency "limit", one may use the settling time allowable. Here, the settling time is the time required to reach and stay within 10 percent of the reference value. From experience, reasonable settling times for a significant course (10 degrees) and depth (30 feet) changes as a function of speed are shown in Table 3.2. If one assumes that the steady state is reached in approximately four time constants, we are left with an indication of the lower frequency limit for crossover.

TABLE 3.2: Settling Times and Crossover Frequencies

Speed (Knots)	Settle Time (sec)	Frequency
30	100	.040
20	200	.020
10	300	.013
5	400	.010

A tight crossover pattern is indicated by the above analysis. As the minimum singular value (corresponding to  $\psi_1$ ) was found to have a crossover of about 0.13 radians per second along with the considerations above, the twenty knot controller shall be designed with crossovers of between .02 and 0.13 radians per second. Since the DC gain appears to increase with larger bandwidths for this system, it is advantageous to design at or near a crossover frequency of 0.13 radians per second. It is emphasized that these ranges are guidelines rather than strict limits. Further, it should be noted that the design procedure to be discussed in Chapter 4 would apply equally as well to a different set of specifications.

In the time domain, the specifications to be met include the settling times (Table 3.2) for simultaneous 10 degree and 30 foot step perturbations. Additionally, any overshoot or oscillatory response is to be minimized but, from experience, acceptable figures are 20 feet in depth and 5 degrees in heading.

The allowable deviation in depth during a course change is a function of vehicle speed. The currently acceptable figures are:

TABLE 3.3: Depth Excursion Limits

Speed	Allowable Depth Excursion
<10 kts.	10 feet
10-20 kts.	15 feet
>20 kts.	20 feet

Heading deviations during a depth change are to be limited to three degrees.

Of considerable importance is the allowable steady state error. An acceptable absolute value for heading error is less than one degree while depth error should be less than five feet. A more useful specification for steady state error is a percentage of the required change or deviation. Obviously, we should expect larger errors for greater course and depth changes. It is the objective of the design to maintain a three percent or less steady state error using the nonlinear simulation.

Finally there is the issue of rate limitations on the control surfaces. The state of the art for the size of the control surfaces and vehicle speeds in this design is 12 to 15 degrees per second. This limitation was not explicitly included in the compensator design or programmed in the simulation but must be kept in mind when deciding if a particular controller is acceptable.

### 3.4 Robustness

The issue of robustness deals with the fact that any model is at best an approximation. Usually the model is a relatively low order linear time invariant approximation in which modeling errors predominantly manifest themselves at higher frequencies. These high frequency modeling errors include neglected dynamics (for instance from the assumption of rigid body motion), time delays and neglected nonlinearities. The basic concern is to find the extent to which the nominal design values of the plant model can deviate without causing system instability.

For purposes of this discussion, the feedback system is as shown in Figure 3.2, with the loop transfer matrix,  $\underline{G}(s)$ , incorporating both the plant dynamics and any compensation utilized.

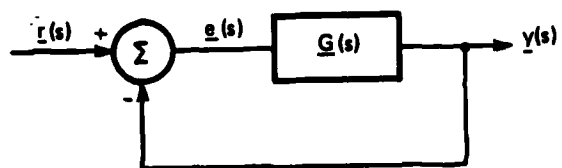


Figure 3.2. General feedback system.

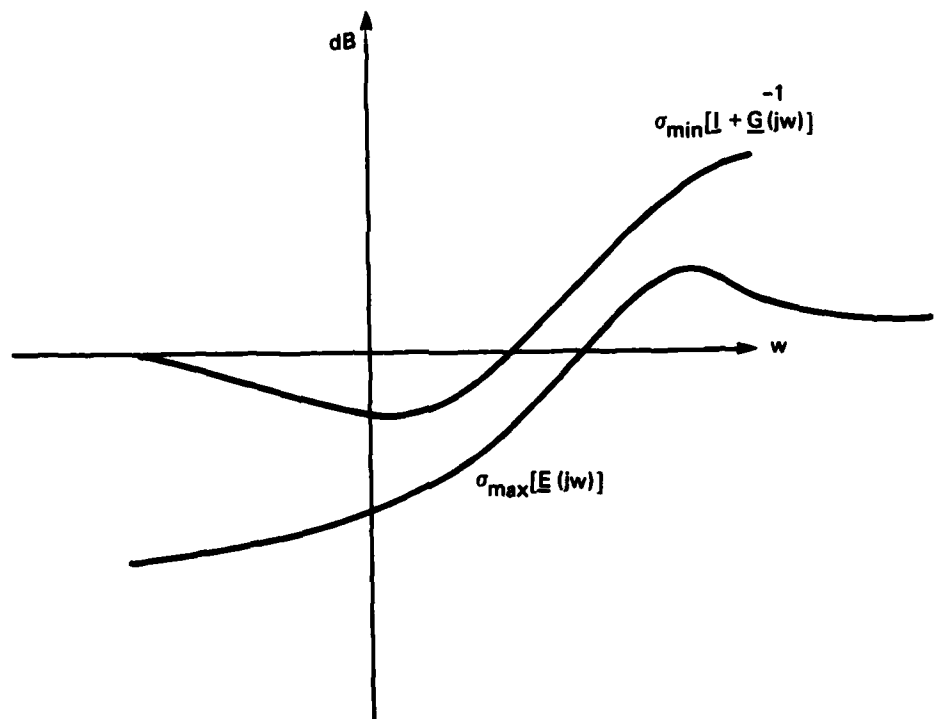


Figure 3.3. Robustness in terms of multiplicative error.

For the single input single output (SISO) case, the Nyquist stability criterion not only informs one if the closed-loop system is stable but also allows one to graphically visualize the stability margins (robustness) of the system by viewing the locus of  $g(s)$  (scalar  $\underline{G}(s)$ ) in relation to the critical point [12]. For the MIMO case, the multivariable Nyquist criterion [5,11,12] answers the question of asymptotic nominal closed-loop stability, but does not indicate the sort or size of errors which will drive the system unstable. In order to obtain a measure of robustness (i.e., stability margins) in the MIMO system one must use singular values.

As stated above, the actual plant,  $\hat{G}(s)$ , differs from the nominal plant,  $\underline{G}(s)$ , because of modeling approximations and errors. There are many ways in which to model these errors. The most common ways are as additive or multiplicative errors. For additive errors we have

$$\hat{G}(s) = \underline{G}(s) + \underline{E}(s) \quad (3.2)$$

where  $\underline{E}(s)$  is the error matrix. For multiplicative errors we find

$$\hat{G}(s) = \underline{G}(s) [\underline{I} + \underline{E}(s)] \quad (3.3)$$

It can be shown [11] that for additive (or division) errors the system will be on the verge of instability when

$$\det[\underline{I} + \hat{G}(s)] = 0. \quad (3.4)$$

Similarly, for multiplicative (or subtractive) errors the verge of instability in the MIMO case is [11,12].

$$\det[\underline{I} + \hat{G}^{-1}(s)] = 0.$$

In terms of the MIMO Nyquist criterion, this is where the number of nominal encirclements of the critical point changes.

In terms of singular values we are interested in the smallest  $\underline{E}(s)$  such that the return difference transfer matrix ( $[\underline{I} + \hat{G}(s)]$  or  $[\underline{I} + \hat{G}^{-1}(s)]$ ) is singular. It has been shown [11,12] that, if the following conditions hold:

1. The actual ( $\hat{\phi}_{OL}(s)$ ) and nominal ( $\phi_{OL}(s)$ ) open-loop characteristic polynomials have the same number of right half plane (RHP) roots (unstable poles).
2. If  $\hat{\phi}_{OL}(j\omega_0) = 0$  then  $\phi_{OL}(j\omega_0) = 0$
3.  $\phi_{CL}(s)$  has no RHP zeros (no unstable poles)

then the actual closed-loop polynomial ( $\hat{\phi}_{CL}(s)$ ) will have no RFP roots if

- a. For the additive or division error models

$$\sigma_{\min}[(\underline{I} + \underline{G}(j\omega))] > \sigma_{\max}[\underline{E}(j\omega)] \quad (3.6)$$

- b. For the multiplicative or subtractive error models

$$\sigma_{\min}[\underline{I} + \underline{G}^{-1}(j\omega)] > \sigma_{\max}[\underline{E}(j\omega)]. \quad (3.7)$$

The requirement for robust control for multiplicative error can be visualized as shown in Figure 3.3. Thus, one may ensure the robustness of the system under consideration using the above inequalities, if an error matrix can be adequately estimated. However, if, as in our case, there is no good estimate of the error margin, other means must be used to check for robustness.

We shall examine the MIMO gain and phase margins as developed in reference [12]. If the three previously stated conditions hold and

$$\sigma_{\min}[\underline{I} + \underline{G}(s)] > \alpha \quad (3.8)$$

or

$$\sigma_{\min}[\underline{I} + \underline{G}^{-1}(s)] > \beta \quad (3.9)$$

then the guaranteed phase (PM) and gain (GM) margins are given respectively by:

$$GM = \frac{1}{1+\alpha} \quad (3.10)$$

$$PM = \pm \cos^{-1}[1 - \frac{\alpha^2}{2}] \quad (3.11)$$

or

$$GM = [1 \pm \beta] \quad (3.12)$$

$$PM = \pm \cos^{-1}[1 - \frac{\beta^2}{2}] \quad (3.13)$$

It should be noted that the phase and gain margins are somewhat conservative in the sense that the gains or phases of all the feedback loops may be changed simultaneously without destabilizing the closed-loop system. In fact, individual loops may have larger margins, taken one at time. For the submersible we shall not set specific margins but evaluate the controller to ascertain its robustness.

### 3.5 Chapter Summary

The present chapter has developed a set of frequency domain specifications to which a controller can be designed. In order that the compensator may, once designed, be tested and validated, time domain specifications have also been presented. Finally, the basic ideas of compensator robustness were discussed in terms of modeling errors with multivariable phase and gain margin definitions given. In chapter 4, the control design methodology is developed and a design example offered and tested.

#### 4. MODEL-BASED COMPENSATOR AND CONTROLLER DESIGN

##### 4.1 Introduction

In this chapter, a compensator will be designed based on the Linear Quadratic Gaussian (LQG) with Loop Transfer Recovery (LTR) procedure. We will first discuss the Model-Based Compensator (MBC) and the augmented dynamics; then, the Loop Transfer Recovery (LTR) design procedure is employed to meet the frequency-domain specifications. A design example using the twenty knot linear model is then presented. Finally, we shall test the compensator design using both linear and nonlinear simulations.

The control specifications will be met by loop-shaping the singular values. In order to meet the performance specifications of small steady-state errors, we desire high DC gains. To ensure modeling errors will not cause closed-loop instability we desire a crossover of about 0.1 radians per second with a large roll-off after crossover. This will ensure attenuation of the high frequency modeling errors and sensor noise.

##### 4.2 Model-Based Compensator Structure

The MBC is a class of MIMO compensators which can be constructed using the results of optimal control theory (the linear quadratic state feedback problem) and optimal estimation theory (the Kalman filter). The MBC has the property that, when cascaded with a MIMO open-loop plant, the resultant closed-loop plant will be stable, provided the constant gain parameters discussed below are properly selected. Thus, the designer's objective is, given an open-loop plant, to select a compensator which ensures stability of the closed-loop system and achieves the desired loop shapes in the frequency domain using singular values. Figure 4.1 illustrates the desired feedback structure of the MIMO control system with the disturbances,  $d(s)$ , reflected to the plant input. Although Linear-Quadratic-Gaussian stochastic optimal control

theory is used to obtain the numerical solutions for the gains of the MBC, the implications of the word "optimal" should be deemphasized. This is, among other reasons, because the designer varies the free parameters, in a systematic way, without regard to stochastic optimality considerations, in order to obtain good compensators.

Figure 4.2, from reference [6], illustrates the internal state-space description of the MBC ( $\underline{K}(s)$ ) and the open-loop plant,  $\underline{G}_p(s)$ . Note that the  $\underline{A}$ ,  $\underline{B}$ , and  $\underline{C}$  matrices describing the plant appear in the compensator,  $\underline{K}(s)$ , as well as in the plant transfer function matrix,  $\underline{G}_p(s)$ . The term MBC is used due to the explicit way the nominal model of the open-loop plant,  $\underline{G}_p(s)$ , shows up in the compensator,  $\underline{K}(s)$ .

The open loop dynamics of the plant are

$$\dot{\underline{x}}(t) = \underline{Ax}(t) + \underline{Bu}(t) + \underline{Ld}(t) \quad (4.1)$$

$$\underline{y}(t) = \underline{Cx}(t) \quad (4.2)$$

where  $\underline{L}$  is a design parameter which may be varied so that an open-loop system can be constructed to reflect the specifications. The closed-loop compensated system will then be required to match this open-loop performance. The control-to-plant transfer function is

$$\underline{G}_p(s) = \underline{C}(s\underline{I} - \underline{A})^{-1}\underline{B}. \quad (4.3)$$

The MBC dynamics are

$$\dot{\underline{z}}(t) = [\underline{A} - \underline{BG} - \underline{HC}]\underline{z}(t) - \underline{He}(t) \quad (4.4)$$

$$\underline{u}(t) = -\underline{Gz}(t) \quad (4.5)$$

where  $\underline{z}(t)$  is the estimated state vector (of the same dimension as the plant state vector),  $\underline{r}(t)$  is the reference input vector,  $\underline{e}(t)$  is the

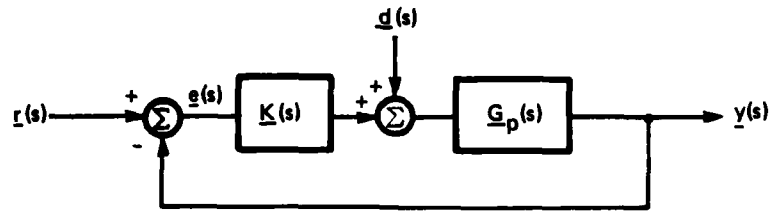


Figure 4.1 MIMO feedback system.

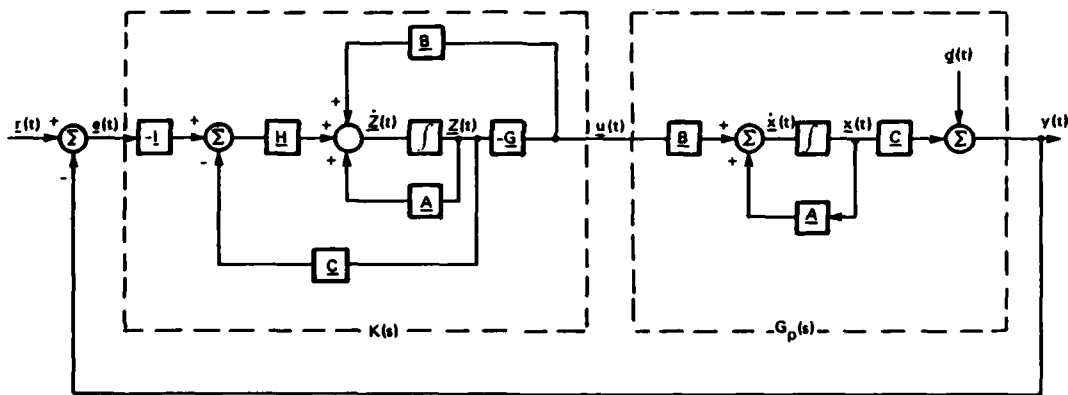


Figure 4.2. State space description of the MBC.

error vector ( $\underline{e}(t) = \underline{r}(t) - \underline{y}(t)$ ) and  $\underline{u}(t)$  is the output vector of the MBC. The control gain matrix,  $\underline{G}$ , and filter gain matrix,  $\underline{H}$ , are design results which together determine the poles and zeros of the MBC. The MBC transfer matrix,  $\underline{K}_{LOG}(s)$ , is given by

$$\underline{K}_{LOG}(s) = \underline{G}(s\underline{I} - \underline{A} + \underline{B}\underline{G} + \underline{H}\underline{C})^{-1} \underline{H} \quad (4.6)$$

where

$$\underline{u}(s) = \underline{K}_{LOG}(s)\underline{e}(s). \quad (4.7)$$

A closed loop representation of the cascaded plant and compensator is derived in reference [2] as

$$\begin{bmatrix} \dot{\underline{x}}(t) \\ \dot{\underline{w}}(t) \end{bmatrix} = \begin{bmatrix} \underline{A} - \underline{B}\underline{G} & \underline{B}\underline{G} \\ 0 & \underline{A} - \underline{H}\underline{C} \end{bmatrix} \begin{bmatrix} \underline{x}(t) \\ \underline{w}(t) \end{bmatrix} + \begin{bmatrix} \underline{L} & 0 \\ \underline{L} & -\underline{H} \end{bmatrix} \begin{bmatrix} \underline{d}(t) \\ \underline{r}(t) \end{bmatrix} \quad (4.8)$$

where a change of variables has been used with

$$\underline{w}(t) = \underline{x}(t) - \underline{z}(t). \quad (4.9)$$

The vector  $\underline{w}(t)$  is simply the error of state estimation.

The above  $2n$  dimensioned vector equation completely describes the closed-loop system. Given  $\underline{A}$ ,  $\underline{B}$ , and  $\underline{C}$ , the selection of  $\underline{H}$  and  $\underline{G}$  will determine the closed-loop dynamics from which one may calculate the closed-loop response to disturbances and/or command inputs. It can be shown [2,3,6] that closed-loop stability decomposes into two separate problems as follows:

1. Given  $\underline{A}$  and  $\underline{B}$ , find  $\underline{G}$  such that the real parts of the eigenvalues of  $(\underline{A} - \underline{B}\underline{G})$  are less than zero.

2. Given A and C, find H such that the real parts of the eigenvalues of (A - HC) are less than zero.

From linear system theory [10] it can be shown that the feedback system of Figure 4.2 can be made closed-loop stable by appropriate selection of H and G, provided that [A, B] is a stabilizable pair and [A, C] is a detectable pair. In fact, as discussed in Chapter 2, the twenty knot linear model satisfies the stronger controllability and observability conditions.

#### 4.3 Calculation of the Gain Matrices

The procedure for calculating G and H is based on the LQG stochastic optimal control theory [10, 16]. Recall that, in the Linear Quadratic Regulator problem we attempt to minimize the quadratic cost functional

$$J = \int [\underline{x}'(t) \underline{Q} \underline{x}(t) + \underline{u}'(t) \underline{R} \underline{u}(t)] dt \quad (4.10)$$

where the R matrix is the control weighting matrix and Q is the state weighting matrix.

The control gain matrix G is

$$\underline{G} = \underline{R}^{-1} \underline{B} \underline{P} \quad (4.11)$$

where R is an arbitrary symmetric, positive definite (mxn) matrix (m being the number of inputs and outputs) and P is the solution to the control algebraic Riccati equation (CARE)

$$\underline{Q} = -\underline{P} \underline{A} - \underline{A}' \underline{P} - \underline{Q} + \underline{P} \underline{B} \underline{R}^{-1} \underline{B}' \underline{P} \quad (4.12)$$

In this development Q is an arbitrary (nxn) symmetric, positive semi-definite matrix given as

$$\underline{Q} = \underline{N}' \underline{N} \quad (4.13)$$

such that  $[A, N]$  is detectable [2].

The filter gain matrix,  $H$ , is found using the Kalman filter algorithm with

$$H = FC'S^{-1} \quad (4.14)$$

where  $S$  is symmetric, positive semi-definite and is given as

$$S = MM' \quad (4.15)$$

and  $M$  is an arbitrary matrix of suitable dimensions with  $[A, M]$  stabilizable. The  $F$  matrix is the solution of the filter algebraic Riccati equation (FARE)

$$0 = FA + A'F + S - FC'\theta^{-1}CF \quad (4.16)$$

where  $\theta$  is an arbitrary, symmetric,  $(mxm)$ , positive definite matrix.

The control engineer has considerable freedom in selecting the parameters of the design. In fact, one may use  $L$ ,  $N$ ,  $M$ ,  $R$  and  $\theta$  directly as design parameters. Obviously, this freedom is of great disadvantage without a method of rationally and systematically selecting these parameters. The LTR method provides such an algorithm. Before the LTR procedure is presented, we shall augment the plant dynamics as discussed below.

#### 4.4 Control Surface Dynamics and Augmentation

##### 4.4.1 Actuator Dynamics and Augmentation

In order to reduce the number of neglected dynamics, it is desirable to include in the linear model the dynamics of the actuators (rudder and sternplanes). The actuators are more accurately described by second order systems (Table 4.1); however, as the damping ratio approaches unity, the second order harmonics disappear. In order to reduce the model size and because the control surfaces are heavily

the actuators were satisfactorily approximated with a first order representation of the form

$$\frac{(1/\tau)}{s + (1/\tau)}$$

with the constant  $\tau$  being derived from the original second order dynamics.

TABLE 4.1: ACTUAL DYNAMICS (Second Order)

Sternplanes:	$\omega = 3.14$ radians/sec $\xi = .9$ $\sigma = \xi\omega = 2.83$ radians/sec
Rudder:	$\omega = 2.51$ radians/sec $\xi = .9$ $\sigma = \xi\omega = 2.26$ radians/sec

Now, from reference [13], using the definition of the time constant for a second order system with critical damping

$$\tau = 1/\sigma$$

we find

$$1/\tau_r = 2.83/\text{sec}$$

$$1/\tau_s = 2.26/\text{sec}$$

As the projected crossover frequency is on the order of one tenth of a radian per second, it was clear that the actuator dynamics would not have a large influence on the design. However, in order to increase roll-off near crossover, it was decided to use lag compensation at 0.1 radians per second instead of the approximate control surface dynamics. This will increase the roll-off above the crossover frequency, making the vehicle less susceptible to modeling errors and high frequency sensor noise. Therefore, the system was augmented with two lag compensators as shown in Figure 4.3.

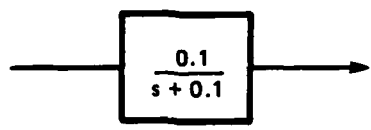


Figure 4.3. First order lag compensation block diagram.

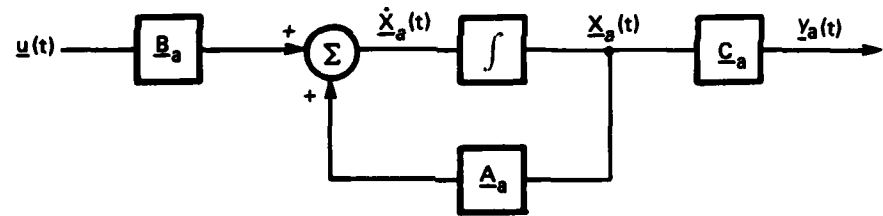


Figure 4.4. State space representation of the augmented dynamics.

The state space representation of the augmented dynamics is shown in Figure 4.4. For the lag compensation previously developed we have

$$\underline{A}_a = \begin{bmatrix} -0.1 & 0.0 \\ 0.0 & -0.1 \end{bmatrix}$$

$$\underline{B}_a = \begin{bmatrix} 0.1 & 0.0 \\ 0.0 & 0.1 \end{bmatrix}$$

$$\underline{C}_a = \begin{bmatrix} 1.0 & 0.0 \\ 0.0 & 1.0 \end{bmatrix}$$

and  $\underline{G}_a(s)$ , the 2 by 2 augmentation transfer matrix is

$$\underline{G}_a(s) = \underline{C}_a(sI - \underline{A}_a)^{-1} \underline{B}_a. \quad (4.19)$$

#### 4.4.2 Overall System Model

The MIMO feedback system with the augmented dynamics  $\underline{G}_a(s)$  is as shown in Figure 4.5. Since  $\underline{G}_a(s)$  is decided by the control designer, it is justifiably part of the overall compensation  $K(s)$  (it is this overall compensation that is incorporated in the simulation), with

$$K(s) = \underline{G}_a(s) K_{LQG}(s) \quad (4.20)$$

and it is only the compensation denoted as  $K_{LQG}(s)$  which will be designed by the LQG/LTR methodology presented later.

For designing  $K_{LQG}(s)$  we first need to define the "plant" transfer matrix  $\underline{G}(s)$  as

$$\underline{G}(s) = \underline{G}_p(s)\underline{G}_a(s) \quad (4.21)$$

as illustrated in Figure 4.5. Note that the "plant" consists of the nominal plant,  $\underline{G}_p(s)$ , and the augmented dynamics  $\underline{G}_a(s)$ . Also note that the input to the "plant",  $\underline{u}(t)$  is not the physical input  $\underline{u}_p(t)$ , but that the output  $\underline{y}(t)$  is the same for either plant definition (augmented or unaugmented). In the present design  $K_{LQG}(s)$ ,  $\underline{G}_a(s)$ , and  $\underline{G}_p(s)$  are all two by two transfer matrices.

In the frequency domain the nominal plant,  $\underline{G}_p(s)$ , is defined as

$$\underline{G}_p(s) = \underline{C}_p(sI - \underline{A}_p)^{-1} \underline{B}_p \quad (4.22)$$

where  $\underline{A}_p$  is a ten by ten matrix,  $\underline{B}_p$  is a ten by two matrix and  $\underline{C}_p$  is a two by ten matrix. The development of the specific plant matrices was presented in Chapter 2.

Combining the augmentation dynamics and nominal plant yields an overall plant transfer matrix

$$\underline{G}(s) = \underline{C}(sI - \underline{A})^{-1} \underline{B} \quad (4.23)$$

where  $\underline{A}$  is a 12 by 12 matrix,  $\underline{B}$  is a 12 by 2 matrix and  $\underline{C}$  a 2 by 12 matrix. Figure 4.6 displays the state space, time domain representation of the overall open-loop "plant".

To develop the form of the  $\underline{A}$ ,  $\underline{B}$ , and  $\underline{C}$  matrices we start by defining the 12 by 1 state vector as

$$\underline{x} = \begin{bmatrix} \underline{x}_p \\ \underline{x}_a \end{bmatrix} \quad (4.24)$$

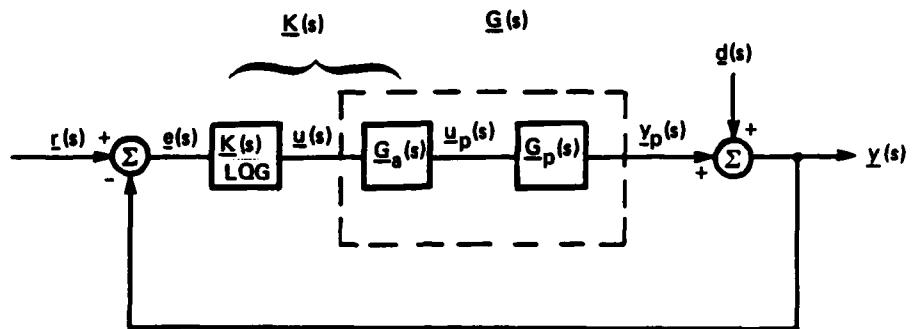


Figure 4.5. Overall compensated system.

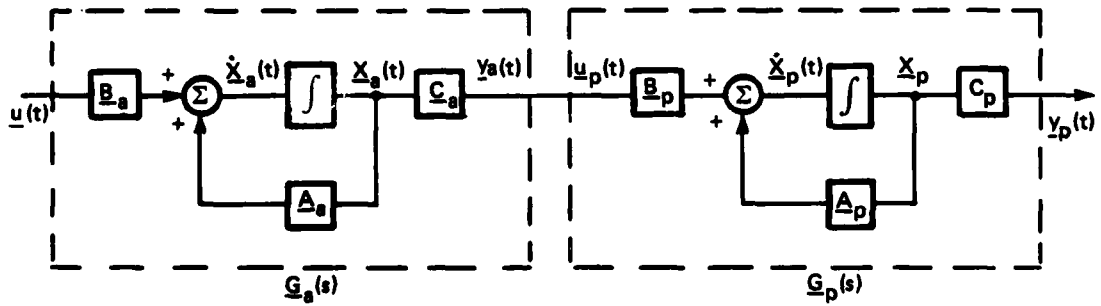


Figure 4.6. Nominal open-loop plant with augmentation.

where  $\underline{x}(t)$  consists of the original ten state variables listed in Table 2.1 and  $x_a(t)$  are the two augmentation states.

The overall plant in state space form is now given by

$$\dot{\underline{x}}(t) = \underline{A}\underline{x}(t) + \underline{B}u(t) \quad (4.25)$$

$$\underline{y}(t) = \underline{C}\underline{x}(t) \quad (4.26)$$

where

$$\underline{A} = \left[ \begin{array}{c|c} \underline{A}_p(10 \times 10) & \underline{B}_p \underline{C}_a \\ \hline \underline{0} (2 \times 10) & \underline{A}_a \end{array} \right]$$

$$\underline{B} = \left[ \begin{array}{c} \underline{0} \\ \hline \underline{B}_a \end{array} \right]$$

$$\underline{C} = \left[ \begin{array}{cc} \underline{C}_p(2 \times 10) & \vdots \underline{0} \\ \vdots & (2 \times 2) \end{array} \right]$$

#### 4.4.3 Augmented Plant Dynamics

The addition of the first order lag compensation at 0.1 radian per second increased the order of the plant to twelve. This augmentation added two poles at 0.1 but did not change the transmission zeros.

The singular values of the augmented open-loop plant were calculated and are shown in Figure 4.7. As expected, the augmented plant singular values roll-off more quickly at frequencies above 0.1 radian per second as compared to the unaugmented plant. The crossover frequencies occur at 0.48 and 0.1 as compared to the unaugmented plant crossovers of 1.0 and 0.13 radians per second. The faster roll-off should enable the designer to more easily meet the crossover and robustness specifications. With the augmented plant A, B, and C matrices (shown in Table C.3 of Appendix C) developed, the loop transfer recovery control design methodology will now be discussed.

#### 4.5 Compensator Design Methodologies

The LTR procedure allows one to systematically design an LQG-based compensator, K(s), given a nominal open-loop plant G<sub>p</sub>(s). We shall systematically select and iterate on the free design parameters L, θ, and R. Specifically, we desire to shape the singular values of the loop transfer matrix, T(s), where

$$\underline{T}(s) = \underline{G_p}(s)\underline{K}(s) \quad (4.27)$$

over the appropriate frequency range such that the specified performance/robustness properties of good command following, output disturbances rejection and insensitivity to modeling errors are met. The LQG/LTR method presented here (and detailed in references [2] and [5]), consists of first shaping the singular values of the Kalman filter loop transfer matrix and then recovering the same loop transfer matrix for T(s) using the dual of the Kwackernaack recovery method [10].

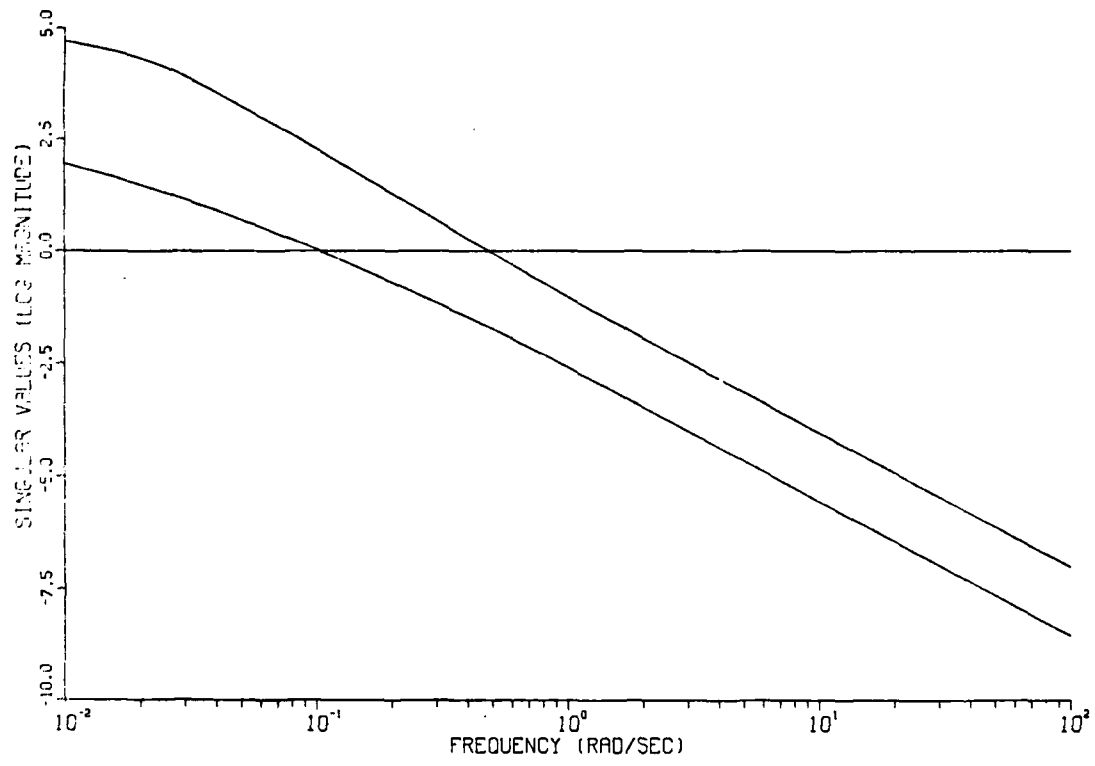


**Figure 4.7: Singular Values of Twenty Knot Augmented Plant**

The first step is based on the Kalman filter (KF) frequency domain equality.

$$(\underline{I} + \underline{G}_{KF}(s)) + (\underline{I} + \underline{G}_{KF}(s))^* = \underline{I} + \frac{1}{\mu} \underline{G}_{FOL}(s) \underline{G}_{FOL}(s)^* \quad (4.28)$$

where

$$\underline{G}_{FOL}(s) = \underline{C}(\underline{s}\underline{I} - \underline{A})^{-1} \underline{L} \quad (4.29)$$

and

$$\underline{G}_{KF}(s) = \underline{C}(\underline{s}\underline{I} - \underline{A})^{-1} \underline{H}. \quad (4.30)$$

The A and C matrices are for the augmented plant, H is for the filter gain matrix and  $\mu$  and L are design parameters. At low frequencies it can be shown [2] that as the frequency approaches zero,

$$\sigma_i[\underline{G}_{KF}(s)] = \sigma_i[\frac{1}{\sqrt{\mu}} \underline{G}_{FOL}(s)]. \quad (4.31)$$

Thus the first step is to select L and  $\mu$  such that the specifications (command following, disturbance rejection and crossover) in the frequency domain are met by

$$\sigma[\underline{G}_{FOL}(j\omega)]. \quad (4.32)$$

Now the FARE, of the form

$$\underline{0} = \underline{A}'\underline{F} + \underline{F}\underline{A} + \underline{L}\underline{L}' - \underline{F}\underline{C}'\underline{\theta}^{-1}\underline{C}\underline{F} \quad (4.33)$$

is solved for F using  $\mu$  and  $\underline{\theta}$  as arbitrary design parameters (usually  $\underline{\theta}$  is taken as the identity matrix due to considerations detailed in reference [12]). The KF gains are then

$$\underline{H} = \underline{F}\underline{C}'\underline{\theta}^{-1} \quad (4.34)$$

The singular values of the filter transfer matrix,  $\underline{G}_{KF}(s)$ , are made to match, as closely as possible, the singular values of  $\underline{G}_{FOL}(s)$ , by iterating on the scalar  $\mu$ . That is, we select  $\mu$  such that for the previously obtained  $\underline{L}$  (selected to meet the stated frequency-domain specifications) we have

$$\sigma_i[\underline{G}_{KF}(s)] = \sigma_i\left[\frac{1}{\sqrt{\mu}} \underline{G}_{FOL}(s)\right] \quad (4.35)$$

At this point the robustness of the KF is checked by ensuring

$$\sigma[\underline{I} + \underline{G}_{KF}(j\omega)] \geq 1 \quad (4.36)$$

$$\sigma[\underline{I} + \underline{G}_{KF}^{-1}(-j\omega)] \geq \frac{1}{2} \quad (4.37)$$

These robustness properties are discussed in reference [12].

The LQG compensator is now designed using LTR by solving the CARE for  $\underline{P}$  which is of the form

$$\underline{0} = -\underline{PA} - \underline{A}'\underline{P} - \underline{Q} + \underline{PBR}^{-1}\underline{B}'\underline{P} \quad (4.38)$$

where

$$\underline{Q} = q\underline{C}'\underline{C} \quad (4.39)$$

and  $q$  (a positive scalar) and  $\underline{R}$  (usually taken as the identity matrix) are the design parameters. The control gain matrix  $\underline{G}$  is then

$$\underline{G} = \underline{R}^{-1}\underline{B}'\underline{P} . \quad (4.40)$$

The singular values of the resultant loop transfer matrix  $\sigma[\underline{T}(j\omega)]$  are now calculated where

$$\underline{T}(s) = \underline{G}(s)\underline{K}_{LQG}(s). \quad (4.41)$$

The designer iterates on  $q$  (and possibly  $R$ ) until

$$\sigma[\underline{T}(j\omega)] \approx \sigma[\underline{G}_{KF}(j\omega)] \quad (4.42)$$

over reasonable frequency ranges.

For all minimum phase systems, the LTR method guarantees that the singular values of  $\underline{T}(s)$  and  $\underline{G}_{KF}(s)$  will coincide as the scalar,  $q$ , approaches infinity. In NMP systems, if all non-minimum phase zeros are beyond the maximum crossover of  $\underline{G}_{KF}(s)$ , then the singular values of  $\underline{T}(s)$  and  $\underline{G}_{KF}(s)$  will coincide satisfactorily at low frequencies. If non-minimum phase zeros exist at frequencies below crossover, it appears that there will be basic limitations on command-following and disturbance rejection [2]. Precisely how to "cure" this is not known at the present time.

Finally, if the designer has available an estimate of the modeling error  $\underline{L}_p(s)$ , the robustness of the compensated system may be checked by ensuring

$$\sigma_{\max} [\underline{L}_p(j\omega) - \underline{I}] < \sigma_{\min} [\underline{I} + \underline{T}^{-1}(j\omega)] \quad (4.43)$$

$$\sigma_{\max} [\underline{L}_p^{-1}(j\omega) - \underline{I}] < \sigma_{\min} [\underline{I} + \underline{T}(j\omega)]. \quad (4.44)$$

Using the augmented, twenty knot linear model, a compensator will now be designed. It should be noted that an accurate estimate of the modeling error was not available to the designer. Therefore, the robustness properties were not examined in terms of  $\underline{L}_p(s)$ .

#### 4.6 Compensator Design Example

The first step of the design procedure is to select an arbitrary  $\underline{L}$  matrix such that the performance specifications are met. Recall that the frequency-domain specifications stated that crossover should be 0.13 radians per second or less, due to the natural crossover frequency of the open-loop plant singular values, the frequency of wave encounter and the NMP zero at 0.488.

The  $\underline{L}$  matrix was selected such that the singular values would be "tied together" both at low and high frequencies with crossover in the vicinity of 0.1 radians per second. The particular  $\underline{L}$  to accomplish this was selected as follows.

At low frequency, the KF equality reduces to the approximation

$$\left[ \frac{1}{\sqrt{\mu}} \underline{G}_{FOL}(j\omega) \right] \approx \sigma[\underline{G}_{KF}(j\omega)] \quad (4.45)$$

which implies

$$\frac{1}{\sqrt{\mu}} \underline{C}(j\omega \underline{I} - \underline{A})^{-1} \underline{L} = \underline{G}_{KF}(j\omega) \quad (4.46)$$

The idea is to select  $\underline{L}$  such that  $\underline{C}(\underline{s}\underline{I} - \underline{A})^{-1} \underline{L} = \sqrt{\mu} \underline{I}$ . As the frequency approaches zero

$$\underline{C}(-\underline{A}^{-1}) \underline{L} = \sqrt{\mu} \underline{I}. \quad (4.47)$$

Therefore, we pick  $\underline{L}$  such that

$$\underline{I} = \underline{C}\underline{A}^{-1} \underline{L} \quad (4.48)$$

which yields

$$\underline{L} = \sqrt{\mu} \underline{A}\underline{C}'(\underline{C}\underline{C}')^{-1}. \quad (4.49)$$

5 76bvns system, the A matrix is singular. Since L is arbitrary, let A = A where A is made non-singular by replacing the zeros in the last two diagonal entries of A with unity. The form of A in relation to C, makes A appear as an identity matrix and since the C matrix is unitary (CC' = I), we have

$$\underline{L} = \sqrt{\mu} \underline{C}' \quad (4.50)$$

at low frequencies.

At high frequencies, we find the KF equality leads to the approximation

$$G_{KF}(j\omega) = \left( \frac{1}{j\omega/\mu} \right) \underline{C} \underline{I} \underline{L} = \frac{\underline{C} \underline{L}}{j\omega/\mu} = \underline{I} \quad (4.51)$$

Thus we desire

$$\underline{C} \underline{L} = \underline{I} \quad (4.52)$$

which leads to

$$\underline{L} = \sqrt{\mu} \underline{C}' (CC') = \sqrt{\mu} \underline{C}' \quad (4.53)$$

Therefore at both high and low frequencies tying the singular values together requires L =  $\sqrt{\mu} \underline{C}$ . We only have to iterate on the scalar  $\mu$  to obtain the desired crossover characteristics of  $\sigma_i[G_{POL}(j\omega)]$ . It was found that for  $\mu = .01$  the singular values of G<sub>POL</sub>(s) (Figure 4.8) exhibited the desired characteristics of high DC gains (60 dB at  $\omega = .0001$ ) and a crossover of 0.1 radian per second.

Using the L matrix thus generated and iterating on the scalar  $1/\sqrt{\mu}$ ,

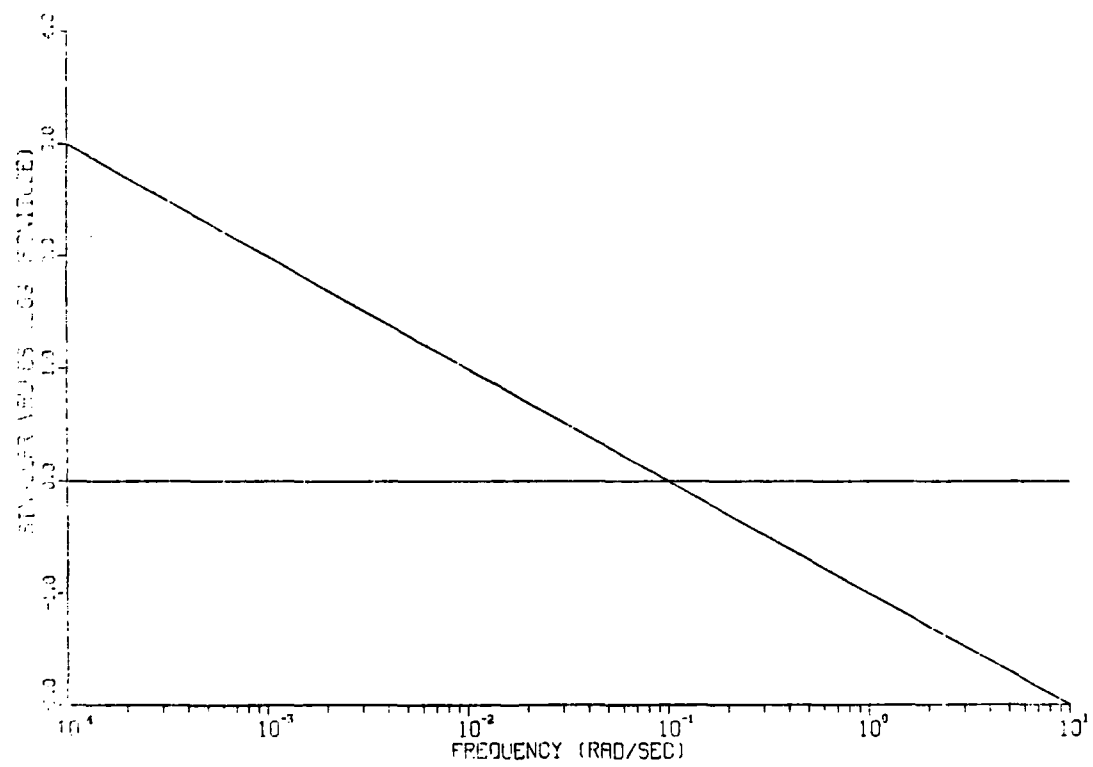


**Figure 4.8: Singular Values of  $G_{POL}(s)$**

the FARE was solved, the filter gain matrix,  $\underline{H}$ , generated and the singular values of the KF transfer matrix ( $\sigma[\underline{G}_{KF}(j\omega)]$ ) calculated. With  $1/\sqrt{\mu}$  equal to 1, the singular values of  $\underline{G}_{KF}(s)$  were found to exactly match the singular values of  $\underline{G}_{POL}(s)$ . Figure 4.9 shows the singular values of  $\underline{G}_{KF}(s)$  with  $1/\sqrt{\mu} = 1$  and  $\underline{L} = .1\underline{C}'$ .

At this point, the poles of the filter ( $\lambda_i[\underline{A}-\underline{H}\underline{C}]$ ) were calculated. All had negative real parts, thus verifying the guaranteed stability of the filter. Further, the robustness of the filter was checked by evaluating

$$\sigma_i[\underline{I}+\underline{G}_{KF}^{-1}(j\omega)] \quad (4.55)$$

and

$$\sigma_i[\underline{I}+\underline{G}_{KF}^{-1}(j\omega)]. \quad (4.56)$$

The filter robustness requirements discussed earlier were met as both sets of singular values maintained magnitudes of unity or greater.

The singular value loop shapes of the filter are now recovered for the compensator. The CARE is solved with  $\underline{R} = \underline{I}$  and the result used to calculate the control gain matrix,  $\underline{G}$ . The singular values of the resultant loop transfer function ( $\sigma_i[\underline{T}(j\omega)]$ ) are generated and compared to the KF singular values. The designer iterates on the scalar  $q$  (where  $\underline{Q} = q\underline{C}'\underline{C}$  in the CARE) until a satisfactory match is obtained over the frequency range of interest. As shown in Figure 4.10, a  $q$  of 100 yielded satisfactory results with a crossover at approximately .065 radians per second and DC gains of 55 dB (at .0001). (In fact, larger values of  $q$  allowed for crossovers and DC gains more closely approaching the KF values but the controller gains subsequently generated were found to saturate the sternplanes and/or cause the rate limits to be exceeded.)

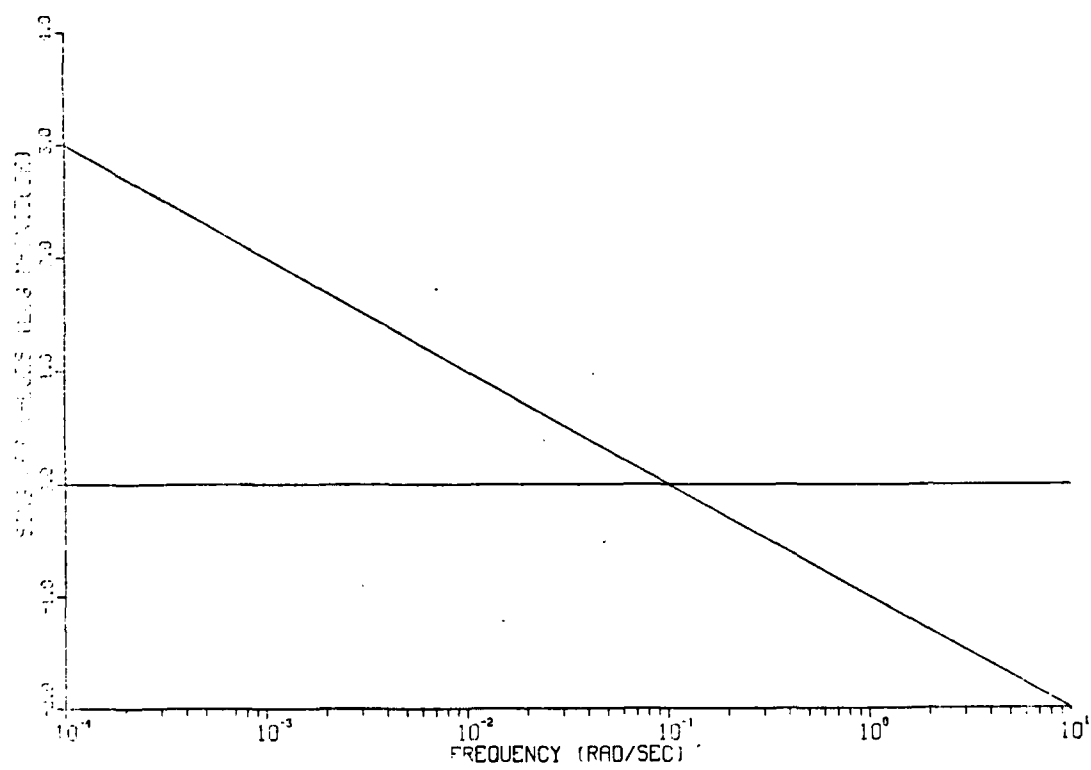
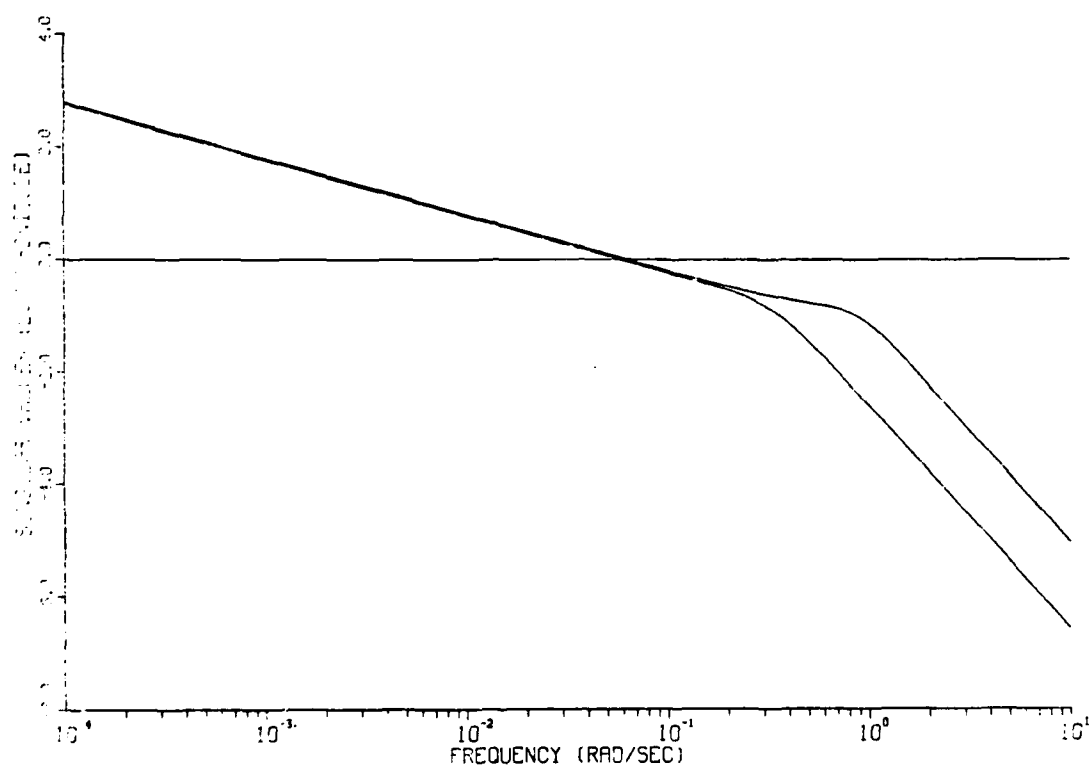


Figure 4.9: Singular Values of  $G_{NF}(s)$



**Figure 4.10: Singular Values of the Compensated Open-Loop System**

Notice the very narrow spread at crossover between the minimum and maximum singular values. Also, at frequencies above 1.0 radians per second, the roll-off approaches 80 dB per decade. This conforms to the Bode-Horowitz condition that all physical systems must exhibit at least two pole roll-off. This roll-off will ensure rapid attenuation of high frequency modeling errors and sensor noise. Further, the roll-off at crossover as predicted by Bode is approximately 20 dB [7]. The presence of a non-minimum phase zero at 0.488 has not prevented the LTR from being accomplished. Its presence however, might possibly have caused the delay in rolloff exhibited by the maximum singular value.

The robustness of the overall loop transfer matrix,  $\underline{T}(s)$ , can now be determined. Figures 4.11 and 4.12 plot the singular values of the return difference ( $\sigma_i[\underline{I} + \underline{T}(j\omega)]$ ) and inverse return difference ( $\sigma_i[\underline{I} + \underline{T}^{-1}(j\omega)]$ ) respectively. Using the gain and phase margins as defined in Chapter 3, we find for additive error

$$GM = [-4.73 \text{ dB}, 11.2 \text{ dB}]$$

$$PM = [-41.5 \text{ deg}, 41.5 \text{ deg}]$$

For multiplicative errors we have

$$GM = [\text{minus infinity}, 6 \text{ dB}]$$

$$PM = [-60 \text{ deg}, 60 \text{ deg}]$$

Thus, the overall loop transfer matrix is quite robust and therefore relatively insensitive to modeling errors which may exist.

The compensator gains generated (found in Table C.4 of Appendix C), will now be used in the linear and nonlinear simulations to ascertain the vehicle response to various reference inputs and initial conditions. The controller will be evaluated in terms of the time-domain specifications delineated in Chapter 3.

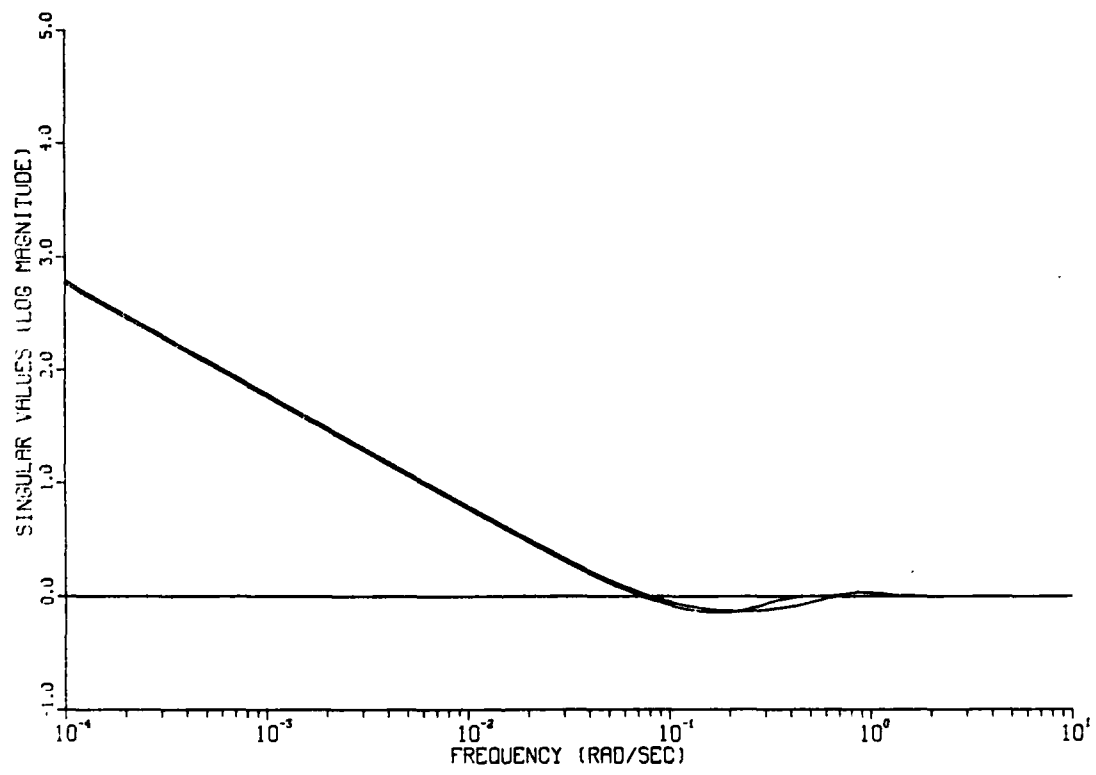


**Figure 4.11: Singular Values of  $[I+T(j\omega)]$**

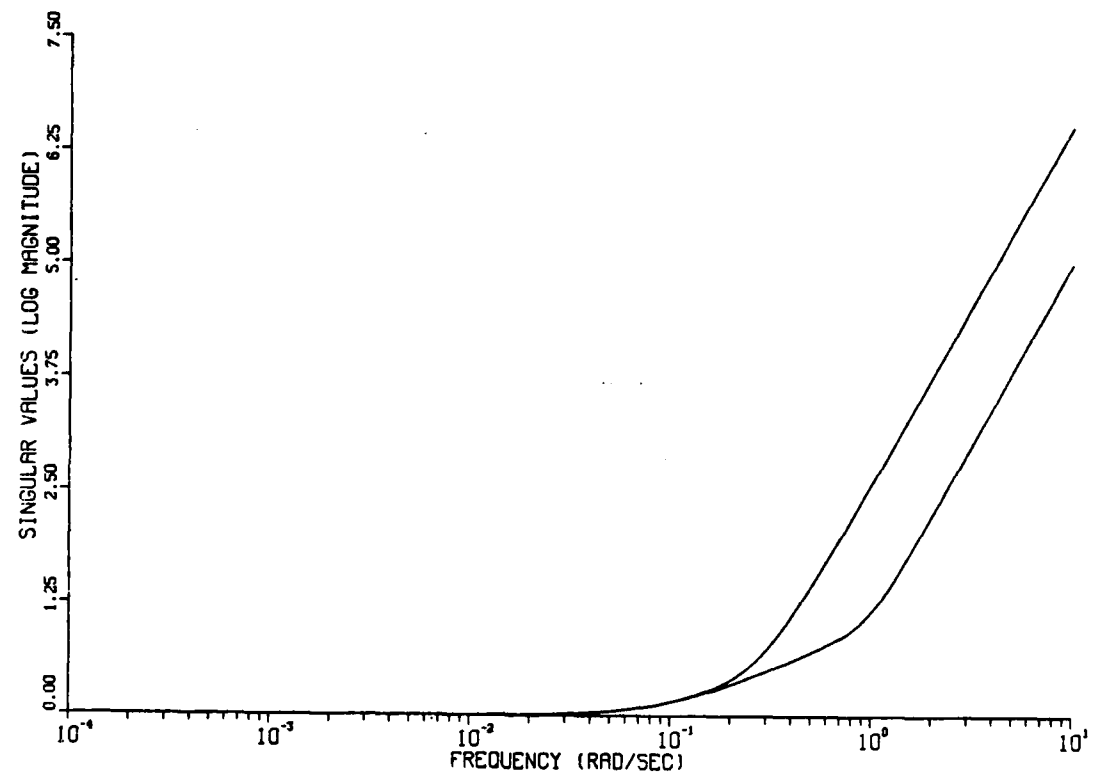


Figure 4.12: Singular Values of  $[I + T^{-1}(j\omega)]$

#### 4.7 Compensated System Response

##### 4.7.1 Simulation

Using the linearized model of the submarine at twenty knots (A, C, and C) and the filter and control gains (H and G) designed for that model, the compensator was tested via a computer simulation. The true test of a compensator is whether it adequately controls the vehicle and meets the specifications. Given that there is no actual test platform, the alternative is a simulation which incorporates the dynamics of the vehicle (as modeled by the equations of motion) and the compensator effects including any augmentation. Both linear and nonlinear, simulations were developed, solving the linearized and nonlinear equations of motion respectively. Thus, one may ascertain how well a linear compensator design is able to control the nonlinear model of the vehicle and critically compare this with the linear model response. Figure 4.5 illustrates the simulated, closed-loop system.

The simulation allows step and ramp perturbations to be input. Free surface effects, random noise and control surface rate limits were not modeled. Further details of the SUBMODEL program can be found in reference [18].

##### 4.7.2 Initial Conditions and Reference Inputs

When the depth and heading controller is initially activated, it will have to compensate for step commands as the ordered depth and heading will almost certainly be different from the depth and course the vehicle is presently maintaining. During manual control it is expected that the course will be maintained within two or three degrees of that ordered and the depth maintained to within 10 feet. To ensure a practical controller, it was desired that the compensator be capable of withstanding simultaneous step commands of 10 degrees and 30 feet. Additionally, the controller was tested with ramp inputs in heading and depth to ensure it could be utilized to automatically change the vehicle's course and depth over greater ranges. Specifically, the

compensated system was subjected to a ramp course change of 30 degrees and a ramp depth change of 50 feet, both input over 100 seconds. The ramp inputs were imposed separately.

#### 4.7.3 Error Limits

Through repeated testing, it was found that error limits (internally limited within the simulations) of 10 degrees in heading and 10 feet in depth offered satisfactory results for the twenty knot model. These error limits prevented excessive control surface deflection and also prevented the rate limits mentioned in Chapter 3 from being exceeded.

#### 4.7.4 Linear and Nonlinear Responses to Step Inputs

The compensated nonlinear responses to simultaneous step commands of 10 degrees and 30 feet are shown in the plots of Figure 4.13. The linear and nonlinear state responses were very similar with the major difference between the two being that the linear simulations showed less error in psi and z at the end of the run. This is to be expected as the compensator gains were designed using the linear model of the submarine. The errors for both the linear and nonlinear simulations were small and growing smaller as time progressed due to the integrator action.

The time domain specifications for the compensator are easily met whether controlling the linear or nonlinear model. The linear model heading error was less than ten percent (one degree) at 28 seconds while the depth error was within 10 percent (three feet) in 54 seconds. The nonlinear model has settling times of 71 and 78 seconds respectively. The settling time specification at 20 knots was 200 seconds.

The error at 200 seconds for the linear model was 0.8 percent in heading and 1.0 percent in depth which is well within the three percent specification. For the nonlinear model, the errors at 200 seconds are 2.245 and 1.1 percent and at 300 seconds are 0.7 and 0.5 percent.

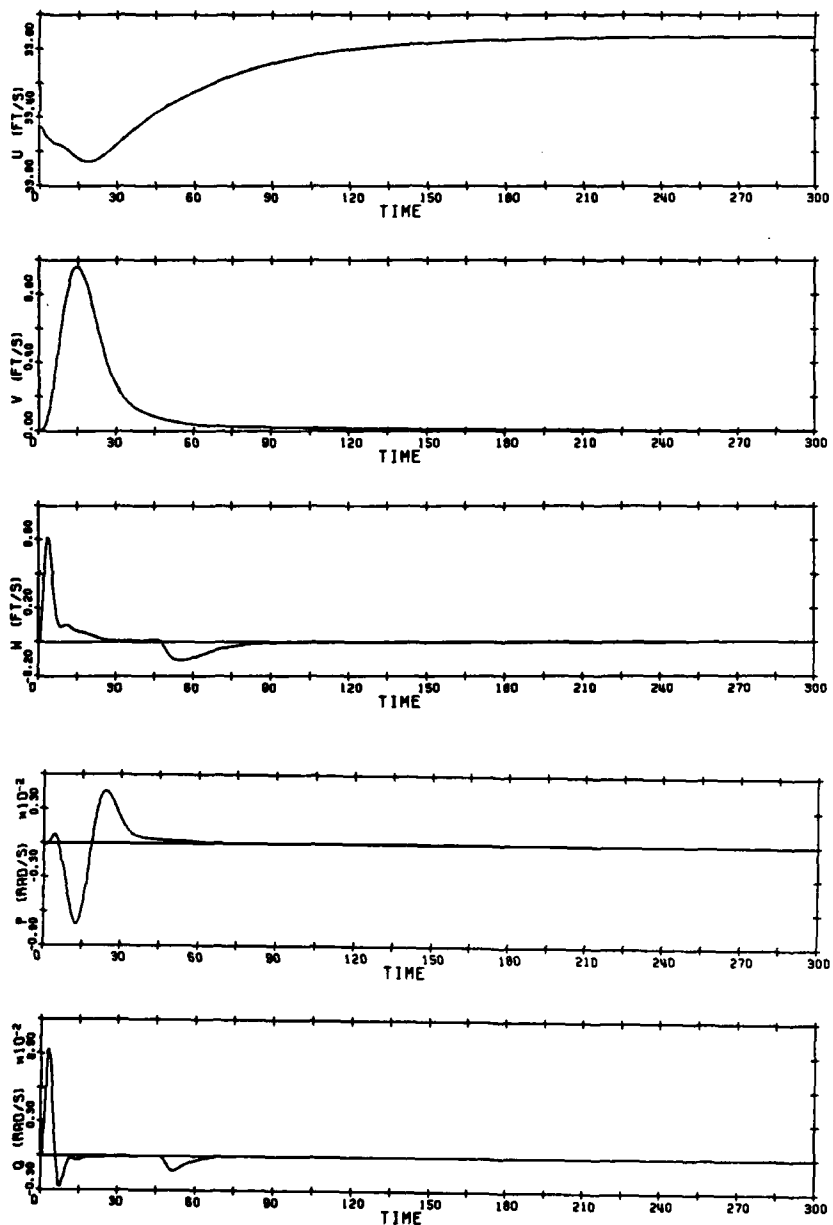


**Figure 4.13: Step Response of the Twenty Knot Compensated Nonlinear Model**

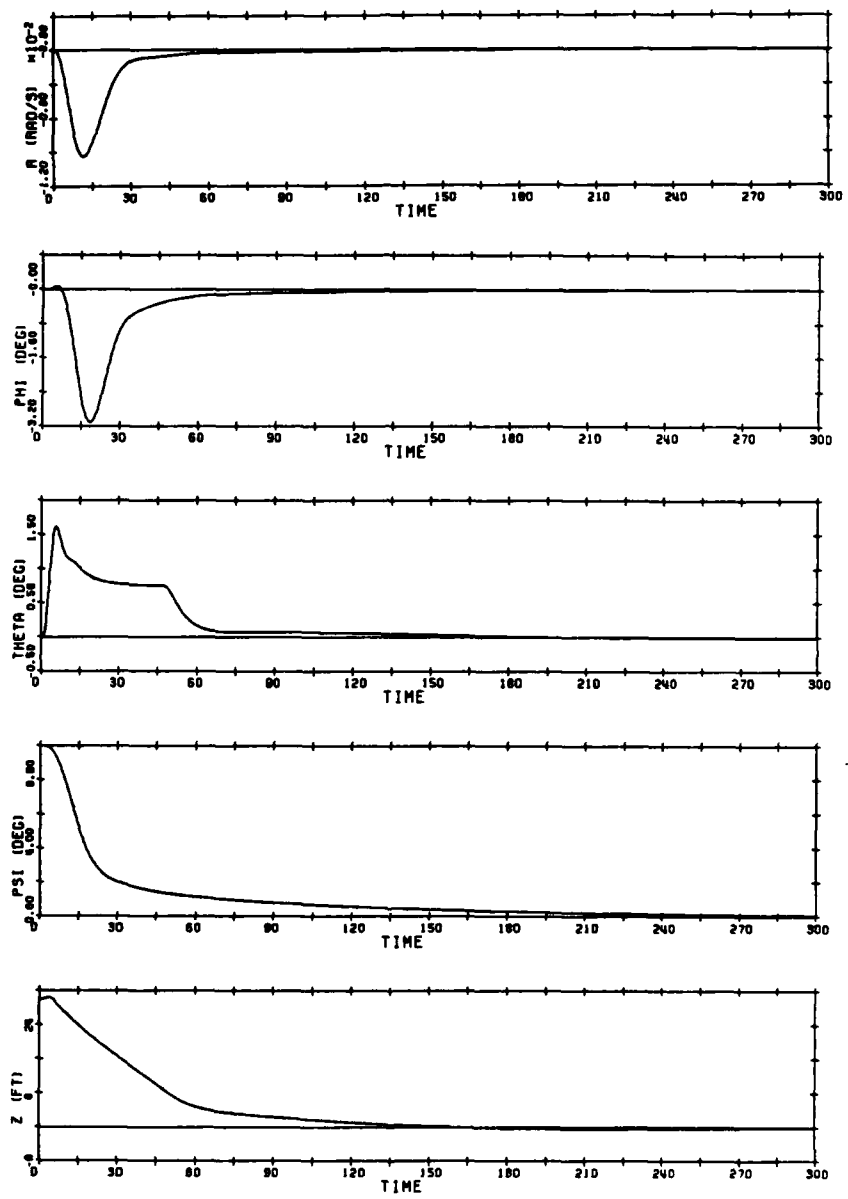


**Figure 4.13: Step Response of the Twenty Knot Compensated Nonlinear Model**

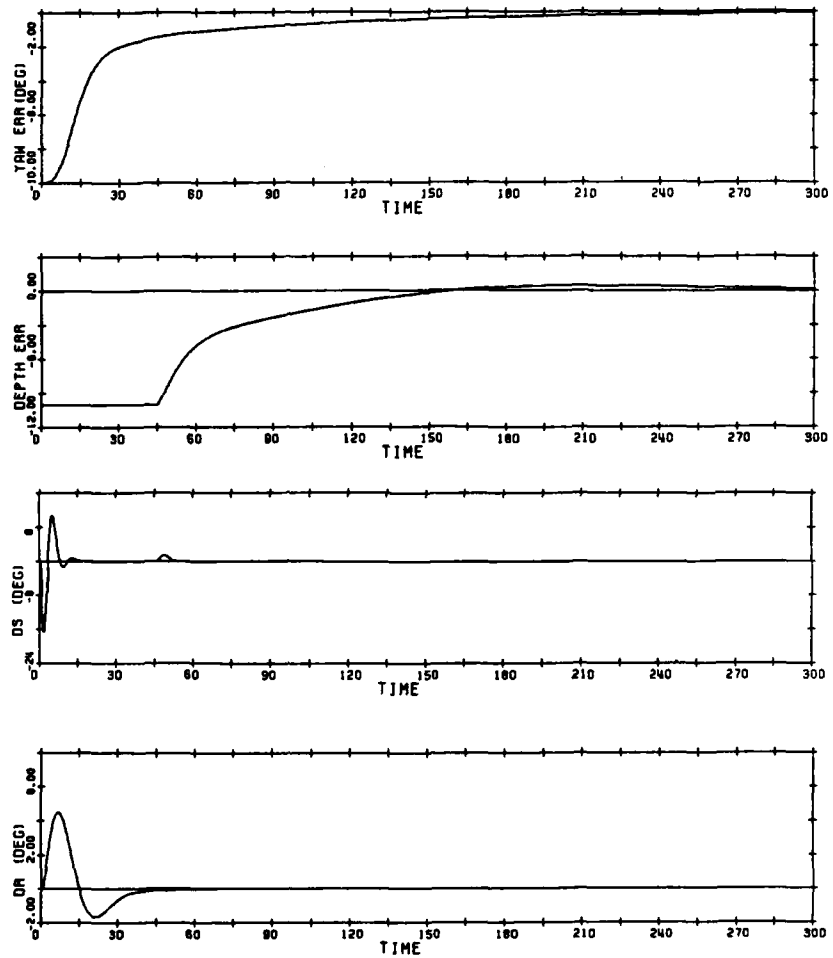


**Figure 4.13: Step Response of the Twenty Knot Compensated Nonlinear Model**

Initial control surface deflections were, of course, the same for both models (same gains and initial errors). The maximum rudder angle is 4.5 degrees at seven seconds and the largest sternplane deflection is 16.2 degrees after two seconds. Thus, the rate limits were not exceeded nor were the control surface deflections near saturation (40 degrees).

Note the type of control action which the design procedure yields. One finds that essentially all the control surface movement comes in the first thirty seconds. This is due to the fact that the controller "believes" it "knows" precisely how the vehicle will respond; and thus, it gives large initial control actions and then allows the vehicle dynamics to take over and "carry" the vehicle to the reference position. Therefore, we see rapid initial reductions in error as the vehicle is allowed to glide to the desired position. Although it cannot be seen on the plots, there is some residual control deflection tending to take the vehicle toward zero steady state error.

#### 4.7.5 Linear and Nonlinear Ramp Responses

Linear and nonlinear simulations were conducted to ascertain whether the controller could response adequately to ramp inputs used to turn or change vehicle depth. A 30 degree turn was first conducted with the nonlinear model responses for psi, z, heading error, depth error and control action shown in Figure 4.14. The linear model showed the submersible reaching steady state at 60 seconds after the ramp input ceased (160 seconds simulation time) with a heading error of 0.33 percent. The depth excursion was essentially zero. In the nonlinear case the submarine is within 3 percent (one degree) of the ordered 30 degree heading 100 seconds after the ramp input ceased and was still approaching 30 degrees (29.7) at 300 seconds. The maximum depth excursion if 3.3 feet during the turn and is within 0.35 feet at the end of the simulation. Thus the "level" turn specification (15 feet allowed at 20 knots) was met by the controller for both the linear and nonlinear models. Control actions were well behaved.

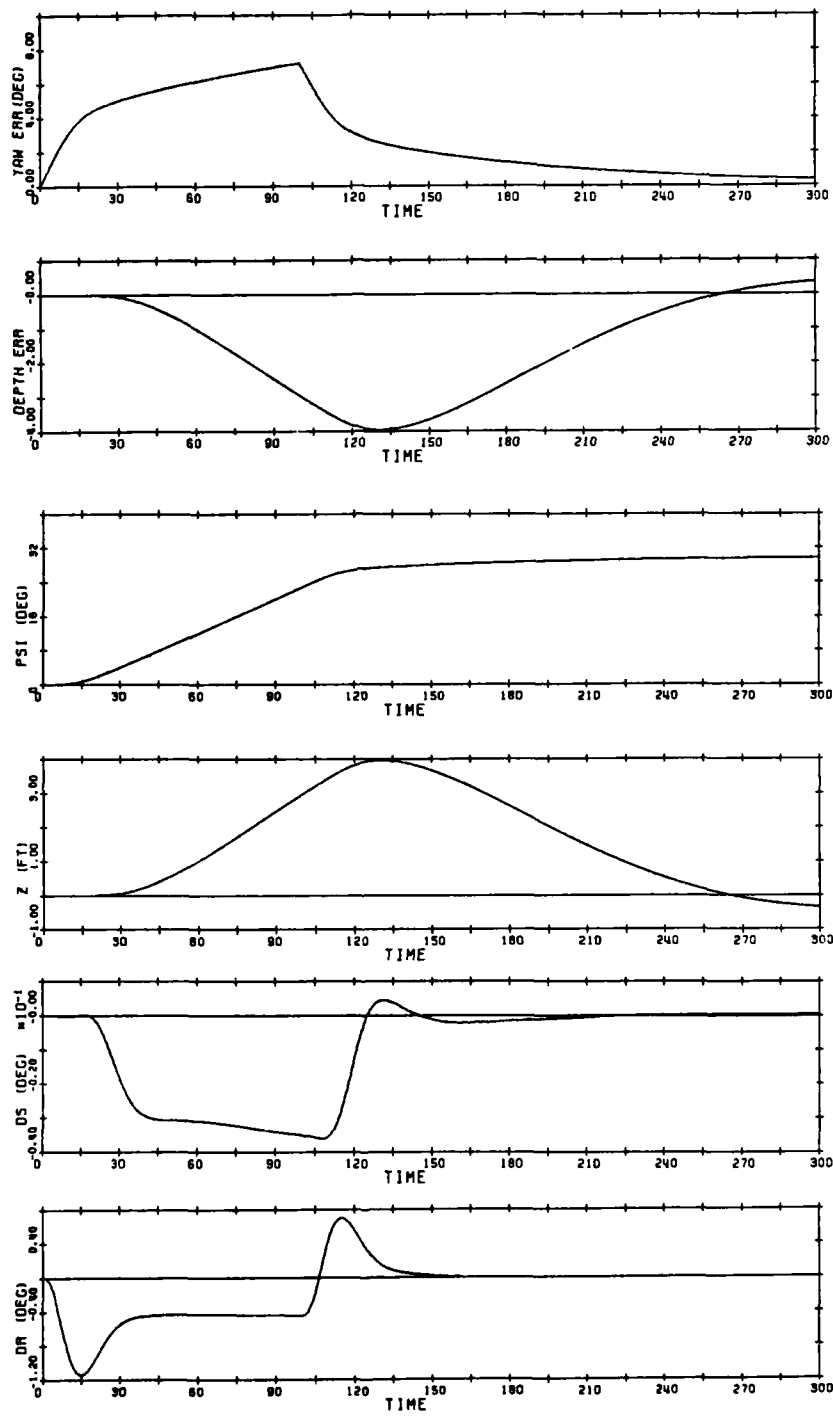


**Figure 4.14: Thirty Degree Ramp Response of the Compensated Nonlinear Model**

A depth change of 50 feet was also simulated with excellent results. Both the linear and nonlinear simulations showed practically no course deviation during the ramp depth change. The linear response showed the vehicle reaching 50 feet some 60 seconds after the input with a 0.47 foot overshoot (one percent) and a 0.3 percent (and decreasing) depth error at 300 seconds. The nonlinear model response (Figure 4.15) shows the ordered depth being reached 48 seconds after termination of the ramp input with a 1.3 foot overshoot (2.6 percent) and an error at 300 seconds of 0.7 percent (and decreasing). Again, the control design more than adequately meets the specifications.

Other ramp inputs were imposed with similar results. The compensator thus can be utilized to "drive" the vehicle with no apparent magnitude limits in depth and heading. Further, although the system as modeled has only one integrator per channel, the errors with ramp inputs have still tended to approach zero.

#### 4.8 Chapter Summary

In the present chapter, the LQG/LTR methodology was presented and used with the frequency domain specifications to design a set of filter and control gains for the augmented system's MBC at twenty knots. It was found that a NMP zero outside the compensator's bandwidth did not adversely affect the recovery process.

Using both a linear and nonlinear simulations with step and ramp commands, the MBC was successfully tested against the time domain specifications delineated in Chapter 3. In Chapter 5, the speed range over which the twenty knot MBC meets the specifications shall be investigated and other linear models generated in order to accomplish gain scheduling over the submarine's operational speed range.

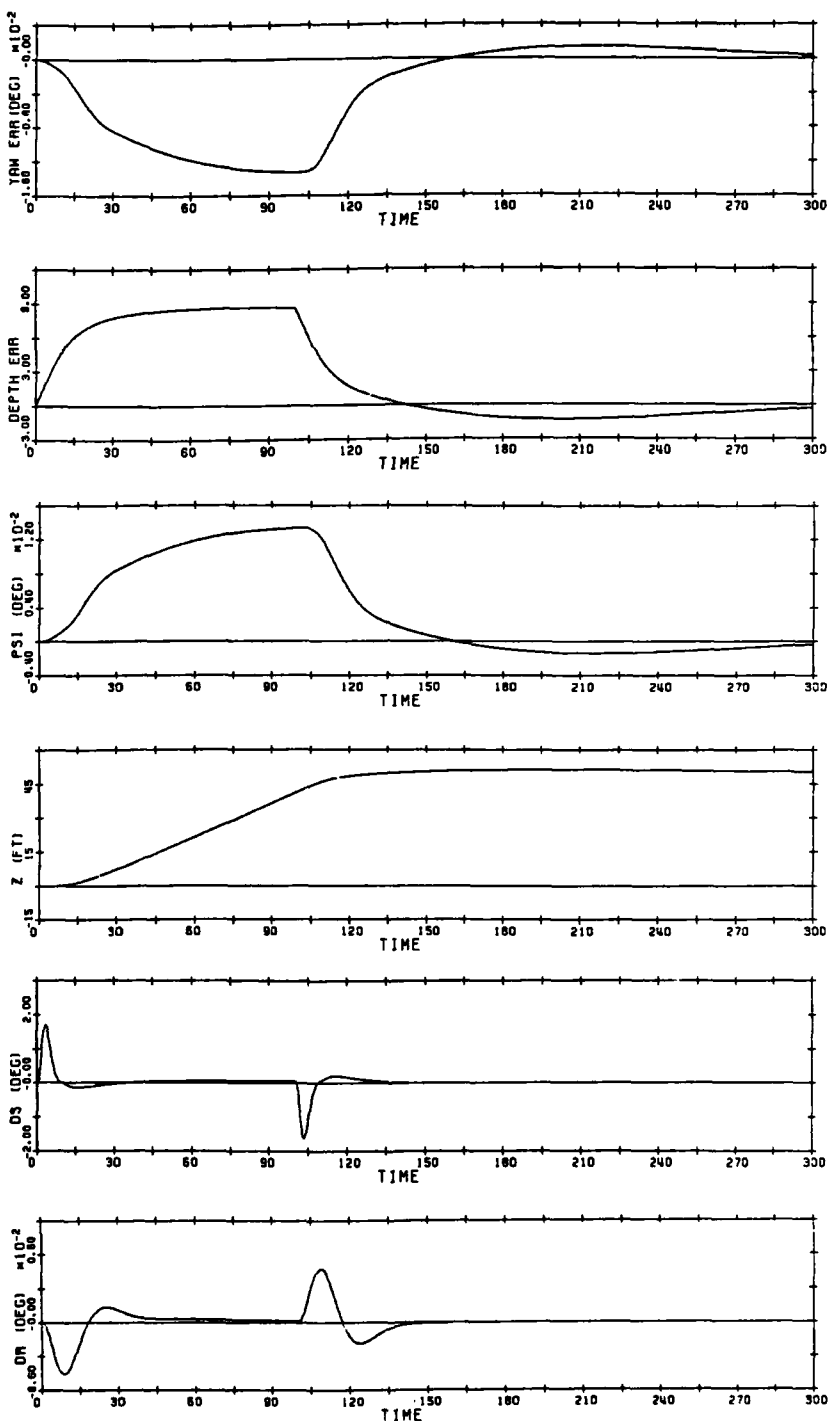


**Figure 4.15: Fifty Foot Ramp Response of the Compensated Nonlinear Model**

## 5. GAIN SCHEDULING

### 5.1 Introduction

In this chapter we shall first investigate the speed range over which the control and filter gains derived from the twenty knot linear model, meet the specifications for the previously discussed ramp and step inputs. In the following sections the five and ten knot models are presented along with their corresponding filter and control gains. The speed range of each set of these compensator gains is also investigated. Finally, a gain scheduling scheme is offered that adequately controls the submarine over the intended five to 30 knot speed range.

### 5.2 Twenty Knot Compensation

#### 5.2.1 Range of the Twenty Knot Controller

Using the nonlinear computer simulation with the propulsion and initial condition data modified as necessary to reflect the desired vehicle speed, one is able to ascertain the speed range over which the twenty knot model-based compensator (MBC) adequately controls the submarine. It was found that the twenty knot control gains, met or bettered specifications over a speed range from 15 knots to 30 knots. The nonlinear time responses at 15 and 30 knots are discussed below.

#### 5.2.2 Vehicle Response at Fifteen Knots Using Twenty Knot Gains

The nonlinear time responses of psi, z, heading error, depth error and control action for simultaneous step inputs of 30 feet and 10 degrees are shown in the plots of Figure 5.1. The time domain specifications are satisfied. The nonlinear model heading error is less than ten percent (one degree) at 80 seconds while the depth error is within 10 percent (three feet) in 149 seconds. The specification at 15 knots is 250 seconds. The error at 250 seconds is 0.54 percent in heading and 0.025 percent in depth which is well within the three

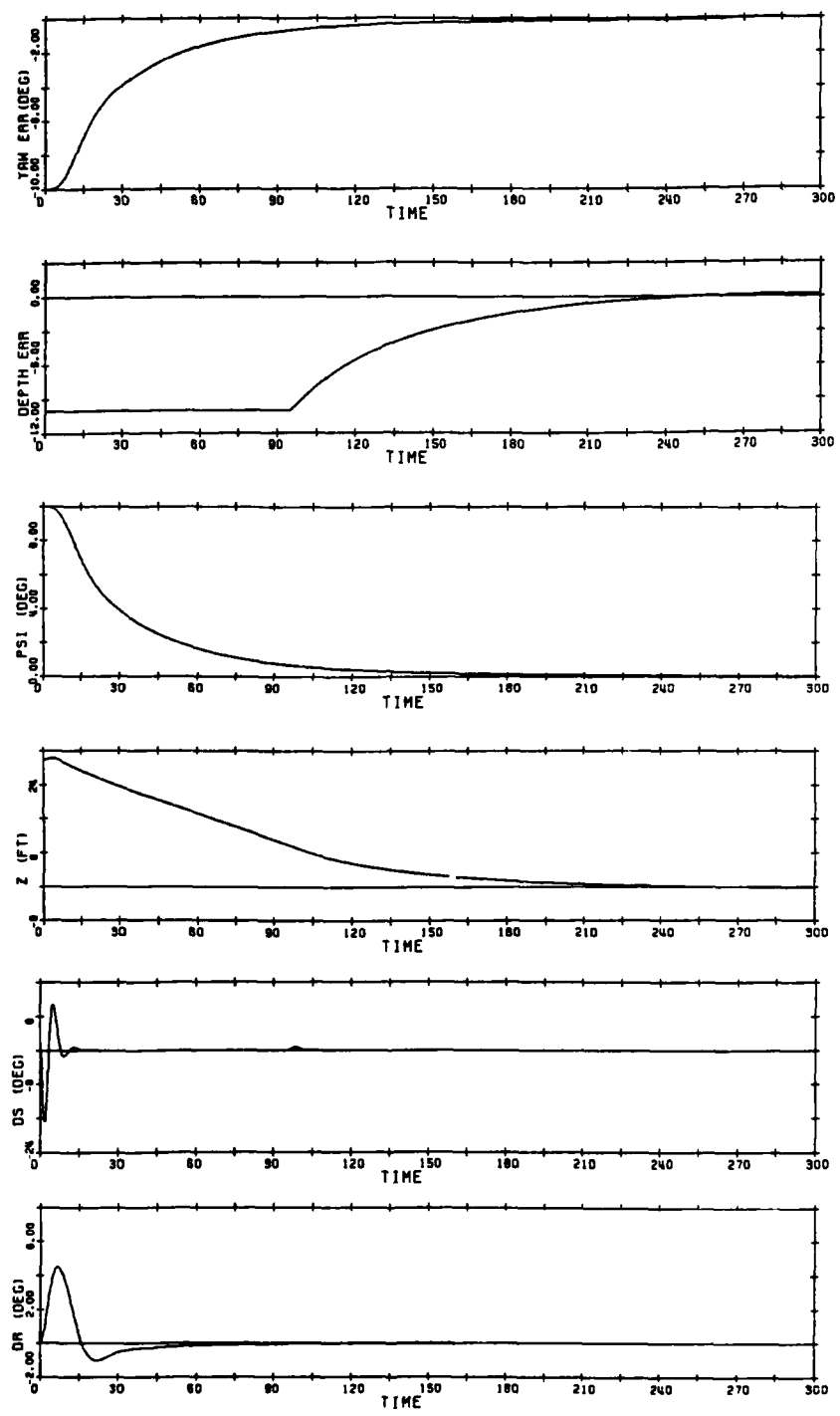


**Figure 5.1: Compensated Nonlinear Step Response  
at 15 Knots with 20 Knot Gains**

percent specification. At 300 seconds (the end of the simulation) the heading error was 0.027 degrees (0.27 percent) with the depth error at 0.17 feet (0.57 percent).

Initial control surface deflections are the same as in the twenty knot case due to the fact that the gains and errors are the same, initially. The maximum rudder angle is 4.5 degrees at seven seconds and the largest sternplane deflection is 16.2 after two seconds. Thus, neither were the rate limits exceeded nor were the control surface deflections near saturation (40 degrees).

Simulations were conducted to ascertain whether the controller could respond adequately to ramp inputs at 15 knots. A 30 degree turn was conducted with the nonlinear model response shown in Figure 5.2. The plots show the submarine reaching 29 degrees 47 seconds after the ramp input ceased (147 seconds simulation time) and still approaching 30 degrees (29.7) at 300 seconds. The maximum depth excursion is 2.93 feet during the turn and is within 0.11 feet (and decreasing) at end of the simulation. Thus, the "level" turn specification (15 feet allowed at 15 knots) was met by the controller.

A depth change of 50 feet at 15 knots was also simulated with excellent results. As before, the simulations show (Figure 5.3) practically no course deviation during the ramp depth change. The nonlinear model response shows the commanded depth being reached in 145 seconds after termination of the ramp input with a 0.3 foot overshoot (0.6 percent). Again, the control design more than adequately meets the specifications.

Thus, the compensator designed for a vehicle linearized about straight ahead motion at twenty knots adequately controls the submersible and easily meets the time domain specifications at 15 knots. In the following section, the results for a vehicle speed of 30 knots are presented.

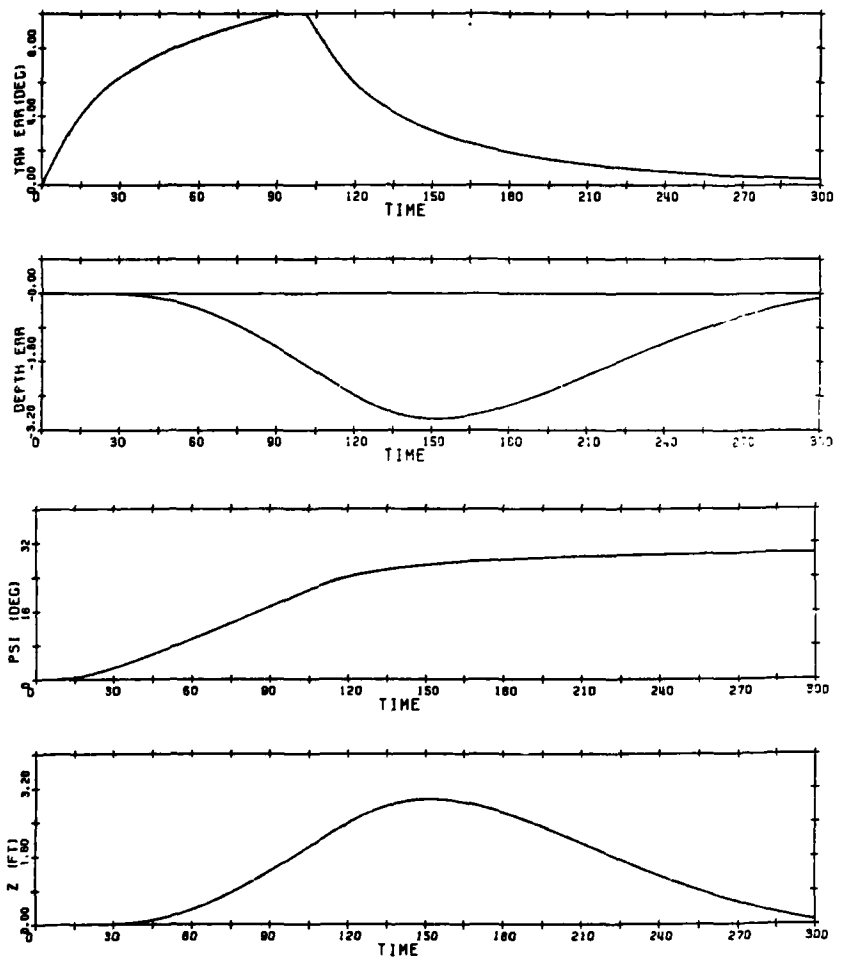


**Figure 5.2: Compensated Nonlinear Response to a 30 Degree Ramp at 15 Knot with 20 Knots Gains**

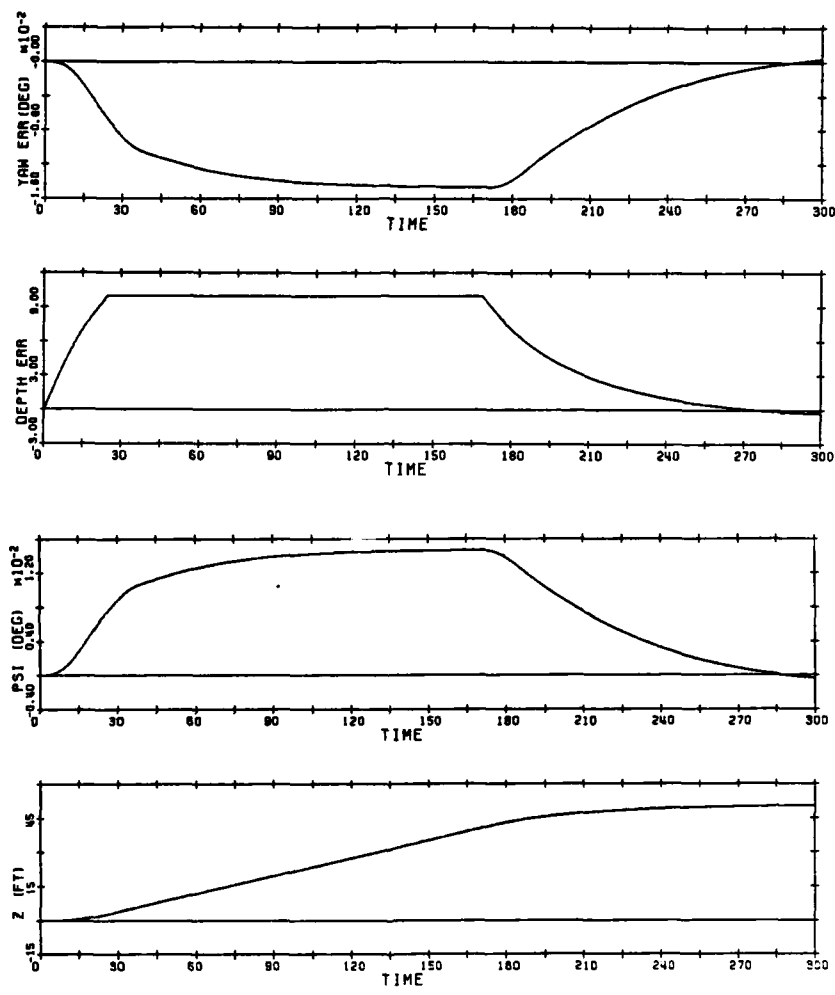


**Figure 5.3: Compensated Nonlinear Response to a 50 Foot Ramp at 15 Knot with 20 Knots Gains**

### **5.2.3 Vehicle Response at Thirty Knots using Twenty Knot Gains**

The nonlinear time response for simultaneous step inputs of 30 feet and 10 degrees is shown in the plots of Figure 5.4. The time domain specification (100 seconds settling time at 30 knots) is satisfied with the nonlinear heading error being less than one degree at 17 seconds and the depth error within 10 percent (three feet) in 46 seconds. At 300 seconds (the end of the simulation) the heading error was 0.093 degrees (0.93 percent) with the depth error at 0.32 feet (1.07 percent). In both cases the error is tending toward zero.

There are small overshoots in both heading and depth responses at 30 knots using 20 knot gains. This is to be expected, since, at higher speeds, the vehicle responds more quickly to a given control surface deflection. The overshoots were 0.66 degrees in yaw and 2.82 feet in depth.

A 30 degree turn was conducted with the nonlinear model responses shown in Figure 5.5. The plots show the submarine reaching 29 degrees 80 seconds after the ramp input ceased with a vehicle heading of 29.8 degrees at 300 seconds. The maximum depth excursion is 4.7 feet during the turn and is within 0.5 feet (and decreasing) at end of the simulation. Thus, the "level" turn specification (20 feet allowed at 30 knots) was met by the controller.

A depth change of 50 feet at 30 knots (see Figure 5.6) was simulated with essentially no course deviation observed during the ramp depth change. The nonlinear model response shows the ordered depth being reached in 21 seconds after termination of the ramp input with a 1.2 foot overshoot (2.4 percent) and an error at 300 seconds of 0.01 percent. Again the control design more than adequately meets the specifications.

Thus, the compensator designed for a vehicle linearized about straight ahead motion at twenty knots adequately controls the submersible at thirty knots. In the following section, the ten knot linear model is briefly discussed along with its control gains and applicable speed range.

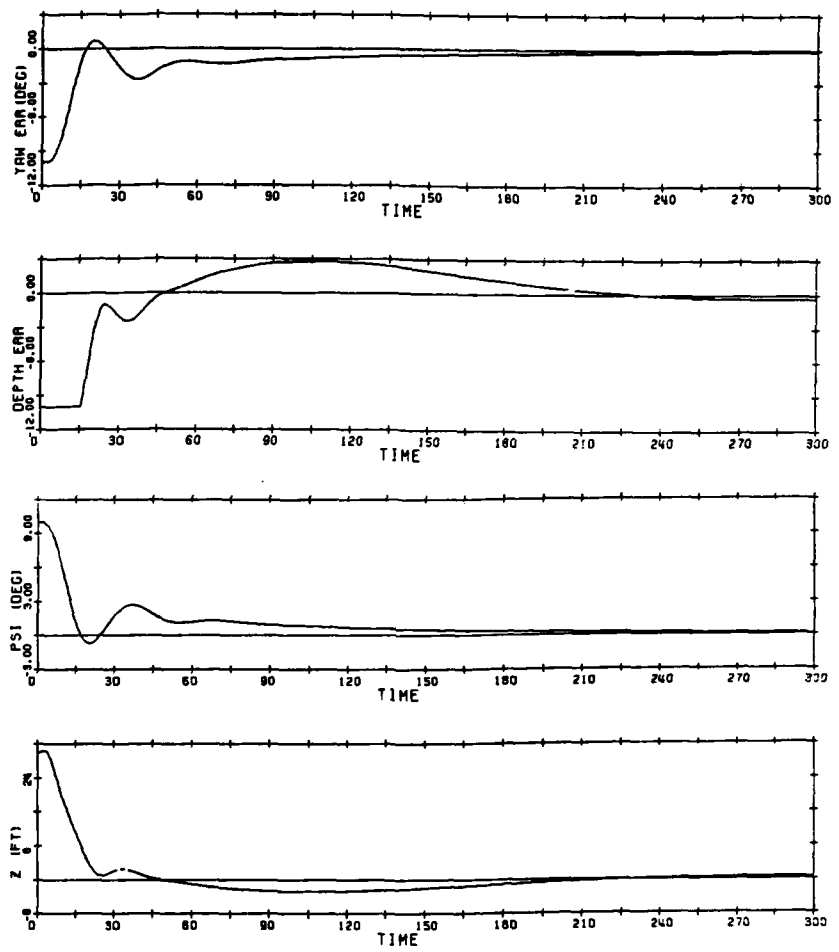


**Figure 5.4: Compensated Nonlinear Step Response  
at 30 Knots with 20 Knot Gains**

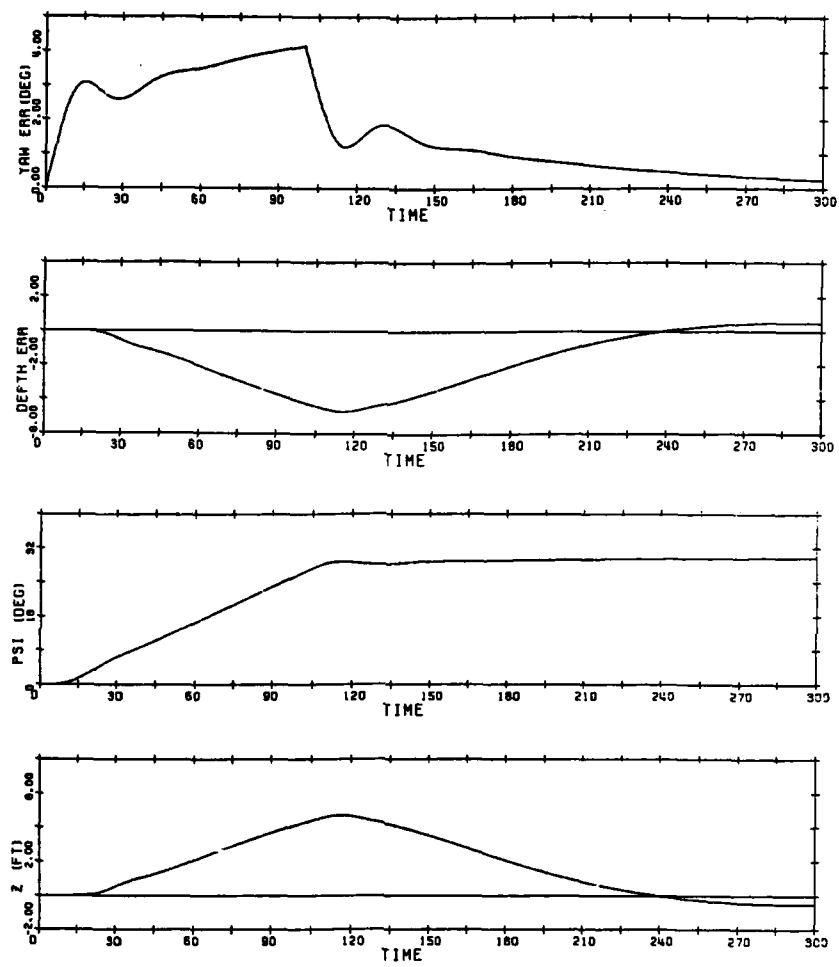


**Figure 5.5: Compensated Nonlinear Response to a 30 Degree Ramp at 30 Knots with 20 Knot Gains**

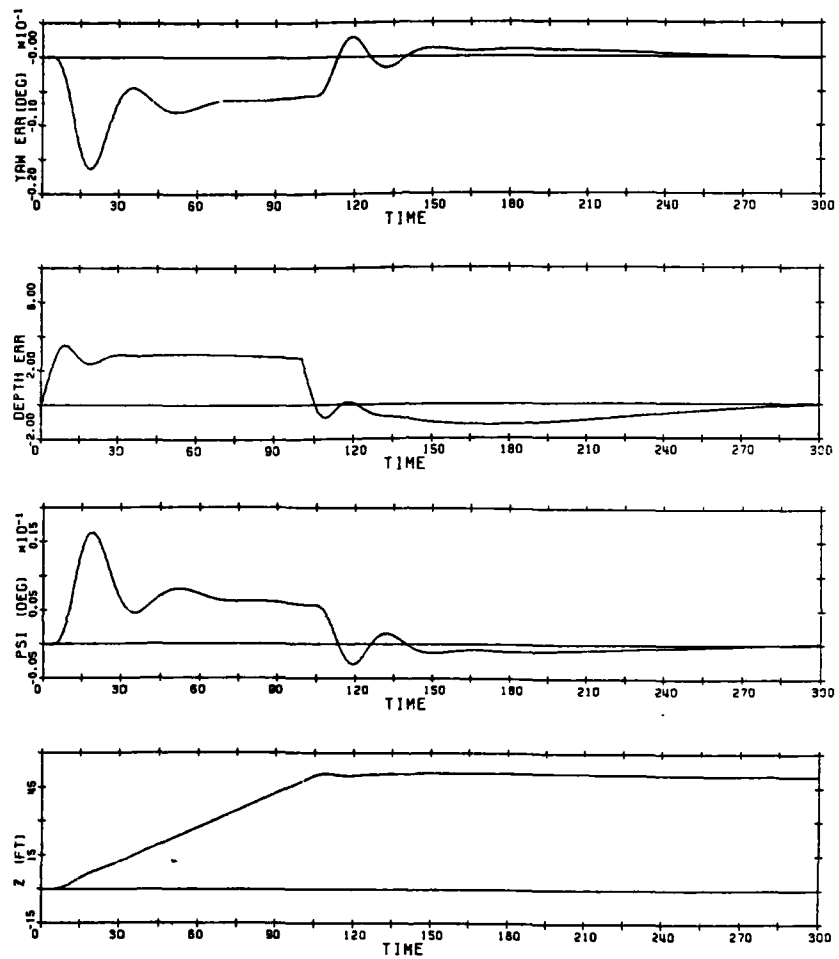


**Figure 5.6:** Compensated Nonlinear Response to a 50 Foot Ramp at 30 Knots with 20 Knot Gains

### 5.3 Ten Knot Linear Model

The nonlinear equations of motion were linearized about straight ahead motion at ten knots with the resultant A and B matrices as shown in Appendix D. The linear model was verified through a modal analysis and a comparison of linear and nonlinear responses to comparable perturbations. The open-loop plant contained a NMP zero at +0.241 and two poles at the origin. The open-loop poles and multivariable zeros are also shown in Appendix D. The plant open-loop singular values ( $\sigma_i [\underline{C}(\underline{sI}-\underline{A})^{-1} \underline{B}]$ ) are as plotted in Figure 5.7. The singular value corresponding to depth has a crossover frequency of 0.51 radians per second while the singular value associated with heading angle has a crossover at 0.063 radians per second. The lower crossover frequencies in comparison with the twenty knot model emphasize the fact that as the vehicle slows, so does its speed of response.

This model was also augmented with the break frequency being 0.1 radians per second. This increased the order of the plant to twelve states and added two poles at -0.1. The singular values for this augmented plant cross over at 0.295 (depth) and 0.059 (heading) radians per second. Note the maximum singular value has the NMP zero within its bandwidth.

In designing the controller, the L matrix ( $\underline{L} = .1 \underline{C}'$ ) was selected so that both singular values crossover at 0.1 radians per second. Thus, the NMP zero will be outside the bandwidth of the compensated system.

The LTR methodology was followed ( $1/\sqrt{\mu} = 1$  and  $q = 300$ ) with the singular values of the overall loop transfer matrix, T(s), (which includes the nominal plant, augmentation and model-based compensator) shown in Figure 5.8. Note that both singular values crossover at approximately 0.052 radians per second.

The eigenvalues of the compensator ( $K_{LOG}(s) = \underline{G}(\underline{sI}-\underline{A}+\underline{B}\underline{G}+\underline{H}\underline{C})^{-1}\underline{H}$ ) were calculated and all were found to have negative real parts, as expected. Thus the stability of the Model-Based Compensator was verified. The multivariable phase (PM) and gain margins (GM) of the

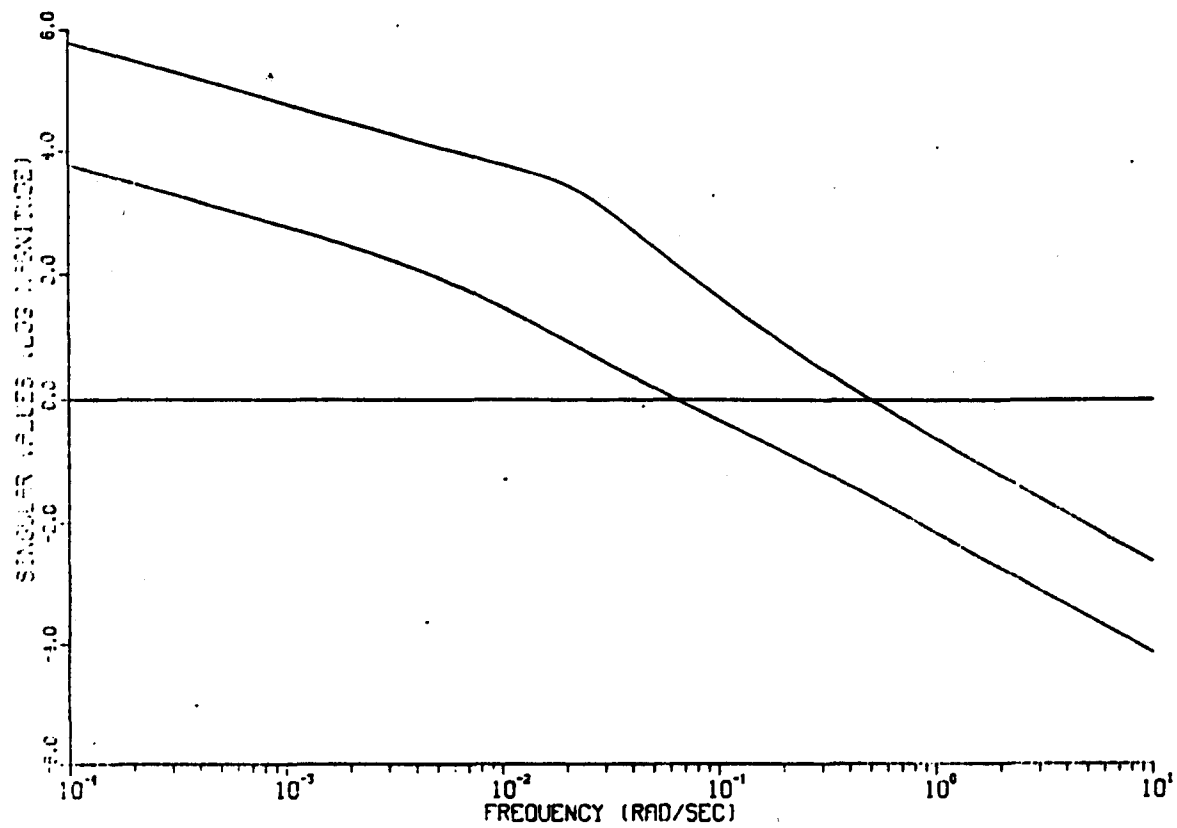


**Figure 5.7: Singular Values of the Ten Knot Open-Loop Plant**

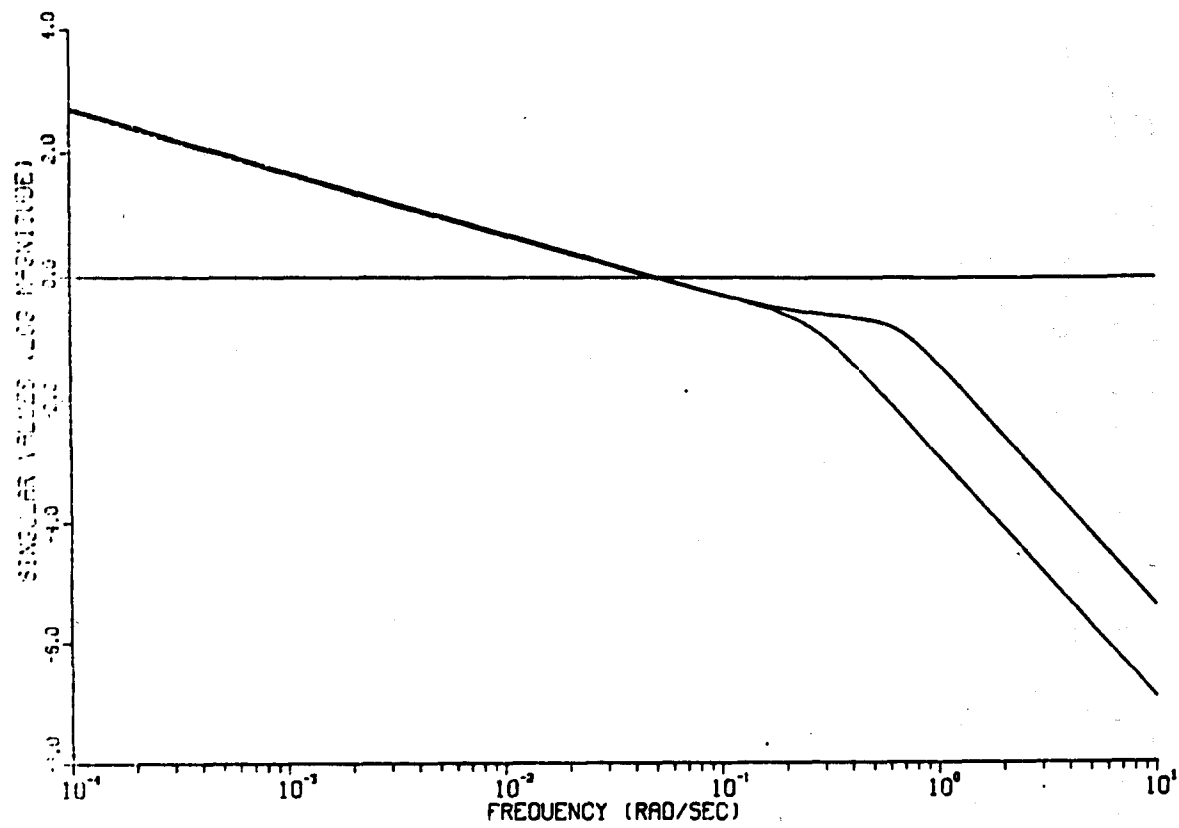


**Figure 5.8: Singular Values of the Compensated Ten Knot System**

compensated system were calculated, and found to be, for additive error:

$$GM = [-4.48 \text{ dB}, 9.75 \text{ dB}]$$

$$PM = [-39.4 \text{ deg}, 39.4 \text{ deg}]$$

for multipliative error:

$$GM = [-\infty, 6 \text{ dB}]$$

$$PM = [-60 \text{ deg}, 60 \text{ deg}].$$

The control and filter gains of the ten knot controller are shown in Appendix D. With these gains, at speeds less than fifteen knots, the error limits imposed within the simulation in order to avoid control surface saturation were four feet and five degrees.

It was found that the ten knot control gains met or bettered specifications over a speed range from 8 knots to 15 knots. Thus, the compensator designed for a vehicle linearized about straight ahead motion at ten knots adequately controls the submersible and meets the time domain specifications from 8 to 15 knots. In the following section, the five knot linear model is discussed.

#### 5.4 Five Knot Linear Model

A linear model was generated at five knots for straight ahead motion and a compensator was designed based on this model. The open-loop plant contained a NMP zero at +0.115. The plant open-loop singular values are as shown in Figure 5.9. The crossovers of the singular values corresponding to psi and depth are 0.032 and 0.26 radians per second respectively. The plant was then augmented with lag compensation at 0.1 radians per second which altered the crossover frequencies to 0.032 and 0.19. The NMP zero is within the system

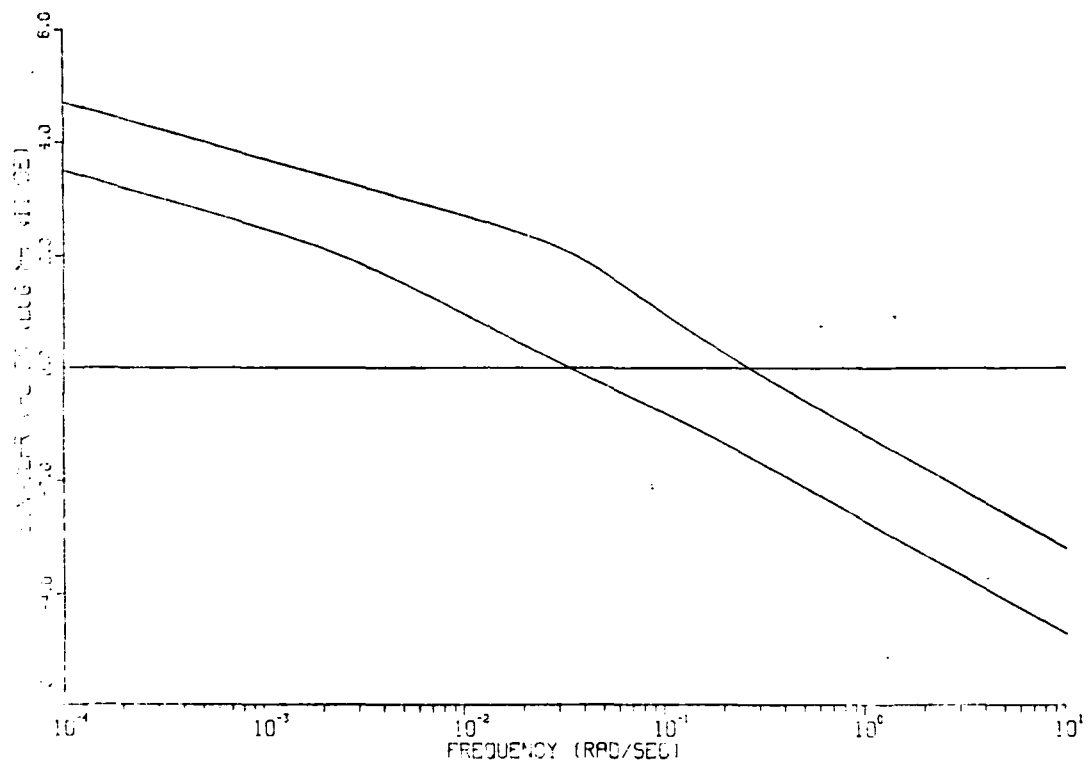


**Figure 5.9: Singular Values of the Five Knot Open-Loop Plant**

bandwidth. Augmentation was considered at lower frequencies (0.05); however, this caused the crossover frequencies to be further reduced in the compensated plant, for gains which did not saturate the controls (low values of the scalar parameter, q).

A compensator was designed to match a crossover frequency of 0.1 radians per second. Designing for a crossover at 0.1 radians per second, instead of around 0.03, was an attempt to increase the bandwidth of the controller (and hence, the speed of response) and to increase the DC gains (reducing the level of steady state error). The singular values of the overall loop transfer matrix,  $\underline{T}(s)$ , for this design ( $1/\sqrt{\mu} = 1$  and  $q = 100$ ) are displayed in Figure 5.10.

Even though the filter transfer function singular values crossover at 0.1 radians per second, in the recovery process the crossover frequencies of the overall transfer matrix attained for reasonable gains (that is gains that did not saturate the controls) are 0.032 radians per second and for psi and 0.036 for depth. Thus, the system's natural bandwidth appears to limit the amount of performance and/or recovery that may reasonably be attained. This was also true in the ten knot design. The end result of designing the filter at a higher crossover frequency (0.1 radians per second) is that the filter poles are slightly faster than necessary as compared to the controller eigenvalues.

The PM and GM for this controller assuming additive error are

$$GM = [-4 \text{ dB}, 7.95 \text{ dB}]$$

$$PM = [-34.9 \text{ deg}, 34.9 \text{ deg}]$$

while for multiplicative error they are

$$GM = [-\infty, 6 \text{ dB}]$$

$$PM = [-60 \text{ deg}, 60 \text{ deg}].$$

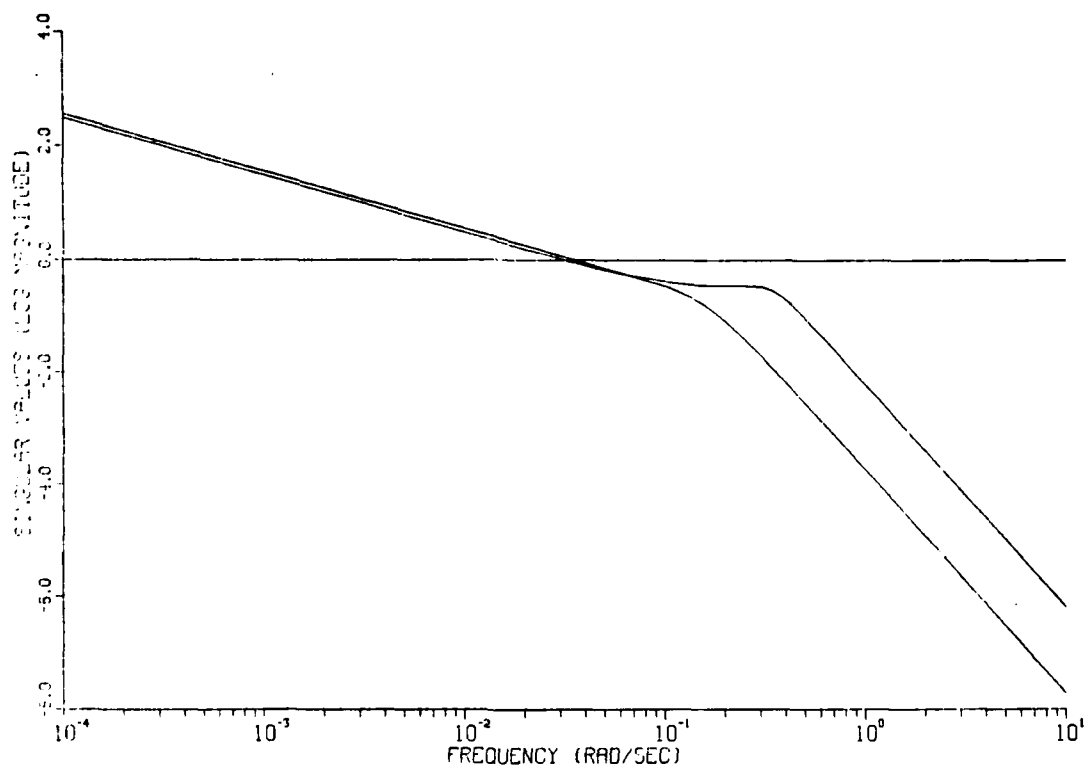


**Figure 5.10: Singular Values of the Compensated Five Knot System**

The five knot linear model (A, B, C), eigenvalues and transmission zeros, and control and filter gains are found in Appendix E.

By using the five knot gains, in the simulation, at various speeds it was shown that the five knot compensator gains met the time domain specifications over the speed range of five to seven knots. In the next section a gain scheduling scheme is discussed and tested.

### 5.5 Gain Scheduling Algorithm

From previous discussions it is clear that for the system under consideration, the LQG/LTR methodology generates robust controllers that are, in general, adequate far from their nominal design points in state space. With just three linear models (at five, ten and twenty knots) it has been shown that, except for the interval from seven to eight knots, the resultant compensator gains adequately control the submersible over its entire speed range. (Between seven and eight knots the response is stable but too slow if the ten knot gains are used and too oscillatory with the five knot compensation).

Unfortunately, using just these three sets of gains and linear models leads to a problem incurred when shifting from one set of gains to another due to the discontinuities at these shift points. This type of gain scheduling would cause large control surface deflections when none are warranted as a gain shift is, in effect, a step perturbation. In order to avoid these discontinuities, it was decided to attempt a linear interpolation scheme between the five and ten knot models; and then, between the ten and twenty knot points. Above twenty knots, the twenty knot model and gains are utilized. For instance, if the commanded submarine speed is seven knots, the control gain (G), filter gain (H) and A matrices (the B and C matrices are the same at all speeds) used in the MBC would be interpolated at two fifths of the difference between the respective matrices at ten and five knots plus, the five knot matrices. It is these interpolated G, H and A matrices that are entered in the simulation.

The simulation has not evolved to the point where gain scheduling can be incorporated on a real-time basis. However, the interpolated matrices for any speed can be generated offline and tested point by point. This was the method used to verify the gain scheduling scheme discussed above.

The linear interpolation algorithm was used to generate MBC's at six, seven, eight, nine, twelve, fifteen and eighteen knots. Results for seven and fifteen knots are discussed below. The error limits for speeds less than fifteen knots were four feet and five degrees while at fifteen knots and above the error limits were 10 feet and 10 degrees.

#### 5.5.1 Selected Gain Scheduling Results

The nonlinear time response at seven knots for simultaneous step inputs of 30 feet and 10 degrees is shown in the plots of Figure 5.11. The time domain specifications are satisfied with the nonlinear model heading error being less than ten percent (one degree) at 100 seconds and the depth error within 10 percent (three feet) in 244 seconds. The specification at seven knots is 360 seconds. At 600 seconds (the end of the simulation) the heading error is 0.096 degrees (0.96 percent) with a depth error of 0.0039 feet (0.013 percent). Both errors are slowly approaching zero.

Control surface deflections are within the specified rate and travel limits. The maximum rudder angle is 7.5 degrees at twelve seconds and the largest sternplane deflection is 24.4 degrees after four seconds.

A 30 degree turn was conducted with the nonlinear model responses shown in Figure 5.12. The plots show the submarine reaching 29 degrees 300 seconds after the ramp input ceased and still approaching 30 degrees (29.6) at 600 seconds. The maximum depth excursion is 0.12 feet during the turn. Thus, the "level" turn specification (10 feet allowed) was met by the controller.

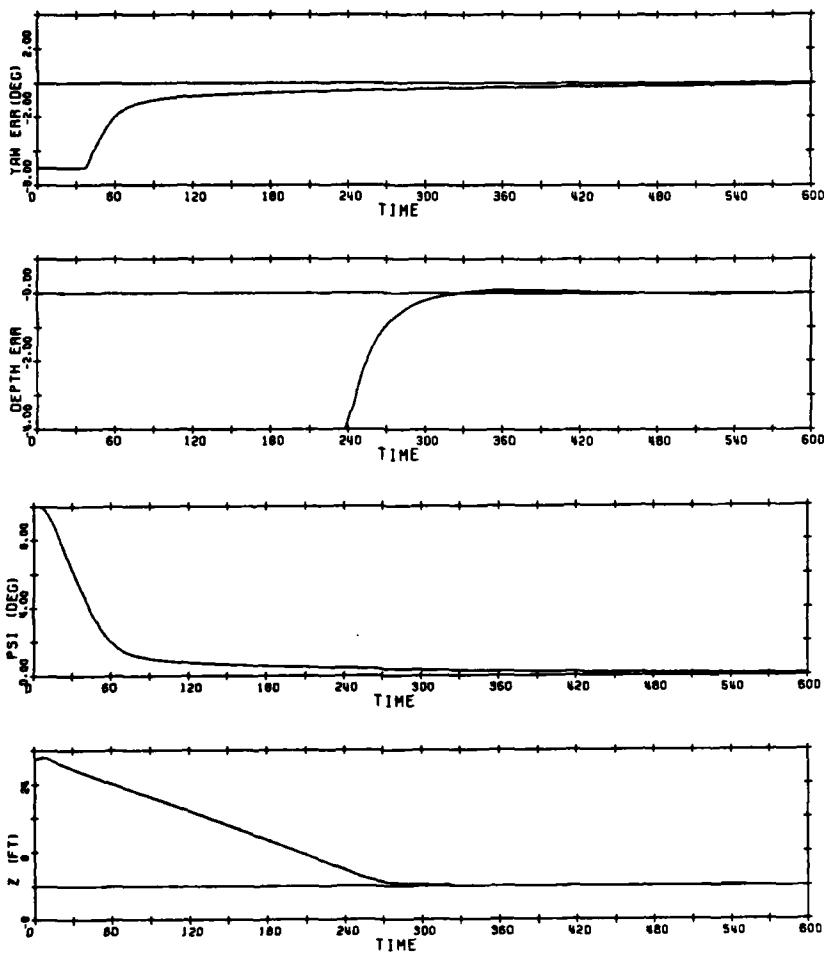


**Figure 5.11: Scheduled Nonlinear Step Response at Seven Knots**

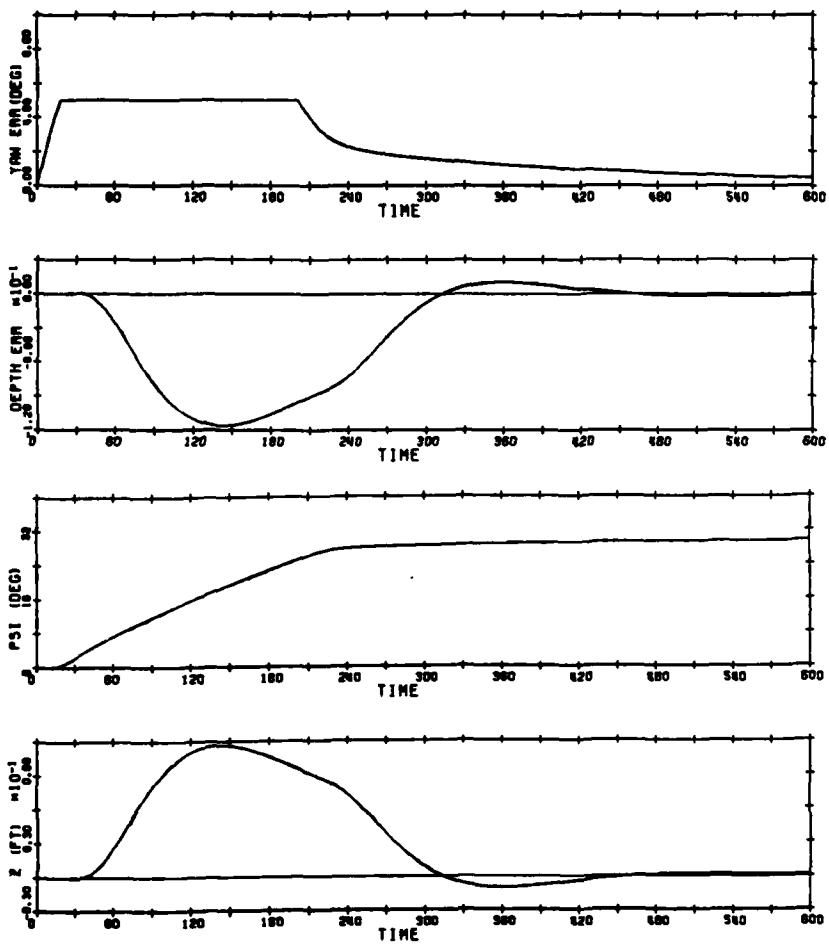


**Figure 3.12: Scheduled Nonlinear 30 Degree Ramp Responses at Seven Knots**

A depth change of 50 feet at seven knots was also simulated as shown in Figure 5.13. The nonlinear model response shows the ordered depth being reached 350 seconds after termination of the ramp input with a 0.13 foot overshoot (0.26 percent). Again the control design more than adequately meets the specification.

Thus, the compensation derived from a linear interpolation between the five and ten knot gains and models adequately controls the submersible and meets the time domain specifications at seven knots. Additionally, the phase and gain margins were calculated. With the interpolated seven knot gains and model, for additive error we have

$$GM = [-4.26 \text{ dB}, 8.69 \text{ dB}]$$

$$PM = [-36.9 \text{ deg}, 36.9 \text{ deg}].$$

For multiplicative error, the multivariable margins are

$$GM = [-\infty, 6 \text{ dB}]$$

$$PM = [-60 \text{ deg}, 60 \text{ deg}].$$

The results for a vehicle speed of 15 knots are now presented.

The time response at fifteen knots for simultaneous step inputs of 30 feet and 10 degrees is shown in the plots of Figure 5.14. The time domain specification (220 seconds settling time) is satisfied with the nonlinear model heading error being less than ten percent (one degree) at 82 seconds while the depth error is within 10 percent (three feet) in 100 seconds. At 400 seconds (the end of the simulation) the heading error was 0.064 degrees (0.64 percent) with the depth error at 0.44 feet (1.46 percent). In both cases the error is tending toward zero.

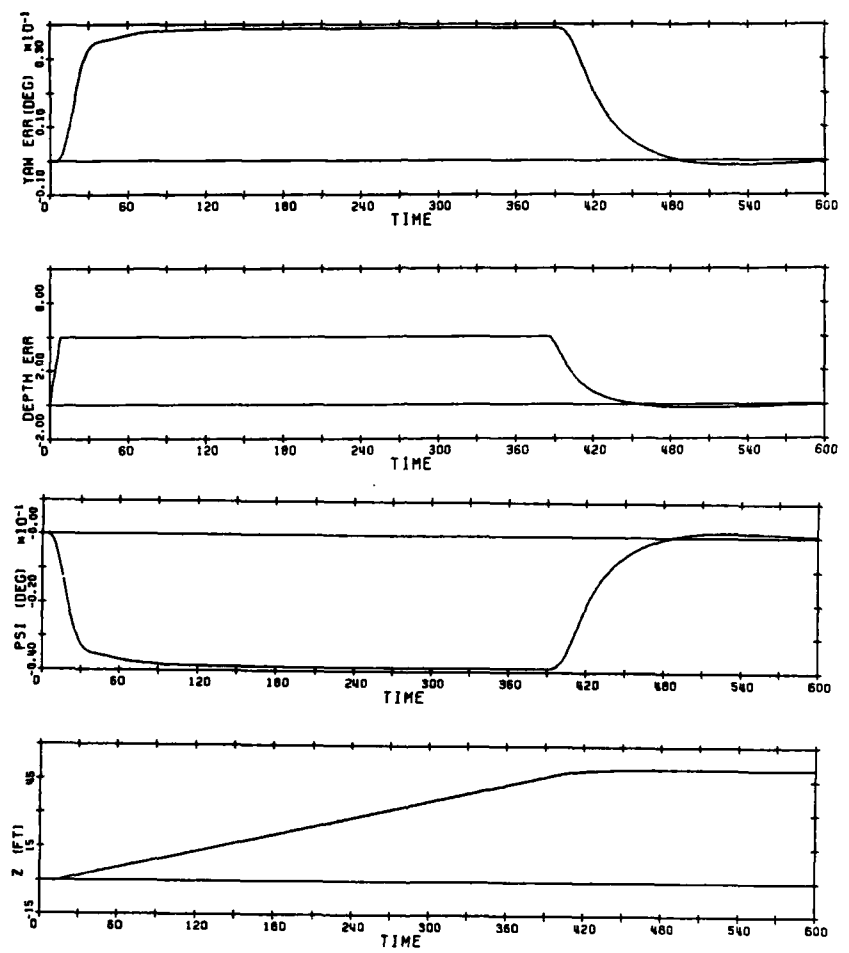


**Figure 5.13: Scheduled Nonlinear 50 Foot Ramp Response at Seven Knots**

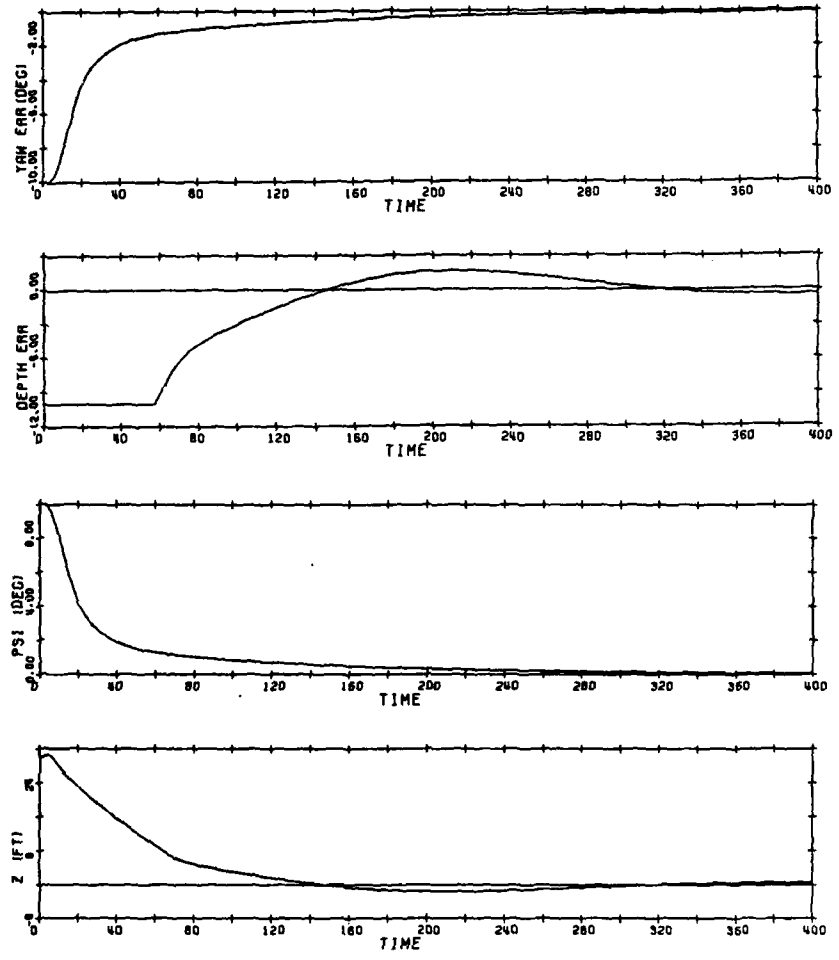


**Figure 5.14: Scheduled Nonlinear Step Responses at Fifteen Knots**

The 30 degree turn was simulated with the nonlinear model responses shown in Figure 5.15. The submarine reaches 29 degrees 160 seconds after the ramp input ceased and the vehicle heading is 29.7 degrees at 400 seconds. The maximum depth excursion is 2.3 feet during the turn and is within 0.13 feet of the reference, and decreasing, at the end of the simulation. The "level" turn specification (15 feet allowed) was met by the controller.

As displayed in Figure 5.16, a depth change of 50 feet at 15 knots was simulated. The nonlinear model response shows the commanded depth being reached 60 seconds after termination of the ramp input with a 2.7 foot overshoot (5.4 percent) and an error at 400 seconds of 1.34 percent (0.67 feet) and declining. Again, the control design more than adequately meets the specifications.

Thus, the 15 knot MBC derived from a linear interpolation between the ten and twenty knot models adequately controls the submersible. The multivariable margins assuming additive error were found to be

$$PM = [-4.64 \text{ dB}, 10.64 \text{ dB}]$$

$$GM = [-41.4 \text{ deg}, 41.4 \text{ deg}].$$

For multiplicative errors the margins are

$$PM \approx [-\infty, 6 \text{ dB}]$$

$$GM = [-60 \text{ deg}, 60 \text{ deg}].$$

Further, the interpolated gains were found to meet or better the specifications at all speeds tested.

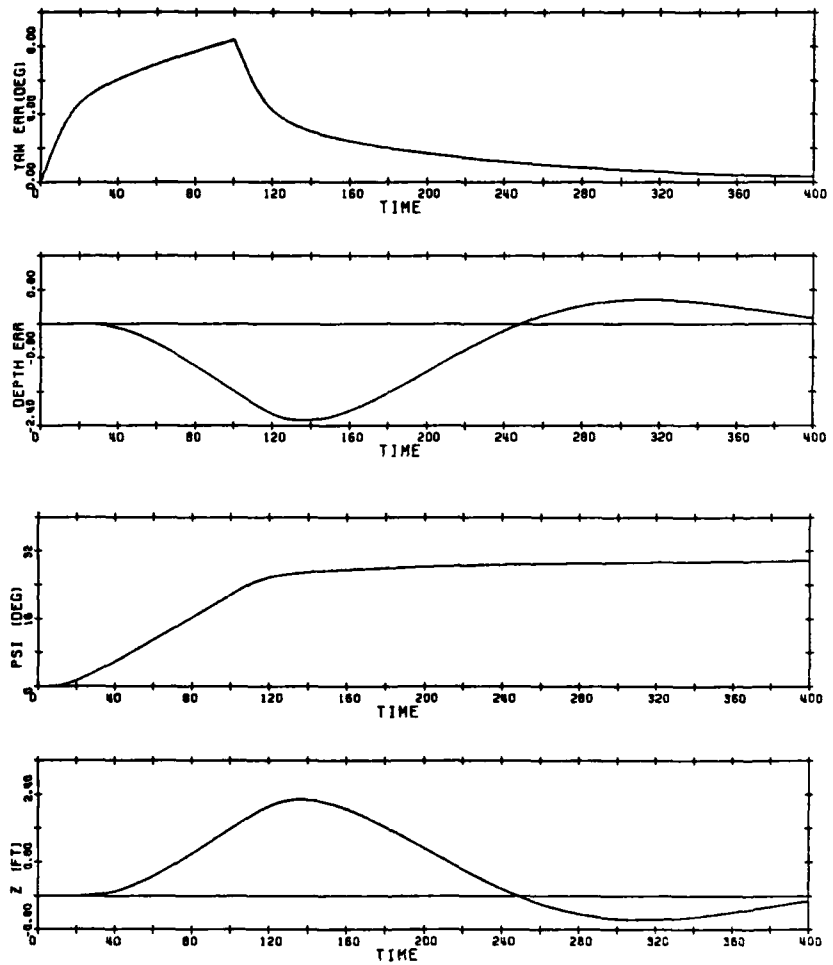


**Figure 5.15: Scheduled Nonlinear 30 Degree Ramp Response at Fifteen Knots**

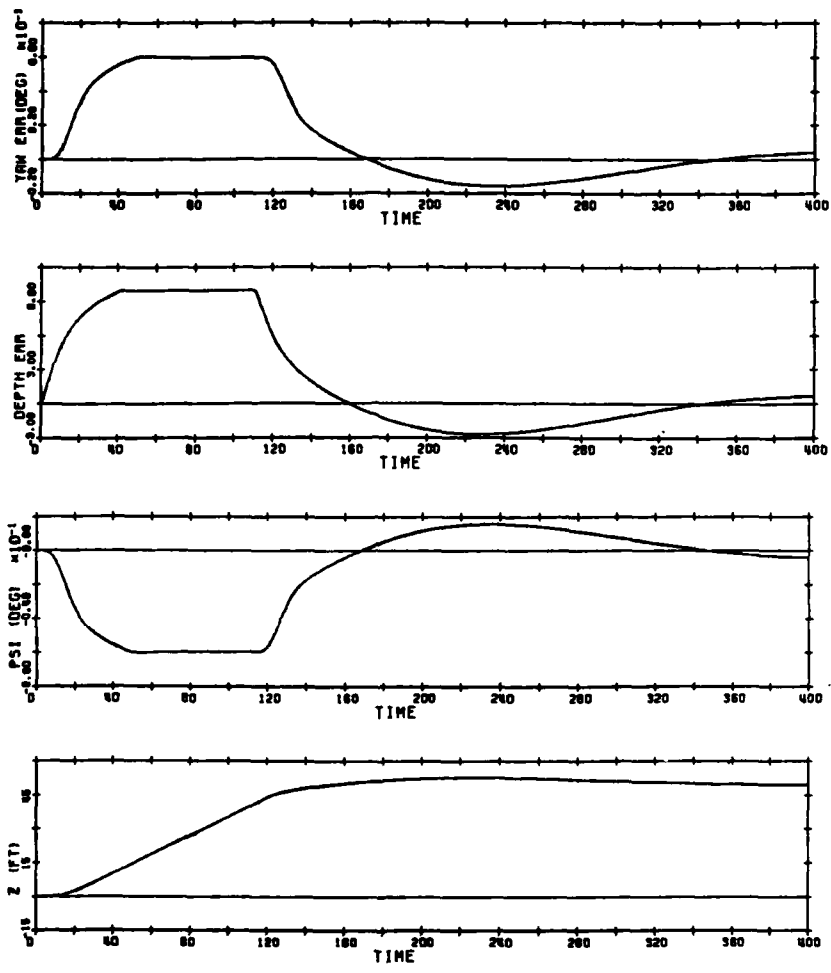


**Figure 5.16: Scheduled Nonlinear 50 Foot Ramp Response at Fifteen Knots**

### 5.6 Chapter Summary

It has been shown that a linear interpolation, gain scheduling scheme provides satisfactory control of the submerged vehicle from five to twenty knots. At twenty knots and above, the twenty knot MBC yields excellent results. Thus, the three linear models and their associated compensations have adequately served as the basis for control of the vehicle over its operating range in speed. Also, we remark here that faster, as well as larger, ramp inputs can be tolerated making the controllers presented here even more practical.

## 6. SUMMARY, CONCLUSIONS AND RECOMMENDATIONS

### 6.1 Summary

This thesis presented a multivariable control design example for an underwater vehicle which comprised of the following:

1. Vehicle modeling based on the NSRDC 2510 equations including crossflow drag and vortex shedding terms. These equations were linearized to generate the linear model of the submarine which was then analyzed and verified.
2. Frequency and time domain specifications were then developed against which a controller could be designed and tested. Multivariable robustness issues were also discussed.
3. The Model-Based Compensator structure was presented and appropriate loop shaping (lag augmentation) included in the compensator structure. The Linear Quadratic Gaussian/Loop Transfer Recover (LQG/LTR) methodology for multivariable control design was discussed and an example of the frequency domain based design process was given for the vehicle model at twenty knots. The controller robustness in terms of multivariable phase and gain margins was evaluated and, using a nonlinear simulation, the compensator was tested. The compensator was subjected to step and ramp inputs and its response evaluated using the time domain specifications.
4. The speed range over which the twenty knot model and control gains met the performance specifications was then investigated. Linear models at five and ten knots were discussed and used as a basis for generating two additional sets of compensator gains. Using the three linear models and their respective control gains a gain scheduling scheme was presented and tested which allowed for good automatic heading and depth control of the submersible over its operational speed range.

### **6.2 Conclusions**

For the type of control design desired, namely, an automatic heading and depth control, linearizing about straight ahead motion at constant speed incorporated enough of the essential vehicle dynamics so as to yield a model which was adequate for compensator design. The LQG/LTR design methodology offered a systematic method for multivariable control design which generated robust controllers that were not only stable but provided satisfactory control far from their nominal point in state space. Further, the method allowed recovery of the desired singular value loop shapes in the presence of NMP zeros which were outside the bandwidth of the compensator. However, the maximum bandwidth of the compensated system appears to be constrained by the plant's natural open-loop bandwidth. This is an advantageous property of the LTR process as it disallows compensator designs that mathematically enhance the system bandwidth but prove useless in practice.

### **6.3 Recommendations for Further Study**

Incorporating differential control on the sternplanes (or using a different control surface configuration such as the inverted-Y) should be investigated. A control system of three inputs (rudder, and differential sternplanes) and three outputs (heading, depth and roll) could be designed which would reduce the coupling effects between planes of motion by allowing direct control over the vehicle roll orientation. This would assist in further overcoming the strong tendency of the vehicle to dive while turning.

As the controller design and model requirements are strongly dependent upon the function a control system is expected to serve, one could linearize the equations of motion about small control surface deflections in order to more fully capture the true vehicle dynamics in the linear model. This might, however, require more models and a more complex gain scheduling technique to adequately control the vehicle over its speed range.

Incorporating free surface effects (wave action) in the simulation would provide a more realistic model of the environment near the ocean surface. This, in the addition to gain scheduling within the simulation, would enable one to test the control design more completely in determining its practicality.

The type of control surface action which the LQG/LTR methodology produced is an interesting area for a designer's consideration. The vast majority of control movement is developed in the first ten to thirty seconds; and thus, yields large, rapid deflections. This large, rapid control action associated with the present design is due to the quadratic cost functional used in the linear quadratic control design. Incorporated within the functional is the control weighting matrix R, which penalizes any control action; and thus, by varying the diagonal entries of R, slower, less severe control action may be generated, if desired.

Finally, it would be advantageous to develop an estimate of the modeling errors. This would allow a more revealing and realistic measure of robustness than the multivariable phase and gain margins used in this thesis. The need for modifying the controllers may be identified, based on the modeling error information and the robustness criterion presented in Chapter 3.

## APPENDIX A

### NONLINEAR EQUATIONS OF MOTION

#### 1. SURGE

$$\begin{aligned} m[\dot{u} + qw - rv - x_G(q^2 + r^2) + y_G(pq - \dot{r}) + z_G(pr + \dot{q})] &= \\ \frac{\rho}{2} \ell^4 [x_{qq}q^2 + x_{rr}r^2 + x_{rp}rp] &+ \\ + \frac{\rho}{2} \ell^3 [x_u \dot{u} + x_{vr}vr + x_{wq}wq] &+ \frac{\rho}{2} \ell^2 [x_{uu}u^2 + x_{vv}v^2 + x_{ww}w^2] + \\ + \frac{\rho}{2} \ell^2 u^2 [x_{\delta r \delta r} \delta r^2 + x_{\delta s \delta s} \delta s^2 + x_{\delta b \delta b} \delta b^2] &+ (\text{PROPTH} - \text{DRAG}) \\ + \frac{\rho}{2} \ell^2(n-1) [x_{vv\eta}v^2 + x_{ww\eta}w^2 + x_{\delta r \delta r \eta}u^2 \eta \delta r^2 + x_{\delta s \delta s \eta}u^2 \delta s^2] & \\ - WTOT \sin \theta & \\ \text{PROPTH} - \text{DRAG} &= u^2(c_i n^2 + b_i n + a_i) \end{aligned}$$

2. SWAY

$$\begin{aligned}
 m[\dot{v} - pw + ur - y_G(r^2 + p^2) + z_G(qr - \dot{p}) + x_G(qp + \dot{r})] &= \\
 \frac{\rho}{2} \ell^4 [y_r \dot{r} + y_p \dot{p} + y_p |p| p |p| + y_{pq} pq + y_{qr} qr + y_{rv} \text{sign}(r, v) \sqrt{v^2 + w^2}] \\
 + \frac{\rho}{2} \ell^3 [y_{wp} wp + y_r ur + y_p up + y_{|r|} \delta r u |r| \delta r] &+ \\
 + \frac{\rho}{2} \ell^2 [y_x u^2 + y_v uv + y_{|v|} v w \sqrt{v^2 + w^2}] &+ y_{\delta r} u^2 \delta r + \\
 + y_{vw} vw u / \sqrt{u^2 + v^2 + w^2} &+ WTOT \sin \phi \cos \theta + \\
 + (n-1) \left\{ \frac{\rho}{2} \ell^3 y_{rn} ur + \frac{\rho}{2} \ell^2 y_{vn} uv + \frac{\rho}{2} \ell^2 y_{\delta rn} u^2 \delta r + \right. \\
 \left. + \frac{\rho}{2} \ell^2 y_v |r| n v \sqrt{v^2 + w^2} \right\} + y_{CRFL} + y_{VTX}^*
 \end{aligned}$$

$$y_{CRFL}: \left\{ \frac{\rho}{2} \left( -\ell^2 \frac{z_{ww}}{\int_{\ell} D(x) dx} \right) \right\} \int_{\ell} H(x) v(x) \sqrt{v^2(x) + w^2(x)} dx$$

$$y_{VTX}^*: \left\{ \frac{\rho}{2} \ell^2 \frac{z_{vv}}{(\bar{x}_{fw} - x_{so})} \right\} \int_{x_{vs}}^{x_{fw}} w(x) \bar{v}_{fw} (t - \tau_x) dx ; \text{ not included in IBM program.}$$

$$\text{sign}(r, v) \triangleq r \cdot \frac{v}{|v|}$$

$\tau_x$ : time it took vehicle to travel a distance  $x$  in the axial direction

3. HEAVE

$$\begin{aligned}
 m[\dot{w} + vp - uq - z_G(p^2 + q^2) + x_G(rp - \dot{q}) + y_G(rp + \dot{p})] = \\
 \frac{\rho}{2} \ell^4 [z_q \dot{q} + (z_{rr} r^2 + z_{rp} rp) \frac{u}{\sqrt{u^2 + v^2 + w^2}}] + \\
 + \frac{\rho}{2} \ell^3 [z_w \dot{w} + z_{vr} vr \frac{u}{\sqrt{u^2 + v^2 + w^2}} + z_w |q| \frac{w}{|w|} \sqrt{v^2 + w^2} |q| + \\
 + z_q uq + z|q| u|q|\delta s] + \\
 + \frac{\rho}{2} \ell^2 [z_{vp} \frac{u}{\sqrt{u^2 + v^2 + w^2}} vp + z_* u^2 + z_{vv} \frac{v^2 u}{\sqrt{u^2 + v^2 + w^2}} + \\
 + z_w |w| \sqrt{v^2 + w^2} w + z_w uw + z_{\delta s} u^2 \delta s + z_{\delta b} u^2 \delta b + z|w| u|w| + \\
 + z_{ww} |w| \sqrt{v^2 + w^2}] + WTOT \cos \phi \cos \theta + \\
 + (\eta - 1) \left\{ \frac{\rho}{2} \ell^3 z_{qn} uq + \frac{\rho}{2} \ell^2 z_{w\eta} uw + \frac{\rho}{2} \ell^2 z_w |w| \eta w \sqrt{v^2 + w^2} + \right. \\
 \left. + \frac{\rho}{2} \ell^2 z_{\delta s\eta} u^2 \delta s \right\} + z_{CRFL} + z_{VTX}^*
 \end{aligned}$$

$$z_{CRFL} = -\frac{\rho}{2} \int_l^{\infty} C_d D(x) w(x) \sqrt{v^2(x) + w^2(x)} dx$$

$$z_{VTX}^* = \frac{\rho}{2} \ell C_y \int_{x_{vs}}^{x_{fw}} v(x) v_{fw}(t - \tau_x) dx ; \text{ not included in the IBM program.}$$

4. ROLLING TORQUE ( $\phi$ )

$$\begin{aligned}
 & I_x \dot{p} + (I_z - I_y)qr - (\dot{r} + pq)I_{xz} + (r^2 - q^2)I_{yz} + (pr - \dot{q})I_{xy} + \\
 & m(y_G(\dot{w} - uq + vp) - z_G(\dot{v} - wp + ur)) = \\
 & \frac{\rho}{2} \ell^5 [K_p \dot{p} + K_r \dot{r} + K_p |p| p' p + K_{qr} qr + K_{pq} pq] + \\
 & + \frac{\rho}{2} \ell^4 [K_v \dot{v} + K_r ur + K_p up] + \\
 & + \frac{\rho}{2} \ell^3 [K_u u^2 + K_v uv + K_v |v| \sqrt{v^2 + w^2} + K_{\delta r} u^2 \delta r + K_{vw} vw + \\
 & + (n-1) K_{\eta} u^2] \\
 & - (z_G^{WTOT} - z_B^B) \cos \theta \sin \phi + (y_G^{WTOT} - y_B^B) \cos \theta \cos \phi + \\
 & + [u^2 + v_t^2 + w_t^2] [k_{4t} \beta_t^2 \sin 4\phi_t + k_{8t} \beta_t^2 \sin 8\phi_t] + \\
 & + \frac{\rho}{2} \ell C_v \bar{x}_{fw} \int_{x_{vs}}^{\bar{x}_f} w(x) \bar{v}_w(t - \tau_x) dx
 \end{aligned}$$

$$v_t = v + x_t r$$

$$w_t = w - x_t q$$

$$\phi_t = \tan^{-1} \left( -\frac{w_t}{v_t} \right)$$

$$\beta_t = \tan^{-1} \sqrt{v_t^2 + w_t^2} / u$$

5. PITCHING TORQUE ( $\theta$ )

$$\begin{aligned}
 I_y \dot{q} + (I_x - I_z)rp - (\dot{p} + qr)I_{xy} + (p^2 - r^2)I_{zx} + (qp - \dot{r})I_{yz} &+ \\
 + m[z_G(\dot{u} - vr + wr) - x_G(\dot{w} - uq + vp)] &= \\
 = \frac{\rho}{2} l^5 [M_q \dot{q} + M_{xr} r^2 \frac{u}{\sqrt{u^2 + v^2 + w^2}}] &+ \\
 + \frac{\rho}{2} l^4 [M_w \dot{w} + M|w|q \frac{q/\sqrt{v^2 + w^2}}{u} + M_q uq + M|q|\delta s u|q|\delta s] &+ \\
 + \frac{\rho}{2} l^3 [M_u u^2 + M_{\delta s} v^2 \frac{u}{\sqrt{u^2 + v^2 + w^2}} + M_w|w| \frac{w/\sqrt{v^2 + w^2}}{u} + M|w|u|w|] &+ \\
 + M_{\delta s} u^2 \delta s + M_{\delta b} u^2 \delta b + M|w| u|w| + M_w|w| |w| \frac{\sqrt{v^2 + w^2}}{u} & \\
 - (z_G^{WTOT} - z_B^B) \sin \theta - (x_G^{WTOT} - x_B^B) \cos \theta \sin \phi & \\
 + (n-1) [\frac{\rho}{2} l^4 M_{qn} uq + \frac{\rho}{2} l^3 M_{wn} uw + \frac{\rho}{2} l^3 M_w|w| n \frac{w/\sqrt{v^2 + w^2}}{u} + M_{\delta sn} u^2 \delta s] & \\
 + M_{CRFL}^* + M_{VTX}^* &
 \end{aligned}$$

$$M_{CRFL} = \frac{\rho}{2} \int_l C_d \times D(x) w(x) \sqrt{v^2(x) + w^2(x)} dx$$

$$M_{VTX}^* = -\frac{\rho}{2} l C_v \int_{x_{vs}}^{x_{fw}} x v(x) \bar{v} f_w(t - \tau_x) dx ; \text{ not included in IBM.}$$

6. YAWING TORQUE ( $\psi$ )

$$\begin{aligned}
 I_z \dot{r} + (I_y - I_x)pq - (\dot{q} + rp)I_{yz} + (q^2 - p^2)I_{xy} + (rp - \dot{p})I_{zx} + \\
 + m[x_G(\dot{v} - wp + ur) - y_G(\dot{u} - vr + wq)] = \\
 + \frac{\rho}{2} l^5 [N_r \dot{r} + N_p \dot{p} + N_{qr} qr + Nr |r| r |r| + N_{pq} pq] + \\
 + \frac{\rho}{2} l^4 [N_v |r| r \sqrt{v^2 + w^2} + N_{wp} wp + N_r ur + N_p up + N_v \dot{v} + N_r |\delta r| u |r| \delta r] + \\
 + \frac{\rho}{2} l^3 [N_u u^2 + N_v |v| v \sqrt{v^2 + w^2} + N_v uv + N_{vw} \frac{vwu}{\sqrt{u^2 + v^2 + w^2}}] + \\
 + (n-1) [\frac{\rho}{2} l^4 N_{r\eta} ur + \frac{\rho}{2} l^3 N_{v\eta} uv + \frac{\rho}{2} l^3 N_v |v| \eta v \sqrt{v^2 + w^2} + \\
 + \frac{\rho}{2} l^3 N_{\delta r\eta} u^2 \delta r] \\
 + (x_G^{WTOT} - x_B^B) \cos \theta \sin \phi + (y_G^{WTOT} - y_B^B) \sin \theta + N_{CRFL}^* + W_{VTX}^*
 \end{aligned}$$

$$N_{CRFL} = -\frac{\rho}{2} C_{dy} \int_l^\infty x H(x) v(x) \sqrt{v^2(x) + w^2(x)} dx$$

$$N_{VTX}^* = -\frac{\rho}{2} l C_v \overline{x}_{fw} \int_{x_{vs}}^\infty x w(x) \bar{v} f_w(t - \tau_x) dx ; \text{ not included in IBM}$$

KINEMATIC RELATIONS

$$u^2 = u^2 + v^2 + w^2$$

$$\dot{z}_o = -u \sin \theta + v \cos \theta \sin \phi + w \cos \theta \cos \phi$$

$$\dot{\phi} = p + \dot{\psi} \sin \theta$$

$$\dot{\theta} = \frac{q - \dot{\psi} \cos \theta \sin \phi}{\cos \phi}$$

$$\dot{\psi} = \frac{r + \theta \sin \phi}{\cos \theta \cos \phi}$$

## APPENDIX B

### PARAMETRIC LINEARIZATION

#### I. AXIAL FORCE (SURGE)

$$\begin{aligned}
 & [m - x_{\dot{u}}] \Delta \dot{u} - my_G \Delta \dot{r} + mz_G \Delta \dot{q} = \\
 & = \Delta u [2u_o \{x_{uu} + a_i + b_i \eta + c_i \eta^2 + x_{\delta r \delta r} \delta r^2 + x_{\delta s \delta s} \delta s^2 + \\
 & + x_{\delta b \delta b} \delta b^2 + (\eta_o - 1) (x_{\delta r \delta r \eta} \delta r^2 + x_{\delta s \delta s \eta} \delta s^2)\}] + \\
 & + \Delta v [2(x_{vv} + (\eta_o - 1)x_{vvn}) v_o + (x_{vr} + m)r_o] + \\
 & + \Delta w [2(x_{ww} + (\eta_o - 1)x_{wwn}) w_o + (x_{wq} - m)q_o] + \\
 & + \Delta p [-my_G q_o - (mz_G - x_{rp}) r_o] + \\
 & + \Delta q [(x_{wq} - m)w_o - my_G p_o + 2(mx_G + x_{qq})q_o] + \\
 & + \Delta r [(x_{vr} + m)v_o + (x_{rp} - mz_G)p_o + 2(mx_G + x_{rr})r_o] \\
 & - \Delta \theta [(WTOT - B) \cos \theta_o] \\
 & + \Delta \delta s [2(x_{\delta s \delta s} + x_{\delta s \delta s \eta} (\eta_o - 1)) \delta s_o u_o^2] \\
 & + \Delta \delta b [2x_{\delta b \delta b} u_o^2 \delta b_o] \\
 & + \Delta \delta r [2(x_{\delta r \delta r} + x_{\delta r \delta r \eta} (\eta_o - 1)) \delta r_o u_o^2] \\
 & + \Delta \eta [u_o^2 (b_i + 2c_i \eta_o) + x_{vvn} v_o^2 + x_{wwn} w_o^2 \\
 & + (x_{\delta s \delta s \eta} \delta s_o^2 + x_{\delta r \delta r} \delta r_o^2) u_o^2]
 \end{aligned}$$

### III. LATERAL FORCE

$$\begin{aligned}
 & [m - Y_v] \Delta \dot{v} - (mz_G + Y_p) \Delta \dot{p} + (mx_G - Y_r) \Delta \dot{r} = \\
 & \Delta u [2u_o \{Y_* + Y_{\delta r} \delta r + (\eta_o - 1) Y_{\delta r \eta} \delta r - \frac{1}{2} \frac{Y_{vw} u_o v_o w_o}{(u_o^2 + v_o^2 + w_o^2)^{3/2}}\} + \\
 & + v_o \{Y_v + (\eta_o - 1) Y_{vn} + \frac{Y_{vw} w_o}{\sqrt{u_o^2 + v_o^2 + w_o^2}}\} + Y_p p_o + \\
 & + r_o \{(Y_r - m) + Y|_r| \delta r \frac{|r_o|}{r_o} \delta r + (\eta_o - 1) Y_{rn}\}] + \\
 & + \Delta v [u_o \{Y_v + \frac{Y_{vw} w_o}{\sqrt{u_o^2 + v_o^2 + w_o^2}} (1 - \frac{v_o^2}{u_o^2 + v_o^2 + w_o^2}) + (\eta_o - 1) Y_{vn} + \\
 & + v_o \{\frac{Y_v |r| |r_o| v_o}{\sqrt{v_o^2 + w_o^2}} + (Y_v |v| + (\eta - 1) Y_v |v| \eta) \cdot (1 + \frac{w_o^2}{v_o^2} + \frac{v_o}{\sqrt{v_o^2 + w_o^2}}) v_o\} \\
 & + Y_{vq} q_o + \frac{\partial Y_{CRFW}}{\partial v} \Big|^\ast] \\
 & + \Delta w [u_o \{ \frac{Y_{vw} v_o}{\sqrt{u_o^2 + v_o^2 + w_o^2}} (1 - \frac{w_o^2}{u_o^2 + v_o^2 + w_o^2})\} + \\
 & + v_o \{ \frac{w_o}{\sqrt{v_o^2 + w_o^2}} (Y_v |r| \frac{|r_o|}{|v_o|} + Y_v |v| + (\eta_o - 1) Y_v |v| \eta)\} \\
 & + p_o \{Y_{wp} + m\} + Y_{wr} r_o + p_o m + \frac{\partial Y_{CRFW}}{\partial w} \Big|^\ast]
 \end{aligned}$$

$$\begin{aligned}
& + \Delta p [u_o y_p + w_o (y_{wp} + m) + p_o (2my_G + 2 \frac{|p_o|}{p_o} y_p |p|) + q_o (y_{pq} - mx_g)] + \\
& + \Delta q [y_{vq} v_o + p_o (y_{pq} - mx_g) + r_o (y_{qr} - mz_g) + \left. \frac{\partial Y_{CRFW}}{\partial q} \right|^*] + \\
& + \Delta r [u_o \{ (y_r - m) + 2y_r |r| \delta r \frac{r_o}{|r_o|} \delta r + y_{rn} (\eta_o^{-1}) \} + v_o \{ y_v |r| \frac{r_o}{|v_o|} \} \\
& \cdot \frac{1}{r_o} \sqrt{v_o^2 + w_o^2} \} + y_{wr} w_o + q_o (y_{qr} - mz_g) + r_o \cdot 2my_G + \left. \frac{\partial Y_{CRFW}}{\partial r} \right|^*] \\
& + \Delta \phi [(WTOT - B) \cos \theta_o \cos \phi_o] \\
& + \Delta \theta [-(WTOT - B) \sin \theta_o \sin \phi_o] \\
& + \Delta \delta r [y_r |r| \delta r u_0 |r_o| + \{ y_{\delta r} + (\eta_o^{-1}) y_{\delta rn} \} u_o^2] \\
& + \Delta \eta [y_{rn} u_o r_o + y_{vn} u_o v_o + y_r |v| v_o \sqrt{v_o^2 + w_o^2} + y_{\delta rn} u_o^2 \delta r_o]
\end{aligned}$$

where:

$$\left. \frac{\partial Y_{CRFW}}{\partial v} \right|^* = \frac{\rho}{2} (-\ell^2 \int_{\ell} \frac{Z_{ww}}{D(x) dx}) \int_{\ell} H(x) \frac{(w_o^2(x) + 2v_o^2(x))}{\sqrt{v_o^2(x) + w_o^2(x)}} dx$$

$$\left. \frac{\partial Y_{CRFW}}{\partial w} \right|^* = \frac{\rho}{2} (-\ell^2 \int_{\ell} \frac{Z_{ww}}{D(x) dx}) \int_{\ell} H(x) \frac{v_o(x) w_o(x)}{\sqrt{v_o^2(x) + w_o^2(x)}} dx$$

$$\left. \frac{\partial Y_{CRFW}}{\partial q} \right|^* = \frac{\rho}{2} (\ell^2 \int_{\ell} \frac{Z_{ww}}{D(x) dx}) \int_{\ell} x \frac{H(x) v_o(x) w_o(x)}{\sqrt{v_o^2(x) + w_o^2(x)}} dx$$

$$\left. \frac{\partial Y_{CRFW}}{\partial r} \right|^* = \frac{\rho}{2} (-\ell^2 \int_{\ell} \frac{Z_{ww}}{D(x) dx}) \int_{\ell} x H(x) \frac{(2v_o^2(x) + w_o^2(x))}{\sqrt{v_o^2(x) + w_o^2(x)}}$$

III. Normal Force (Heave)

$$\begin{aligned}
 & (m - z_w^*) \Delta \dot{w} + my_G \Delta \dot{p} - (z_q^* + mx_G) \Delta \dot{q} \\
 = & \Delta u [ 2u_0 \{ z_{\delta s} \delta s + z_{\delta b} \delta b + z_* + (\eta_0 - 1) z_{\delta s \eta} \delta s \} + \\
 & + v_0 \{ (z_{vv} v_0 + z_{vp2} p_0 + z_{vr} r_0) \left( \frac{1}{\sqrt{u_0^2 + v_0^2 + w_0^2}} - \frac{u_0^2}{(u_0^2 + v_0^2 + w_0^2)^{3/2}} \right) \} + \\
 & + w_0 \{ z_w + z_{|w|} \frac{|w_0|}{w_0} + (\eta_0 - 1) z_{w \eta} \} + \\
 & + p_0 \{ (z_{pp} p_0 + z_{rp} r_0) \left( \frac{1}{\sqrt{u_0^2 + v_0^2 + w_0^2}} - \frac{u_0^2}{(u_0^2 + v_0^2 + w_0^2)^{3/2}} \right) \} + \\
 & + q_0 \{ z_q + m + z_{|q|} \frac{|q_0|}{q_0} \delta s + (\eta_0 - 1) z_{q \eta} \} + \\
 & + r_0 \{ z_{rr} r_0 \left( \frac{1}{\sqrt{u_0^2 + v_0^2 + w_0^2}} - \frac{u_0^2}{(u_0^2 + v_0^2 + w_0^2)^{3/2}} \right) \}] + \\
 & + \Delta v [ u_0 \{ \frac{(z_{vr} r_0 + z_{vp2} p_0 + 2z_{vv} v_0)}{\sqrt{u_0^2 + v_0^2 + w_0^2}} \\
 & - \frac{v_0 (z_{rr} r_0^2 + z_{pp} p_0^2 + z_{vp} r_0 p_0 + z_{vr} v_0 r_0 + z_{vp2} v_0 p_0 + z_{vv} v_0^2)}{(u_0^2 + v_0^2 + w_0^2)^{3/2}} \} ] +
 \end{aligned}$$

III. Normal Force (Cont.)

$$\begin{aligned}
 & + v_0 \{ z_w |q| \frac{w_0}{|w_0|} \frac{|q_0|}{\sqrt{v_0^2 + w_0^2}} + \frac{1}{\sqrt{v_0^2 + w_0^2}} \cdot \\
 & (z_{ww} |w_0| + z_w |w| w_0 + (\eta_0 - 1) z_w |w| n w_0) \} + p_0 (z_{vp} - \frac{\partial z_{CRFW}}{\partial r}) \Big|^{*} ] + \\
 & + \Delta w [ u_0 \{ z_w + z |w| \frac{w_0}{|w_0|} + (\eta_0 - 1) z_{wn} \\
 & - \frac{w_0}{(u_0^2 + v_0^2 + w_0^2)^{3/2}} \cdot \\
 & (z_{pp} p_0^2 + z_{rr} r_0^2 + z_{rp} r_0 p_0 + z_{vr} v_0 r_0 + z_{vp2} v_0 p_0 + z_{vv} r_0^2) \} + \\
 & + v_0 \{ z_w |w| \sqrt{1 + (w_0^2/v_0^2)} + z_{ww} \frac{w_0 v_0}{|w_0| \sqrt{v_0^2 + w_0^2}} + (\eta_0 - 1) \frac{z_w |w| n v_0}{\sqrt{v_0^2 + w_0^2}} \} + \\
 & + w_0 \{ z_w |q| \frac{|w_0| |q_0| |w_0|}{\sqrt{v_0^2 + w_0^2}} + \frac{w_0}{\sqrt{v_0^2 + w_0^2}} \cdot \\
 & (2z_w |w| w_0 + \frac{z_{ww}}{|w_0|} \cdot 2w_0 (\eta_0 - 1) z_w |w| n + 2w_0) + \frac{\partial z_{CRFW}}{\partial w} ] + \\
 & + \Delta p [ u_0 \frac{1}{\sqrt{u_0^2 + v_0^2 + w_0^2}} (2z_{pp} p_0 + z_{rp} r_0 + z_{vp2} v_0) + \\
 & + v_0 (z_{vp} - m) + p_0 2m z_G - q_0 m y_G - r_0 m x_G ] +
 \end{aligned}$$

III. Normal Force (Cont.)

$$\begin{aligned}
 & + \Delta q [ u_0 \{ z_q + m + z |q| \delta s \frac{q_0}{|q_0|} \delta s + (n_0 - 1) z_{qn} \} + \\
 & + w_0 \{ z_w |q| \frac{\sqrt{v_0^2 + w_0^2}}{|w_0|} \frac{q_0}{|q_0|} \} + q_0^{2mz_G} - r_0^{my_G} + \frac{\partial z_{CRFW}}{\partial q} \Big|^* ] + \\
 & + \Delta r [ u_0 \{ \frac{1}{\sqrt{u_0^2 + v_0^2 + w_0^2}} (2z_{rr} r_0 + z_{rp} p_0 + z_{vr} v_0) \} \\
 & - p_0^{mx_G} - q_0^{my_G} + \frac{\partial z_{CRFW}}{\partial r} \Big|^* ] + \\
 & + \Delta \phi [ -(WTOT - B) \cos \theta_0 \sin \phi_0 ] \\
 & + \Delta \theta [ -(WTOT - B) \sin \theta_0 \cos \phi_0 ] \\
 & + \Delta \delta s [ (z_{\delta s} + (n_0 - 1) z_{\delta sn}) u_0^2 + z |q| \delta s u_0 |q_0| ] + \\
 & + \Delta \delta b [ z_{\delta b} u_0^2 ] + \\
 & + \Delta n [ z_{qn} u_0 q_0 + z_{wn} u_0 w_0 + z_w |w| n w_0 \sqrt{v_0^2 + w_0^2} + z_{\delta sn} u_0^2 \delta s_0 ]
 \end{aligned}$$

where:

$$\frac{\partial z_{CRFW}}{\partial v} \Big|^* = \frac{\rho}{2} (-l^2 \frac{z_{ww}}{\int_l D(x) dx}) \int_l D(x) \frac{w_0(x) v_0(x)}{\sqrt{v_0^2(x) + w_0^2(x)}} dx$$

$$\frac{\partial z_{CRFW}}{\partial w} \Big|^* = \frac{\rho}{2} (-l^2 \frac{z_{ww}}{\int_l D(x) dx}) \int_l D(x) \frac{(v_0^2(x) + 2w_0^2(x))}{\sqrt{v_0^2(x) + w_0^2(x)}} dx$$

$$\frac{\partial Z_{CRFW}}{\partial q} \Big|_* = \frac{\rho}{2} (\ell^2 \frac{z_{ww}}{\int_\ell D(x) dx}) \int_\ell x \cdot D(x) \frac{(v_0^2(x) + 2w_0^2(x))}{\sqrt{v_0^2(x) + w_0^2(x)}} dx$$

$$\frac{\partial Z_{CRFW}}{\partial r} \Big|_* = \frac{\rho}{2} (-\ell^2 \frac{z_{ww}}{\int_\ell D(x) dx}) \int_\ell x \frac{D(x) w_0(x) v_0(x)}{\sqrt{v_0^2(x) + w_0^2(x)}} dx$$

#### IV. Rolling Torque

$$\begin{aligned}
& -[mz_G + K_v] \Delta \dot{v} + my_G \Delta \dot{w} + [I_x - K_p] \Delta \dot{p} - I_{xy} \Delta \dot{q} - [I_{xz} + K_r] \Delta \dot{r} = \\
& \Delta u [2u_0 \{K_v + K_{\delta r} \delta r_0 + (\eta_0 - 1) K_{\alpha \eta} + \\
& + \beta_{t0}^2 (K_{4t} \sin 4\phi_{t0} + K_{8t} \sin 8\phi_{t0})\} + \\
& + v_0 \{K_v - 2\beta_{t0} \sqrt{\frac{v_{t0}^2}{v_0^2} + \frac{w_{t0}^2}{v_0^2}} \cdot (K_{4t} \sin 4\phi_{t0} + K_{8t} \sin 8\phi_{t0})\} + \\
& + p_0 K_p + q_0 my_G + r_0 mz_G + M_o Z_G + K_r] r_0 \\
& + \Delta v [u_0 \left\{ \frac{2v_0 \beta_{t0}}{\sqrt{v_{t0}^2 + w_{t0}^2}} \cdot (K_{4t} \sin 4\phi_{t0} + K_{8t} \sin 8\phi_{t0}) + \frac{u_0 \beta_{t0} w_{t0}}{\sqrt{v_{t0}^2 + w_{t0}^2}} \right. \\
& \left. (4K_{4t} \sin 4\phi_{t0} + 8K_{8t} \sin 8\phi_{t0}) + K_v \right\} + v_0 \{K_v \left| v \right| \left( \sqrt{1 + \frac{w_0^2}{v_0^2}} + \frac{v_0}{\sqrt{v_0^2 + w_0^2}} \right)\} + \\
& + \beta_{t0}^2 \{ (K_{4t} \sin 4\phi_{t0} + K_{8t} \sin 8\phi_{t0}) 2v_{t0} + \\
& + w_{t0} (4K_{4t} \cos 4\phi_{t0} + K_{8t} 8 \cos 8\phi_{t0}) \} + \\
& + w_0 K_{uw} - p_0 my_G + K_{vq} q_0] +
\end{aligned}$$

IV. Rolling Torque (Cont.)

$$\begin{aligned}
 & + \Delta w [ u_0 \left\{ \frac{2w_{t0} \beta_{t0}}{\sqrt{v_{t0}^2 + w_{t0}^2}} (K_{4t} \sin 4\phi_{t0} + K_{8t} \sin 8\phi_{t0}) \right. \\
 & \quad \left. - \frac{u_0 \beta_{t0} v_{t0}}{\sqrt{v_{t0}^2 + w_{t0}^2}} (4K_{4t} \cos 4\phi_{t0} + 8K_{8t} \cos 8\phi_{t0}) \right\} \\
 & + v_0 \left\{ K_{vw} + \frac{K_v |v| w_0}{\sqrt{v_0^2 + w_0^2}} \right\} + \\
 & + \beta_{t0}^2 \left\{ 2w_{t0} (K_{4t} \sin 4\phi_{t0} + K_{8t} \sin 8\phi_{t0}) \right. \\
 & \quad \left. - v_{t0} (4K_{4t} \cos 4\phi_{t0} + 8K_{8t} \cos 8\phi_{t0}) \right\} + \\
 & + p_0 (K_{wp} - mz_G) + r_0 K_{wr} ] + \\
 \\ 
 & + \Delta p [ u_0 k_p - v_0 my_G + w_0 \{ k_{wp} - mz_G \} + 2k_p |p| |p_0| ] + \\
 & + q_0 (I_{yz} + K_{pq}) - r_0 I_{xy} ] + \\
 \\ 
 & + \Delta q [ u_0 \{ my_G - \left( \frac{2w_0 \beta_{t0} x_{t0} w_{t0}}{\sqrt{v_{t0}^2 + w_{t0}^2}} + 2w_{t0} \beta_{t0}^2 \right) \cdot \right. \\
 & \quad \left. (K_{4t} \sin 4\phi_{t0} + K_{8t} \sin 8\phi_{t0}) \right. \\
 & \quad \left. + \frac{4u_0 v_{t0} x_{t0}}{\sqrt{v_{t0}^2 + w_{t0}^2}} (K_{4t} \cos 4\phi_{t0} + K_{8t} \cos 8\phi_{t0}) \right\} + \\
 & + v_0 \{ K_{vq} \} + p_0 \{ I_{yz} + K_{pq} \} - q_0 2I_{yz} + r_0 \{ (I_y - I_z) \} + \\
 & + K_{qr} + 4\beta_{t0}^2 v_{t0} x_{t0} (K_{4t} \cos 4\phi_{t0} + K_{8t} \cos 8\phi_{t0}) ] +
 \end{aligned}$$

IV. Rolling Torque (Cont.)

$$\begin{aligned}
 & + \Delta r [u_0 \{mz_G + K_r + \frac{2\beta_{t0} v_{t0} x_{t0}}{\sqrt{v_{t0}^2 + w_{t0}^2}} (k_{4t} \sin 4\phi_{t0} + k_{8t} \sin 8\phi_{t0}) + \\
 & + \frac{u_0 \beta_{t0} w_{t0} x_{t0}}{\sqrt{v_{t0}^2 + w_{t0}^2}} (4k_{4t} \phi_{t0} + 8k_{8t} \cos 8\phi_{t0})\} + w_0 K_{wr} - p_0 I_{xy} + \\
 & + q_0 \{(I_y - I_z) + K_{qr}\} - r_0 2I_{yz} + \\
 & + 2v_{t0} x_{t0} \beta_{t0}^2 (k_{8t} \sin 4\phi_{t0} + k_{8t} \sin 8\phi_{t0}) \\
 & + \beta_{t0}^2 w_{t0} x_{t0} (4k_{4t} \cos 4\phi_{t0} + 8k_{8t} \cos 8\phi_{t0})] \\
 & + \Delta \phi [-(y_G^{WTOT} - y_B^B) \cos \theta_0 \sin \phi_0 - (z_G^{WTOT} - z_B^B) \cos \phi_0 \cos \theta_0] + \\
 & + \Delta \theta [(z_G^{WTOT} - z_B^B) \sin \theta_0 \sin \phi_0 - (y_G^{WTOT} - y_B^B) \sin \theta_0 \cos \phi_0] + \\
 & + \Delta \delta r [K_{\delta r} u_0^2] \\
 & + \Delta n [K_{\star n} u_0^2]
 \end{aligned}$$

V. Pitching Torque

$$\begin{aligned}
 mz_G \Delta \dot{u} - (mx_G + M_w) \Delta \dot{w} - I_{xy} \Delta \dot{p} + [I_y - M_q] \Delta \dot{q} - I_{yz} \Delta \dot{r} \\
 = \Delta u [2u \{M^* + M_{\delta s} \delta s_0 + M_{\delta b} \delta b_0 + (\eta_0 - 1) M_{\delta s \eta} \delta s\} + \\
 + v_0 \{M_{vr} r_0 + M_{vp} p_0\} + M_{vv} v_0 \} \left( \frac{v_0^2 + w_0^2}{u_0^2 + v_0^2 + w_0^2} \right)^{3/2} \\
 + w_0 \{M_w + M \left| \frac{w_0}{w} \right| + (\eta_0 - 1) M_{wn} \} + \\
 + p_0 \{M_{pp} p_0 + M_{rp2} r_0\} \left( \frac{v_0^2 + w_0^2}{u_0^2 + v_0^2 + w_0^2} \right)^{3/2} \\
 + q_0 \{M_q - mx_G + M \left| q \right| \delta s \left| \frac{q_0}{q} \right| \delta s_0 + (\eta_0 - 1) M_{qn} \} + \\
 + \frac{r_0 M_{rr} r_0 (v_0^2 + w_0^2)}{(u_0^2 + v_0^2 + w_0^2)^{3/2}} + \\
 + \Delta v \left[ \frac{u_0}{(u_0^2 + v_0^2 + w_0^2)^{3/2}} \{M_{vv} (2v_0(u_0^2 + w_0^2) + v_0^3) \right. \\
 \left. - v_0(M_{rr} r_0^2 + M_{pp} p_0^2 + M_{vr} r_0 v_0 + M_{vp} v_0 p_0 + M_{rp2} r_0 p_0)\} + \right. \\
 + \frac{u_0}{\sqrt{u_0^2 + v_0^2 + w_0^2}} (M_{rr} r_0 + M_{vp} p_0 + M_{vr} r_0) + \\
 + \frac{v_0}{\sqrt{v_0^2 + w_0^2}} \{M \left| w \right| q_0 + M_w \left| w \right| w_0 + M_{ww} \left| w \right| w_0\} + \\
 + (\eta_0 - 1) M_{wwn} w_0 \} + p_0 mx_G + r_0 mz_G + \frac{\partial M_{CRFW}}{\partial v} \Big|^{*} ] +
 \end{aligned}$$

V. Pitching Torque (Cont.)

$$\begin{aligned}
 & + \Delta w [ u_0 \left\{ \frac{-w_0}{(u_0^2 + v_0^2 + w_0^2)^{3/2}} \cdot \right. \\
 & \quad \left. (M_{pp} p_0^2 + M_{rr} r_0^2 + M_{vr} v_0 r_0 + M_{vp} v_0 p_0 + M_{rp2} v_0 p_0 + M_{vv} v_0^2) \right. \\
 & \quad \left. + M_w + M|w| \frac{w_0}{|w_0|} + (\eta_0 - 1) M_{wn} \right\} + \frac{w_0}{\sqrt{v_0^2 + w_0^2}} \cdot \\
 & \quad \left\{ M|w|q q_0 + M_w|w| \frac{(2w_0^2 + v_0^2)}{w_0} + M_{ww} \frac{(2w_0^2 + v_0^2)}{|w_0|} \right. \\
 & \quad \left. + (\eta_0 - 1) M_w|w|\eta \frac{(2w_0^2 + v_0^2)}{w_0} \right\} - m z_G q_0 + \frac{\partial M_{CRFW}}{\partial w} \Big|^{*} ] + \\
 & + \Delta p \left[ \frac{u_0}{\sqrt{u_0^2 + v_0^2 + w_0^2}} (2M_{pp} p_0 + M_{vp} v_0 + M_{rp2} r_0) + m x_G v_0 \right. \\
 & \quad \left. - 2p_0 I_{zx} - q_0 I_{zy} + (I_z - I_x + M_{rp}) r_0 \right] + \\
 & + \Delta q [ u_0 \{ M_q - m x_G + (\eta_0 - 1) M_{qn} + M|q| \delta s \frac{q_0}{|q_0|} \delta s_0 \} + \\
 & \quad + v_0 M|w|q \sqrt{1 + \frac{w_0^2}{v_0^2}} - m z_G w_0 - I_{yz} p_0 + 2M_q|q| |q_0| + \\
 & \quad + I_{xy} r_0 + \frac{\partial M_{CRFW}}{\partial q} \Big|^{*} ] + \\
 & + \Delta r \left[ \frac{u_0}{\sqrt{u_0^2 + v_0^2 + w_0^2}} (M_{vr} v_0 + M_{rp2} p_0 + 2M_{rr} r_0) + m z_G v_0 + \right. \\
 & \quad \left. + p_0 (I_z - I_x + M_{rp}) + I_{xy} q_0 + 2I_{xz} r_0 + \frac{\partial M_{CRFW}}{\partial r} \Big|^{*} \right]
 \end{aligned}$$

V. Pitching Torque (Cont.)

$$\begin{aligned}
 & + \Delta\phi [-(x_G^{WTOT} - x_B^B) \cos \theta_0 \sin \phi_0] + \\
 & + \Delta\theta [(x_G^W - x_B^B) \sin \theta_0 \cos \phi_0 - (z_G^{WTOT} - z_B^B) \cos \theta_0] + \\
 & + \Delta\delta s [(M_{\delta s} + M_{\delta s n}(\eta_0 - 1))u_0^2 + M_{q|\delta s u_0|q_0}] + \\
 & + \Delta\delta b [M_{\delta b}u_0^2] \\
 & + \Delta\eta [M_{qn}u_0q_0 + M_{wn}u_0w_0 + M_w|w|\eta \sqrt{v_0^2 + w_0^2}] +
 \end{aligned}$$

Where:  $\frac{\partial M_{CRFW}}{\partial v} \Big|_* = \frac{\rho}{2} (\ell^2 \frac{Z_{ww}}{\int_\ell D(x) dx}) \int_\ell x \frac{D(x) w_0(x) v_0(x)}{\sqrt{v_0^2(x) + w_0^2(x)}} dx$

$$\frac{\partial M_{CRFW}}{\partial w} \Big|_* = \frac{\rho}{2} (\ell^2 \frac{Z_{ww}}{\int_\ell D(x) dx}) \int_\ell x D(x) \frac{(v_0^2(x) + 2w_0^2(x))}{\sqrt{v_0^2(x) + w_0^2(x)}} dx$$

$$\frac{\partial M_{CRFW}}{\partial q} \Big|_* = \frac{\rho}{2} (-\ell^2 \frac{Z_{ww}}{\int_\ell D(x) dx}) \int_\ell x^2 D(x) \frac{(v_0^2(x) + 2w_0^2(x))}{\sqrt{v_0^2(x) + w_0^2(x)}} dx$$

$$\frac{\partial M_{CRFW}}{\partial r} \Big|_* = \frac{\rho}{2} (\ell^2 \frac{Z_{ww}}{\int_\ell D(x) dx}) \int_\ell x^2 D(x) \frac{w_0(x) v_0(x)}{\sqrt{v_0^2(x) + w_0^2(x)}} dx$$

VI. Yawing Torque.

$$\begin{aligned}
 & -my_G \Delta \dot{u} + (mx_G - N_v) \Delta \dot{v} - (I_{zx} + N_p) \Delta \dot{p} - I_{yz} \Delta \dot{q} + (I_z - N_r) \Delta \dot{r} \\
 & = \Delta u [2u_0 \{N^* + (N_{\delta r} + (\eta_0 - 1)N_{\delta_{x\eta}})\delta r_0\} + \\
 & + v_0 \{N_v + N_{vw} \frac{w_0(v_0^2 + w_0^2)}{(u_0^2 + v_0^2 + w_0^2)^{3/2}} + (\eta_0 - 1)N_{vn}\}] + \\
 & + N_p p_0 + r_0 [N_r - mx_G + N \left| r \right| \delta r \frac{|r_0|}{r_0} \delta r_0 + (\eta_0 - 1)N_{rn}] + \\
 & + \Delta v [u_0 \{N_v + N_{vw} \frac{w_0(w_0^2 + u_0^2)}{(u_0^2 + v_0^2 + w_0^2)^{3/2}} + (\eta_0 - 1)N_{vn}\} \\
 & + \frac{v_0}{\sqrt{v_0^2 + w_0^2}} \{N \left| v \right| r r_0 + 2N_v \left| v \right| v_0 + 2(\eta_0 - 1)N_v \left| v \right| n v_0\}] + \\
 & + \frac{w_0}{\sqrt{v_0^2 + w_0^2}} \{N_v \left| v \right| w_0 + (\eta_0 - 1)N_v \left| v \right| n w_0\} + \\
 & + N_{vq} q_0 - my_G r_0 + \frac{\partial N_{CRFW}}{\partial v} \Big| ^* ] + \\
 & + \Delta w [u_0 N_{vw} \frac{v_0(u_0^2 + v_0^2)}{(u_0^2 + v_0^2 + w_0^2)^{3/2}} + \frac{v_0}{\sqrt{v_0^2 + w_0^2}} \\
 & \quad \{N_v \left| v \right| w_0 + (\eta_0 - 1)N_v \left| v \right| n w_0\}] + \\
 & + r_0 (N_{wr} + \frac{N \left| v \right| r w_0}{\sqrt{v_0^2 + w_0^2}} + mx_G p_0 + N_{wp} p_0 + my_G q_0 + \frac{\partial N_{CRFW}}{\partial w} \Big| ^* ] +
 \end{aligned}$$

VI. Yawing Torque (Cont.)

$$\begin{aligned}
 & + \Delta p [N_p u_0 + w_0 (m x_G + N_{wp}) + 2 p_0 I_{xy} + q_0 \\
 & \quad (N_{pq} + I_x - I_y + m y_G + N_{pq}) + I_{yz} r_0] + \\
 & + \Delta q [N_{vq} v_0 + m y_G w_0 + (N_{pq} + I_x - I_y) p_0 \\
 & \quad - 2 I_{xy} q_0 + r_0 (N_{qr} - I_{zx}) + \frac{\partial N_{CRFW}}{\partial q} \Big|^*] + \\
 & + \Delta r [u_0 \{N_r - m x_G + N_r |r| \delta r \frac{r_0}{|r_0|} \delta r_0 + (n_0 - 1) N_{r\eta}\} + \\
 & \quad + v_0 (N_r |v|_r - 1 + \frac{w_0^2}{v_0^2} - m y_G) + N_{wr} w_0 + I_{yz} p_0 + \\
 & \quad + q_0 (N_{qr} - I_{zx}) + 2 N_r |r| |r_0| + \frac{\partial N_{CRFW}}{\partial r} \Big|^{*}] \\
 & + \Delta \phi [(x_G^{WTOT} - x_B^B) \cos \theta_0 \cos \phi_0] + \\
 & + \Delta \theta [y_G^{WTOT} - y_B^B) \cos \theta_0 - (x_G^W - x_B^B) \sin \theta_0 \sin \phi_0] + \\
 & + \Delta \delta r [(N_{\delta r} + N_{\delta r \eta} (n_0 - 1)) u_0^2 + N_r |r| \delta r u_0 |r_0|] + \\
 & + \Delta \eta [N_{x\eta} u_0 r_0 + N_{v\eta} u_0 v_0 + N_v |v|_v \sqrt{v_0^2 + w_0^2} + N_{\delta r \eta} u_0^2 \delta r_0]
 \end{aligned}$$

where:

$$\frac{\partial N_{CRFW}}{\partial v} \Big|^{*} = \frac{\rho}{2} (-l^2 \int_l^\infty \frac{Z_{ww}}{D(x) dx} \int_l^\infty x H(x) \frac{(w_0^2(x) + 2v^2(x))}{\sqrt{v_0^2(x) + w_0^2(x)}} dx)$$

$$\frac{\partial N_{CRFW}}{\partial w} \Big|^{*} = \frac{\rho}{2} (-l^2 \int_l^\infty \frac{Z_{ww}}{D(x) dx} \int_l^\infty x H(x) \frac{v_0(x) w_0(x)}{\sqrt{v_0^2(x) + w_0^2(x)}} dx)$$

$$\frac{\partial N_{CRFW}}{\partial q} \Big|^{*} = \frac{\rho}{2} \left( l^2 \frac{z_{ww}}{\int_l D(x) dx} \right) \int_l x^2 H(x) \frac{v_0(x) w_0(x)}{\sqrt{v_0^2(x) + w_0^2(x)}} dx$$

$$\frac{\partial N_{CRFW}}{\partial r} \Big|^{*} = \frac{\rho}{2} \left( -l^2 \frac{z_{ww}}{\int_l D(x) dx} \right) \int_l x^2 H(x) \frac{(w_0^2(x) + 2v^2(x))}{\sqrt{v_0^2(x) + w_0^2(x)}} dx$$

## APPENDIX C

The SUBMODEL program as detailed in reference [18] was developed at Draper Laboratory to perform any of the following tasks:

1. Solve the previously developed nonlinear differential equations of motion of a submarine.
2. Search for a local equilibrium point in the nonlinear equations of motion by finding a set of state variable values for which the derivatives are essentially zero.
3. Calculate the linearized dynamics about a particular nominal point using the previously developed linearized equations.
4. Solve the linearized equations of motion for the submarine.
5. Simulate, using either the linear or nonlinear equations, the compensated vehicle response.

The program, as originally implemented was designed to handle nonlinear equations of the form

$$\underline{M} \dot{\underline{x}} = \underline{f}(\underline{x}, \underline{u})$$

where

$\underline{x}$  = 10x1 state vector

$\underline{u}$  = 4x1 control vector

$\underline{f}$  = 10x1 vector that is the nonlinear functions of the states and controls

$\underline{M}$  = 10x10 matrix of hydrodynamic coefficient

The first nine states are  $u$  (forward velocity),  $v$ ,  $w$ ,  $p$ ,  $q$ ,  $r$ ,  $\phi$  ( $\emptyset$ ),  $\theta$ , and  $\psi$  ( $\psi$ ). The tenth differential equation and state variable is used to describe the propulsion dynamics. The four controls originally incorporated in SUBMODEL were  $\delta_s$  (sternplane deflection),  $\delta_b$  (bowplane deflection),  $\delta_r$  (rudder deflection), and  $W_{STEAM}$  (steam flow).

For purposes of this thesis, the SUBMODEL Program was modified for the following reasons. The present operating procedures are such that the propulsion plant is controlled from within the engine room of the submarine. The engineers maintain the ordered propeller speed regardless of the maneuver the submarine is presently undertaking. Additionally, as discussed previously, the fairwater planes are placed in a fixed position and not utilized under normal operating conditions. (It should be noted that by not utilizing the fairwater planes under normal conditions, a separate set of gains can, alternatively, be generated as a method of backup control of vehicle depth.) Further, it is the intent of this thesis to use and evaluate the loop transfer recovery technique (discussed in Chapter 4) to design the compensator. This methodology requires a square system with equal control inputs (u), and observed outputs, y. Finally, the controller to be designed is one that will control the heading and depth of the submarine.

Due to these requirements and considerations a modification to the SUBMODEL program was developed. CONSTRPS is a computer program which will accomplish the same five tasks as outlined previously, but the shaft speed is assumed constant and the number of controls and outputs can be varied. The above considerations led to the adoption of a two by two system with the two controls being the rudder and the sternplanes and the outputs, psi and z. The propulsion variable, with constant shaft speed becomes a function of the forward velocity and therefore, is incorporated in the u state variable. To summarize:

$$\underline{x} = \begin{bmatrix} u \\ v \\ w \\ p \\ q \\ \text{phi} \\ \text{theta} \\ \text{psi} \\ z \end{bmatrix}$$

$$\underline{y} = \begin{bmatrix} \text{psi} \\ z \end{bmatrix}$$

$$\underline{u} = \begin{bmatrix} \delta s \\ \delta r \end{bmatrix}$$

Before the linearized dynamics can be calculated, equations of motion solved, or the local equilibrium point search for, the program must be supplied the mass properties, hydrodynamic coefficients, and the propulsion and drag constants. The constants and coefficients describe the dynamics of a specific vehicle; and, with two exceptions, are assumed to be valid for any dynamic condition. The exceptions are the propulsion variables, wake and thrust deduction which must be included in the propulsion data provided to the program. Within the SUBMODEL and CONSTRPS program there are two different propulsion models. The RPS propulsion model calculates these variables while in the ETA propulsion model these two variables are assumed constant.

The RPS propulsion model contains a first order differential equation in terms of rps (revolutions per second) of the propellor and differential equation in terms of eta (eta being defined as  $u_t/U$ ). It is a simplified version of the RPS model and is the propulsion model that was linearized and included in the linear equations of motion. Thus, a method of determining accurate wake and thrust deduction factors is to solve the nonlinear equations of motion using the RPS model and use the values of wake and thrust deduction calculated after the transients have settled out.

At this point a nominal point can be found by integrating the nonlinear equations of motion (using the ETA propulsion model with the wake and thrust deduction found above) and using a set of search routines. To integrate the nonlinear equations of motion, initial conditions of the states and controls must be supplied. The program solves the nonlinear equations using a fourth order Runge Kutta routine. Additionally, the initial and final times and the integration time step must be specified.

The search routines take a supplied guess (provided by the integration of the nonlinear equations using the ETA propulsion model) and iterate a specified number of times in search of a nominal point. The routines iterate by perturbing the state variables in attempting to

find a combination that sets the derivatives of the states equal to zero. The closeness of a point to being a local equilibrium point is determined by how close the sum of the squares of the derivatives is to zero.

Once the nominal point is found, the linearized dynamics of the form

$$\dot{\underline{x}} = \underline{M}^{-1} \underline{A} \underline{x} + \underline{M}^{-1} \underline{B} \underline{u}$$

(where x and u are the perturbations from the nominal values of the state and the controls) can be calculated by linearizing about the nominal point. The A and B matrices are calculated and placed in a file for use in later designing a compensator. Further, if one desired to ascertain the linear dynamics by solving the linearized differential equations, the initial conditions of the state and controls must be provided as well as the nominal point. The perturbations from the nominal point are then calculated and the linear dynamics generated. As with the nonlinear equations, the user must specify the initial time, final time, and integration time step. Also, the options to store data for plotting and to print out the state and control responses must be delineated.

Table C.1: Twenty Knot Accelerations and Equilibrium States

XDOT( 1) = -.766276E-20  
XDOT( 2) = 0.185523E-11  
XDOT( 3) = 0.949660E-19  
XDOT( 4) = -.225747E-11  
XDOT( 5) = 0.651512E-19  
XDOT( 6) = 0.364509E-14  
XDOT( 7) = 0.770974E-19  
XDOT( 8) = -.134837E-22

U = 0.333301E+02  
V = 0.573749E-14  
W = -.585469E-17  
P = 0.770974E-19  
Q = -.366668E-20  
R = -.343823E-16  
PHI = 0.608781E-02  
THETA = -.160134E-14  
PSI = 0.153802E-02  
Z = 0.202062E-01  
DS = 0.000000E+00  
DB = 0.000000E+00  
DR = 0.000000E+00

**Table C.2: Twenty Knot Linear System: A, B and C Matrices**

A MATRIX

```

-.25220E-01 -.56120E-16 -.12154E-03 -.52704E-16 8.31446E-01 8.11545E-15 8.00000E+00 8.29551E-05 8.00000E+00 8.00000E+00
-.38649E-05 -.89121E-01 8.12332E-16 -.89461E+00 8.26458E-16 -.11477E+02 8.15181E+00 8.39112E-21 8.00000E+00 8.00000E+00
-.64150E-06 -.41217E-19 -.88040E-01 -.58623E-14 8.07214E+01 -.16702E-15 8.00000E+00 8.76178E-02 8.00000E+00 8.00000E+00
8.37670E-05 -.79773E-02 -.51467E-21 -.29444E+00 -.29526E-16 -.10740E-01 -.16213E+00 -.46107E-21 8.00000E+00 8.00000E+00
8.21157E-06 8.49257E-21 8.18332E-02 -.30799E-16 -.26702E+00 -.21257E-19 8.00000E+00 -.25123E-02 8.00000E+00 8.00000E+00
-.40092E-06 -.14481E-02 -.44410E-21 -.48612E-02 -.77474E-19 -.23900E+00 8.26100E-05 8.77704E-24 8.00000E+00 8.00000E+00
8.00000E+00 8.00000E+00 8.00000E+00 8.10000E+01 -.29672E-20 -.27923E-16 8.41353E-39 -.34400E-16 8.00000E+00 8.00000E+00
8.00000E+00 8.00000E+00 8.00000E+00 8.00000E+00 8.10000E+01 -.10626E-05 8.30400E-16 8.00000E+00 8.00000E+00 8.00000E+00
8.00000E+00 8.00000E+00 8.00000E+00 8.10000E+01 -.14800E-22 8.96043E-33 8.00000E+00 8.00000E+00 8.00000E+00
8.27923E-16 8.10626E-05 8.10000E+01 8.00000E+00 8.00000E+00 8.00000E+00 8.57400E-14 -.33335E+02 8.00000E+00 8.00000E+00

```

B MATRIX

```

8.26014E-02 -.75904E-05 8.00000E+00
8.00000E+00 8.00000E+00 8.10751E+01
-.71457E+00 -.67190E+00 8.00000E+00
8.00000E+00 8.00000E+00 8.19824E-01
-.22110E-01 8.64513E-02 8.00000E+00
8.00000E+00 8.00000E+00 -.27184E-01
8.00000E+00 8.00000E+00 8.00000E+00
8.00000E+00 8.00000E+00 8.00000E+00
8.00000E+00 8.00000E+00 8.00000E+00

```

C MATRIX

```

8.00000E+00 8.00000E+00 8.00000E+00 8.00000E+00 8.00000E+00 8.00000E+00 8.00000E+00 8.10000E+01 8.00000E+00 8.00000E+00
8.00000E+00 8.00000E+00 8.00000E+00 8.00000E+00 8.00000E+00 8.00000E+00 8.00000E+00 8.10000E+01 8.00000E+00
8.00000E+00 8.00000E+00 8.00000E+00 8.00000E+00 8.00000E+00 8.00000E+00 8.00000E+00 8.10000E+01 8.00000E+00

```

Table C.3: Twenty Knot Augmented Linear System: A, B, and C Matrices

A PENTEK

© MATTEO

0.000E+00 0.000E+00  
0.100E+00 0.000E+00  
0.000E+00 0.100E+00

C MATRIX

**Table C.4: Twenty Knot Compensator Gains: G and H Matrices**

**G MATRIX**

```
-1.16E-02 0.414E-02 0.453E+02 -.364E-02 -.297E+00 0.301E+00 0.469E-02 -.292E+04 -.324E-02 0.100E+02 0.211E+02 -.308E-02  
-.462E-04 0.222E+00 -.129E-01 -.159E-01 0.798E+00 -.377E+02 0.159E-01 0.522E+00 -.100E+02 -.324E-02 -.308E-02 0.413E+01
```

**H MATRIX**

```
0.114E-17 -.469E-16  
0.470E-14 0.123E-15  
0.846E-18 -.161E-18  
-.337E-15 0.729E-19  
0.246E-20 -.289E-20  
-.163E-16 -.982E-19  
-.121E-15 -.833E-17  
-.231E-19 0.249E-18  
0.100E+00 -.550E-15  
0.583E-14 0.100E+00  
0.200E-21 -.340E-21  
-.234E-18 0.792E-19
```

## APPENDIX D

**Table D.1: Ten Knot Augmented Linear System: A, B and C Matrices**

### A MATRIX

```

-.131E-01 0.904E-12 -.614E-04 0.701E-12 0.159E-01 -.761E-10 0.000E+00 0.294E-05 0.000E+00 0.667E-05 0.000E+00
-.159E-05 -.451E-01 -.257E-14 -.453E+00 -.398E-11 -.261E+01 0.132E+00 0.673E-16 0.000E+00 0.000E+00 0.000E+00 0.173E+00
-.333E-06 -.119E-12 -.294E-01 0.379E-10 0.442E+01 0.333E-11 0.000E+00 0.762E-02 0.000E+00 0.000E+00 -.233E+00 0.000E+00
0.191E-03 -.404E-02 0.403E-15 -.150E+00 0.442E-12 -.961E-02 -.162E+00 -.822E-16 0.000E+00 0.000E+00 0.000E+00 0.307E-02
0.110E-06 -.777E-15 0.524E-03 0.488E-12 -.138E+00 0.124E-12 0.000E+00 -.251E-02 0.000E+00 0.000E+00 -.548E-02 0.000E+00
-.300E-06 -.533E-03 0.971E-15 -.231E-02 0.111E-13 -.121E+00 0.262E-03 0.134E-16 0.000E+00 0.000E+00 0.000E+00 -.670E-02
0.000E+00 0.000E+00 0.000E+00 0.100E+01 -.511E-15 0.144E-11 -.907E-15 0.403E-12 0.000E+00 0.000E+00 0.000E+00 0.000E+00
0.000E+00 0.000E+00 0.000E+00 0.000E+00 0.100E+01 0.300E-03 -.403E-12 0.000E+00 0.000E+00 0.000E+00 0.000E+00
0.000E+00 0.000E+00 0.000E+00 0.000E+00 -.300E-03 0.100E+01 -.594E-15 0.884E-24 0.000E+00 0.000E+00 0.000E+00 0.000E+00
-.144E-11 -.300E-03 0.100E+01 0.000E+00 0.000E+00 0.000E+00 -.373E-10 -.169E+02 0.000E+00 0.000E+00 0.000E+00 0.000E+00
0.000E+00 0.000E+00 0.000E+00 0.000E+00 0.000E+00 0.000E+00 0.000E+00 0.000E+00 0.000E+00 0.000E+00 -.100E+00 0.000E+00
0.000E+00 0.000E+00 0.000E+00 0.000E+00 0.000E+00 0.000E+00 0.000E+00 0.000E+00 0.000E+00 0.000E+00 0.000E+00 -.100E+00

```

### B MATRIX

```

0.000E+00 0.000E+00
0.100E+00 0.000E+00
0.000E+00 0.100E+00

```

### C MATRIX

```

0.000E+00 0.000E+00 0.000E+00 0.000E+00 0.000E+00 0.000E+00 0.000E+00 0.100E+01 0.000E+00 0.000E+00 0.000E+00
0.000E+00 0.000E+00 0.000E+00 0.000E+00 0.000E+00 0.000E+00 0.000E+00 0.000E+00 0.100E+01 0.000E+00 0.000E+00

```

**Table D.2: Ten Knot System Eigenvalues and Transmission Zeros**

**POLES**

<b>NUMBER</b>	<b>REAL</b>	<b>IMAG</b>	<b>DAMPING</b>	<b>FREQUENCY</b>
1	0.000000000E+00			
2	0.000000000E+00			
3	-5.828713416E-03			
4	-1.311178789E-02			
6	-1.329846220E-02	1.812443465E-02	5.915679721E-01	2.248002398E-02
7	-1.000000000E-01			
8	-1.000000000E-01			
9	-1.382963877E-01			
10	-1.646311070E-01			
12	-7.297208977E-02	3.932787325E-01	1.824341654E-01	3.999913591E-01

**ZEROES**

<b>NUMBER</b>	<b>REAL</b>	<b>IMAG</b>	<b>DAMPING</b>	<b>FREQUENCY</b>
1	-1.311178695E-02			
2	-7.523505946E-02			
3	-8.382681741E-02			
4	2.412065619E-01			
6	-7.312544279E-02	-3.920159008E-01	1.833738696E-01	3.987778791E-01

**Table D.3: Ten Knot Compensator Gains: G and H Matrices**

**G MATRIX**

```
-420E-02 -391E-02 0.148E+03 -.115E-01 -.851E+04 -.239E+01 -.311E+04 0.229E-01 0.173E+02 0.152E+02 0.660E-02  
0.194E-04 0.399E+00 0.161E+00 0.560E-01 -.717E+01 -.993E+02 -.260E-01 -.294E+01 -.173E+02 0.229E-01 0.660E-02 0.313E+01
```

**H MATRIX**

```
0.829E-19 -.120E-15  
-.460E-14 -.400E-16  
-.913E-18 0.514E-18  
0.190E-15 -.490E-18  
-.593E-23 0.340E-23  
0.173E-16 0.394E-16  
0.703E-15 -.390E-17  
0.100E-18 -.597E-19  
0.100E+00 -.904E-16  
0.122E-15 0.100E+00  
-.800E-23 0.194E-26  
0.140E-27 -.470E-26
```

## APPENDIX E

**Table E.1: Five Knot Augmented Linear System: A, B and C Matrices**

### A MATRIX

```

-.711E-02 -.193E-13 -.314E-04 -.179E-13 0.832E-02 0.315E-11 0.000E+00 0.296E-03 0.000E+00 0.000E+00 0.181E-03 0.000E+00
-.612E-04 -.234E-01 0.912E-17 -.227E+00 0.877E-14 -.303E+01 0.132E+00 -.188E-19 0.000E+00 0.000E+00 0.000E+00 0.744E-01
-.180E-06 -.112E-16 -.172E-01 -.171E-11 0.231E+01 0.124E-15 0.000E+00 0.762E-02 0.000E+00 0.000E+00 -.634E-01 0.000E+00
0.100E-03 -.211E-02 0.611E-20 -.704E-01 -.100E-13 -.501E-02 -.162E+00 0.194E-19 0.000E+00 0.000E+00 0.000E+00 0.139E-02
0.599E-07 0.267E-19 0.269E-03 -.107E-13 -.707E-01 -.316E-17 0.000E+00 -.251E-02 0.000E+00 0.000E+00 -.154E-02 0.000E+00
-.142E-06 -.438E-03 0.144E-19 -.121E-02 0.729E-17 -.632E-01 0.262E-03 -.313E-22 0.000E+00 0.000E+00 0.000E+00 -.189E-02
0.000E+00 0.000E+00 0.000E+00 0.100E+01 0.120E-18 -.616E-15 -.533E-38 -.117E-13 0.000E+00 0.000E+00 0.000E+00 0.000E+00
0.000E+00 0.000E+00 0.000E+00 0.000E+00 0.100E+01 0.194E-03 0.117E-13 0.000E+00 0.000E+00 0.000E+00 0.000E+00
0.000E+00 0.000E+00 0.000E+00 0.000E+00 -.194E-03 0.100E+01 0.063E-20 0.721E-29 0.000E+00 0.000E+00 0.000E+00 0.000E+00
0.616E-15 -.194E-03 0.100E+01 0.000E+00 0.000E+00 0.000E+00 0.168E-11 -.881E+01 0.000E+00 0.000E+00 0.000E+00 0.000E+00
0.000E+00 0.000E+00 0.000E+00 0.000E+00 0.000E+00 0.000E+00 0.000E+00 0.000E+00 0.000E+00 0.000E+00 -.100E+00 0.000E+00
0.000E+00 0.000E+00 0.000E+00 0.000E+00 0.000E+00 0.000E+00 0.000E+00 0.000E+00 0.000E+00 0.000E+00 0.000E+00 -.100E+00

```

### B MATRIX

```

0.000E+00 0.000E+00
0.100E+00 0.000E+00
0.000E+00 0.100E+00

```

### C MATRIX

```

0.000E+00 0.000E+00 0.000E+00 0.000E+00 0.000E+00 0.000E+00 0.000E+00 0.100E+01 0.000E+00 0.000E+00 0.000E+00
0.000E+00 0.000E+00 0.000E+00 0.000E+00 0.000E+00 0.000E+00 0.000E+00 0.000E+00 0.100E+01 0.000E+00 0.000E+00

```

Table E.2: Five Knot System Eigenvalues and Transmission Zeros

POLES

<u>NUMBER</u>	<u>REAL</u>	<u>IMAG</u>	<u>DAMPING</u>	<u>FREQUENCY</u>
1	0.000000000E+00			
2	0.000000000E+00			
3	-3.024089983E-03			
4	-7.113993141E-03			
5	-3.005117302E-02			
7	-2.892676692E-02	2.308620747E-02	7.815959177E-01	3.700967462E-02
8	-8.558510799E-02			
9	-1.000000000E-01			
10	-1.000000000E-01			
12	-3.825415101E-02	4.001017488E-01	9.517701732E-02	4.019263483E-01

ZEROES

<u>NUMBER</u>	<u>REAL</u>	<u>IMAG</u>	<u>DAMPING</u>	<u>FREQUENCY</u>
1	-7.113992856E-03			
2	-2.890585762E-02			
3	-4.318266216E-02			
4	1.153794658E-01			
6	-3.845341422E-02	-3.996021859E-01	9.578676498E-02	4.014480939E-01

**Table E.3: Five Knot Compensator Gains: G and H Matrices**

**G MATRIX**

```
-.522E-02 -.281E-01 0.166E+03 -.259E-01 -.920E+04 -.167E+01 -.120E-01 -.173E+04 0.822E-02 0.100E+02 0.753E+01 0.209E-02  
-.833E-05 0.480E+00 0.101E+00 0.149E+00 -.501E+01 -.110E+03 0.510E-02 -.104E+01 -.100E+02 0.822E-02 0.209E-02 0.142E+01
```

**H MATRIX**

```
-.490E-17 0.455E-15  
-.104E-14 0.191E-15  
-.291E-18 -.342E-17  
0.445E-17 -.266E-17  
-.881E-20 -.924E-19  
0.378E-17 -.103E-17  
-.994E-19 0.157E-17  
-.287E-16 -.134E-17  
0.100E+00 -.120E-16  
0.255E-14 0.100E+00  
0.000E+00 0.000E+00  
0.000E+00 0.000E+00
```

#### REFERENCES

1. Abkowitz, M.A. Stability and Motion Control of Ocean Vehicles. Cambridge, MA: MIT Press, 1969.
2. Athans, Michael. "The Role and Use of the Stochastic Linear-Quadratic-Gaussian Problem in Control Systems Design," IEEE Transactions on Automatic Control, Vol. AC-16, No. 6 (December 1971): 529-552.
3. Athans, Michael. Multivariable Control Systems. Notes, MIT, Spring 1983.
4. Brogan, William L. Modern Control Theory. New York: Quantum Publishers, Inc., 1974.
5. Doyle, J.C. and Stein, Gunter. "Multivariable Feedback Design: Concepts for a Classical/Modern Synthesis," IEEE Transactions on Automatic Control, Vol. AC-26, No. 1 (February 1981): 4-16.
6. Doyle, J.C. and Stein, Guter. "Robustness with Observers," IEEE Transactions on Automatic Control, Vol. AC-24, No. 4 (August 1979): 756-757.
7. Freudenburg, J.S. and Looze, D.P. "The Impact of Right Half Plane Poles and Zeros and Design Tradeoffs in Feedback Systems," Preprint from IEEE Transactions on Automatic Control, (1984).
8. Gertler, Morton and Hagan, Grant R. "Standard Equations of Motion for Submarine Simulation," Research and Development Report. NSRDC, Washington, D.C. 1976. (AD 653 861)
9. Kuo, B.C. Automatic Control Systems. Englewood Cliffs, N.J.: Prentice Hall, 1982.
10. Kwakernaack, H. and Sivan, R. Linear Optimal Control Systems. New York: Wiley, 1972.
11. Lehtomaki, N.A. "Practical Robustness Measures in Multivariable Control Systems Analysis," Ph.D. Thesis, MIT, 1981.
12. Lehtomaki, N.A.; Sandell, N.R.; and Athans, M. "Robustness Results in Linear-Quadratic-Gaussian Based Multivariable Control Designs," IEEE Transactions on Automatic Control, Vol. AC-26, No. 1 (February 1981): 75-93.
13. Ogata, Katsuhiko. Modern Control Engineering. Englewood Cliffs, N.J.: Prentice Hall, Inc., 1972.

14. Safonov, M.G. "Robustness and Stability Aspects of Stochastic Multivariable Feedback System Design," Ph.D. Thesis, MIT, 1979.
15. Stein, Gunter. "LQG-Based Multivariable Design: Frequency Domain Interpretation," AGARD, NATO, 1981.
16. Takahashi, Y.; Rabins, M.J.; and Auslander, D.M. Control and Dynamic Systems. Reading, MA.: Addison-Wesley Publishing Co., 1972.
17. Triantafyllou, Michael S.; Bodson, Marc; and Athans, Michael. "Real Time Estimation of Ships Motion using Kalman Filtering Techniques," IEEE Journal of Oceanic Engineering, Vol. OE-8, No. 1 (January 1983): 9-20.
18. -----, "Submarine Configuration and Control," Charles Stark Draper Laboratory Memo: Sub 1-1083, 1983.